Multiple sources of slow activity fluctuations in a bacterial chemosensory network

R. Colin[1,*,+], C. Rosazza[1,*], A. Vaknin[2], V. Sourjik[1,+]

[1]Max Planck Institute for Terrestrial Microbiology and LOEWE Center for Synthetic Microbiology (SYNMIKRO), Karl-von-Frisch-Strasse 16, D-35043 Marburg, Germany

[2] The Racah Institute of Physics, the Hebrew University, Jerusalem 91904, Israel

[*] Authors contributed equally to this work.

[+] Corresponding authors: victor.sourjik@synmikro.mpi-marburg.mpg.de,

remy.colin@synmikro.mpi-marburg.mpg.de

Abstract

Cellular networks are intrinsically subject to stochastic fluctuations, but analysis of the resulting noise remained largely limited to gene expression. The pathway controlling chemotaxis of *Escherichia coli* provides one example where posttranslational signaling noise has been deduced from cellular behavior. This noise was proposed to result from stochasticity in chemoreceptor methylation, and it is believed to enhance environment exploration by bacteria. Here we combined single-cell FRET measurements with analysis based on the fluctuation-dissipation theorem (FDT) to characterize origins of activity fluctuations within the chemotaxis pathway. We observed surprisingly large methylation-independent thermal fluctuations of receptor activity, which contribute to noise comparably to the energy-consuming methylation dynamics. Interactions between clustered receptors involved in amplification of chemotactic signals are also necessary to produce the observed large activity fluctuations. Our work thus shows that the high

23 response sensitivity of this cellular pathway also increases its susceptibility to noise, from
24 thermal and out-of-equilibrium processes.

Introduction

It is well established that cellular processes are intrinsically stochastic and therefore prone to fluctuations [1-3]. The best-characterized examples of cellular noise relate to the variability in expression of genes or proteins, observed either across a population of genetically identical cells or within one cell over time [4, 5]. The molecular origins and physiological effects of such expression noise are comparatively well understood [2-4, 6-8]. In contrast, noise that arises in cellular networks at the posttranslational level remains much less characterized. Although such noise is expected to be ubiquitous, e.g., in signaling networks, it was mostly observed indirectly through its effects on gene expression or cell behavior [1, 3].

Chemotaxis of *Escherichia coli,* a bacterial model for signal transduction, previously provided one example where signaling noise has been predicted based on analyses of cell motility and flagellar rotation [9-15]. *E. coli* swims by a succession of straight runs during which the bacterium advances, that are interrupted by short reorientations, or tumbles, which results in a random walk. In chemical gradients, this random walk becomes biased by lengthening the runs towards more favorable conditions. The chemotaxis pathway controlling this behavior is composed of two modules, one mediating signal transduction and another adaptation, that operate on different time scales [16-18] (Figure 1 – Figure Supplement 1A). The signal transduction module includes sensory complexes consisting of the dimers of transmembrane receptors, the kinase CheA and the scaffold protein CheW. Signaling by these complexes can be understood in terms of a two-state model: In the absence of stimulation, receptor dimers are at equilibrium between the active (ON) and inactive (OFF) states, resulting in an intermediate level of autophosphorylation activity of the receptor-associated CheA. Positive chemotactic stimuli

(attractants) shift the equilibrium towards the OFF state, thus inhibiting CheA, whereas repellent stimulation has the opposite effect. Downstream signal transduction occurs via phosphorylation of the response regulator CheY that can subsequently bind to the flagellar motors to induce tumbles. CheY is dephosphorylated with the help of the phosphatase CheZ. All reactions within the signal transduction module occur within a few hundred milliseconds [19], ensuring that swimming bacteria can faithfully monitor their current local environment.

The adaptation module operates on a much longer time scale of seconds to minutes. It includes two enzymes, the methyltransferase CheR and the methylesterase CheB, which add or remove respectively methyl groups at four specific glutamyl residues of the chemoreceptors. Since receptor methylation increases the activity of the chemosensory complexes, these changes gradually compensate for the effects of both attractant and repellent stimulation via a negative feedback loop [20-22]. This enables bacteria to robustly maintain an intermediate steady-state activity of CheA, and thus the level of CheY phosphorylation and frequency of cell tumbles, even in the presence of steady background stimulation. Notably, in both major *E. coli* chemoreceptors Tar and Tsr, two of the four methylated residues are initially encoded as glutamines, *e.g.* Tar is expressed as Tar^{QEQE}. Glutamines are functionally similar to methylated glutamates [23-26], and they are subsequently deamidated to glutamates by CheB [27, 28].

Despite this importance of the adaptation system for robust maintenance of the average signaling output, it was suggested that the relatively small number of methylation enzymes [29] and their slow exchange rates at their receptor substrates [30, 31] lead to fluctuations of the level of phosphorylated CheY [9, 10, 12, 32, 33]. Further amplified by the cooperative response of the flagellar motor [32, 34], these fluctuations were proposed to explain the observed large variation in the motor rotation [9, 10, 15] and in the swimming behavior [9, 11, 13, 35] of individual cells

over time. Subsequent theoretical analyses suggested that such behavioral fluctuations might provide physiological benefit, by enhancing environmental exploration [10, 36-40].

Another distinctive feature of the bacterial chemotaxis pathway is the clustering of chemoreceptors in large signaling arrays, formed through a complex network of interactions between trimers of receptor dimers, CheA and CheW [16]. Although signaling arrays are stable on the time scale of signal transduction [31, 41], they appear to locally reorganize within minutes [42]. Within arrays, the activity states of neighboring receptors are coupled, resulting in amplification and integration of chemotactic signals [24, 25, 43-48]. These allosteric receptor interactions have been previously described using either the Monod-Wyman-Changeux (MWC) model [47] which assumes that receptors operate in units (signaling teams) of 10-20 dimers where activities of individual receptors are tightly coupled [24, 46-49] or using an Ising model of a receptor lattice with intermediate coupling [45, 46]. In both models, the sensitivity of signaling arrays is highest at intermediate levels of receptor activity where receptors can easily switch between ON and OFF states, with optimal intermediate activity being maintained by the adaptation system [43, 44]. Another connection between the adaptation system and receptor clustering is through adaptation assistance neighborhoods, where adaptation enzymes that are transiently tethered to one receptor molecule can methylate (or demethylate) multiple neighboring receptors [30].

In this work we directly quantify signaling noise in *E. coli* chemotaxis, using Förster (fluorescence) resonance energy transfer (FRET) to monitor pathway activity in single cells and with high time resolution. We show that the pathway activity fluctuations arise from interplay of multiple factors, including not only the stochasticity of the methylation system but also cooperative interactions and slow rearrangements of receptors within clusters. Finally, using

analysis based on the fluctuation-dissipation theorem (FDT) we could distinguish between equilibrium and out-of-equilibrium fluctuations within the chemotaxis network and elucidate respective contributions of receptor clusters and methylation to the overall noise.

Results

Fluctuations of chemotaxis pathway activity in single cells

To perform time-resolved measurements of the chemotaxis pathway activity in individual *E. coli* cells, we adapted the microscopy-based ratiometric FRET assay [50] that relies on the phosphorylation-dependent interaction between CheY, fused to yellow fluorescent protein (CheY-YFP), and its phosphatase CheZ, fused to cyan fluorescent protein (CheZ-CFP) (Figure 1 – Figure Supplement 1A). The amount of this complex, and thus the level of FRET, provides a direct intracellular readout of CheA activity [26, 50-52]. In previous studies where this assay was applied to investigate chemotactic signaling in *E. coli* populations [18, 24, 26, 42, 44, 50-60], bacteria expressing the FRET pair were immobilized in a flow chamber and fluorescent signals were collected using photon counters from an area containing several hundred cells [50]. Here, we used a similar setup but instead imaged fluorescence of the FRET pair with an electron multiplication charge-coupled device (EM-CCD) camera (see Materials and methods and Figure 1 – Figure Supplement 1B, C).

As done previously [24, 26, 52, 55], we analyzed *E. coli* cells that express the CheY-YFP/CheZ-CFP FRET pair instead of the native CheY and CheZ and have Tar as the only chemoreceptor (see Materials and methods). The level of Tar expression in these cells and under our conditions

is ~10^4 dimers per cell [24, 26], comparable to the total level of endogenous chemoreceptors [29]. When integrated over the population, the chemotactic response of these cells measured using EM-CCD (Figure 1A and Figure 1 – Figure Supplement 2, upper panel) was very similar to the one observed previously using area detectors [51, 55]. When bacteria in the flow chamber were stimulated with the Tar-specific chemoattractant α-methyl-DL-aspartate (MeAsp), the ratio of the YFP to CFP fluorescence (FRET ratio, $R(t) = YFP(t)/CFP(t)$) first rapidly decreased. This is consistent with the fast attractant-mediated inhibition of the kinase activity, which results in decreased formation of the FRET complex, and therefore reduced energy transfer from the donor (CFP) to the acceptor (YFP) fluorophore. As 10 μM MeAsp is known to fully inhibit the kinase activity in this strain [24, 26], the value of the FRET ratio immediately after stimulation reflects the zero activity baseline. Subsequently, the pathway adapted to the new background level of attractant via the CheR-dependent increase in receptor methylation. But as previously reported adaptation of Tar-only cells to high levels of MeAsp was only partial [53-55], meaning that the adapted pathway activity remained lower than in buffer. Subsequent removal of attractant resulted in a transient increase in kinase activity, followed by the CheB-mediated adaptation through the demethylation of receptors.

Although the FRET ratio measured for individual cells during the same experiment was expectedly noisier than the population-averaged data, both the initial response and subsequent adaptation were clearly distinguishable (Figure 1A and Figure 1 – Figure Supplement 2, lower panel). In contrast to the population measurement, however, a majority of individual cells also exhibited large fluctuations in the FRET ratio on the time scale of 10-100 sec. For cells adapted in buffer, the amplitude of these fluctuations could be as large as the response to strong attractant stimulus. Confirming that this low-frequency noise reflects fluctuations of the pathway activity,

it was not observed when imaging either fluorescent beads or the same FRET pair in receptorless cells that do not activate CheA (Figure 1 – Figure Supplement 3 A, B). Furthermore, inhibition of the pathway activity by saturating stimulation with 10 µM or 25 µM MeAsp also transiently suppressed long-term fluctuations, which subsequently (partly) reappeared upon (partial) recovery of the pathway activity due to adaptation (Figure 1A and Figure 1 – Figure Supplement 2). In contrast, the higher-frequency noise in the FRET ratio could be observed in all strains and conditions, including receptorless cells, indicating that it represents the noise of the measurement. High-frequency noise was also observed in the control measurements using fluorescent beads, although its magnitude was lower, consistent with higher brightness of beads compared to the YFP/CFP expressing cells.

To analyze these activity fluctuations in greater detail, we computed the power spectral density (PSD) of the single-cell FRET ratio, $s_R(\omega)$ (see Materials and methods). The PSD extracts the average spectral content of the temporal variations of the single-cell FRET ratio, *i.e.* determines the frequencies at which this ratio fluctuates, with $s_R(\omega)$ representing the magnitude of fluctuations at a given frequency ω. We observed that at high frequency (ω > 0.1 Hz) the PSD kept a constant frequency-independent low value that was similar in all strains (Figure 1B). We thus conclude that the noise in the FRET ratio in this frequency range is dominated by the shot noise of the measurement. At lower frequency, however, the PSD measured for the Tar-expressing cells adapted in buffer increased dramatically (roughly as $1/\omega$), reaching a low frequency plateau at $\omega/2\pi \simeq 0.015$ Hz. A similar result was obtained for cells expressing Tar in the unmodified (Tar^{EEEE}) state, where all glutamates are directly available for methylation by CheR (Figure 1 – Figure Supplement 4A). The increase of the PSD at low frequency was also observed for cells adapted to either 10 or 25 µM MeAsp (Figure 1B and Figure 1 – Figure

Supplement 4A), although the amplitude of this increase was smaller than for the buffer-adapted cells, apparently consistent with their lower pathway activity (Figure 1A and Figure 1 – Figure Supplement 2). The receptorless strain showed nearly constant noise level over the entire frequency range, as expected for white shot noise, although the PSD increased weakly at the lowest frequency. As such increase was not observed for the control using fluorescent beads (Figure 1 – Figure Supplement 3 A), it might be due to the slow drift of the FRET ratio arising as a consequence of the slightly different bleaching rates of CFP and YFP, but possibly also to slow changes in cell physiology. In any case, the contribution of this low-frequency component to the overall PSD of the Tar-expressing cells is only marginal (note the log scale in Figure 1B), and subtracting it did not markedly change our results (Figure 1 – Figure Supplement 5).

The PSD was further used to calculate the average time autocorrelation function of the single-cell FRET ratio, which reflects the characteristic time scale of activity fluctuations (see Materials and methods). For cells adapted in buffer, the autocorrelation time constant was 9.5 ± 0.5 s, as determined by an exponential fit to the autocorrelation function (Figure 1D). This value is similar to the characteristic time of the pathway activity fluctuation previously deduced from behavioral studies [9, 14]. The same characteristic time was observed in MeAsp-adapted cells, although the amplitude of the correlation was considerably smaller in this case (Figure 1D and Figure 1 – Figure Supplement 4B). Interestingly, at longer times the autocorrelation function becomes weakly negative, indicating an overshoot that is likely caused by the negative feedback in the adaptation system [61]. As expected, no autocorrelation was observed for the receptorless cells.

Finally, the variance of activity was evaluated from the PSD using Parseval's formula [62]. After subtracting the variance measured for the receptorless strain, which reflects the contribution of

the shot noise, the specific variance of the FRET ratio for cells adapted in buffer was $\langle \Delta R^2 \rangle^+ = 0.0046 \pm 0.0002$ (where "+" refers to the presence of adaptation enzymes, $CheR^+$ $CheB^+$). As shown previously [50], the FRET ratio R is related to the relative pathway activity $\langle A \rangle$ as $R = \lambda \langle A \rangle + \mu$, where λ is the conversion factor and μ is a constant corresponding to the baseline FRET ratio at zero pathway activity (i.e., upon stimulation with saturating attractant concentration; Figure 1A). The value $\lambda = 0.10 \pm 0.01$ could be estimated as the mean difference between the measured FRET ratio values corresponding to the fully active (i.e., $\langle A \rangle = 1$) and fully inactive (i.e., $\langle A \rangle = 0$) pathway (see Materials and methods). The calculated variance of the pathway activity was $\langle \Delta A^2 \rangle^+ = 0.46 \pm 0.04$, indicating concerted activity fluctuations across much of the signaling array.

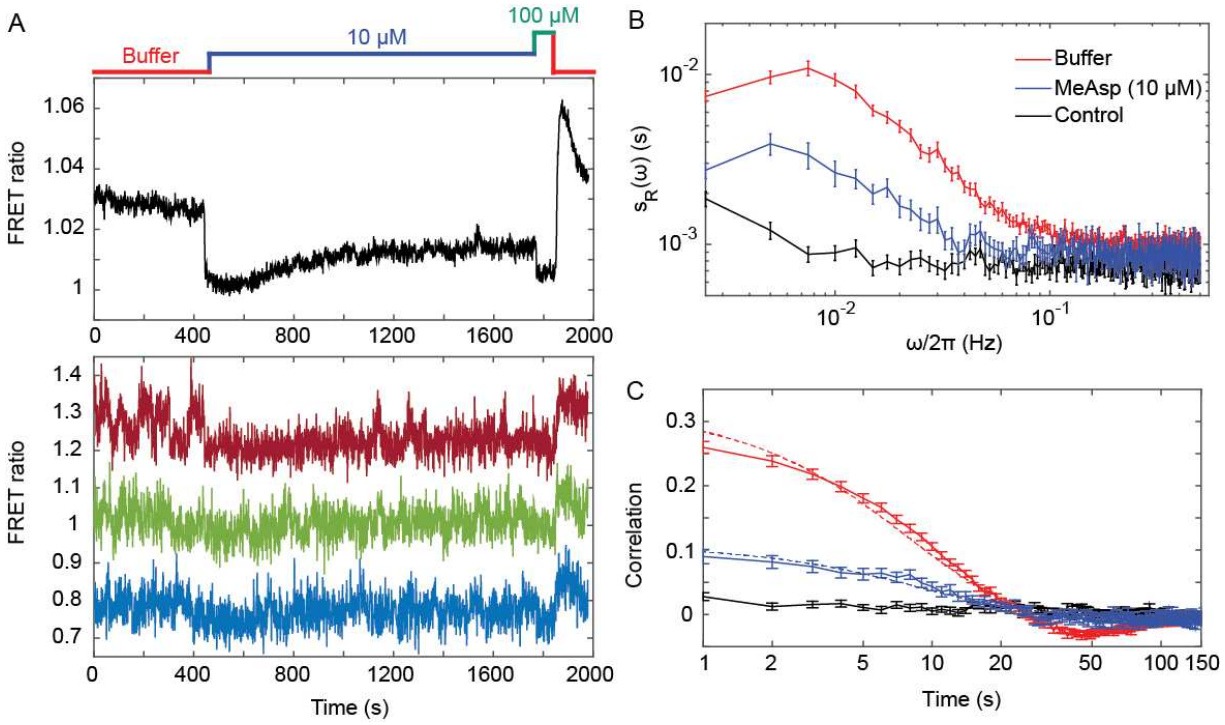

Figure 1. Fluctuations of the chemotaxis pathway activity in individual $CheR^+$ $CheB^+$ cells. (*A*) Time course of the FRET measurements for the $CheR^+$ $CheB^+$ strain expressing the FRET pair CheY-YFP and CheZ-CFP and Tar

as the sole receptor (see Materials and methods for details of expression), for cell population (upper panel) and for representative single cells (lower panel). Cells immobilized in a flow chamber under steady flow (see Materials and methods and Figure 1 – Figure Supplement 1B) were initially adapted in buffer (red) and subsequently stimulated by addition and subsequent removal of indicated concentrations of a non-metabolizable chemoattractant MeAsp (blue and green). The measurement traces for single cells have been shifted along the *y*-axis to facilitate visualization. (*B*) Power spectral density (PSD) of the FRET ratio for single cells adapted in buffer (red curve) or in 10 µM MeAsp (blue curve), as well as for the control receptorless strain in buffer (black curve). (*C*) The corresponding time autocorrelation functions of the single-cell FRET ratio. Dashed lines show fits by exponential decay (see Materials and methods). The error bars represent standard errors of the mean (SEM), and the sample sizes are 265 (buffer), 69 (10 µM) and 103 (receptorless control) single cells coming from at least three independent experiments in each case.

Activity fluctuations in absence of adaptation system

We next monitored the single-cell pathway activity in a strain lacking CheR and CheB, to test whether the observed fluctuations could be solely explained by the action of the adaptation system. Given the observed dependence of the fluctuations on the level of pathway activity, we first analyzed a Δ*cheR*Δ*cheB* strain that was engineered to express Tar receptor in one-modified state (Tar^{QEEE}). This closely mimics the average modification state and intermediate activity of Tar in $CheR^+$ $CheB^+$ cells adapted in buffer [26, 51]. Expectedly, Δ*cheR*Δ*cheB* Tar^{QEEE} cells responded to MeAsp but showed no adaptation comparable to $CheR^+$ $CheB^+$ cells (Figure 2A). But despite the lack of the adaptation system, pathway activity in individual Δ*cheR*Δ*cheB* Tar^{QEEE} cells showed pronounced long-term fluctuations when cells were equilibrated in buffer (Figure 2A, lower panel). These methylation-independent long-term fluctuations were suppressed upon saturating pathway inhibition with 30 µM MeAsp, leaving only the shot noise of the measurement.

In contrast to Tar^{QEEE}, Δ*cheR*Δ*cheB* cells expressing the half-modified Tar^{QEQE} as the sole receptor showed no long-term activity fluctuations in buffer (Figure 2B). Because Tar^{QEQE} is known to be highly active (*i.e.*, strongly biased towards the ON state) in absence of attractants [26, 52] and therefore insensitive to stimulation, we lowered its activity to an intermediate value by stimulating cells with 30 µM MeAsp (Figure 2B, upper panel). This partial stimulation indeed restored low-frequency fluctuations in Δ*cheR*Δ*cheB* Tar^{QEQE} cells (Figure 2B, lower panel). Again, these activity fluctuations were completely abolished upon saturating attractant stimulation. Cumulatively, these results clearly demonstrate that, at intermediate level of activity where the receptors are highly sensitive, pathway output fluctuates even in the absence of the methylation system. These fluctuations were clearly identifiable above shot noise in the PSD of the FRET ratio (Figure 2C), and they were absent under conditions of very low or very high activity. Notably, these methylation-independent fluctuations were slower than those observed in $CheR^{+}$ $CheB^{+}$ cells (Figure 2 – Figure Supplement 2), with a typical time scale of 34 ± 4 s, as determined by fitting the time autocorrelation functions with an exponential decay (Figure 2D), although this time might be slightly under-evaluated since it is already comparable to the total duration of acquisition (400 s). Their amplitude, evaluated again using Parseval's formula, was $\langle \Delta R^2 \rangle^{-} = 0.0025 \pm 0.0001$, corresponding to $\langle \Delta A^2 \rangle^{-} = 0.25 \pm 0.01$, and thus roughly half of the amplitude of fluctuations observed in $CheR^{+}$ $CheB^{+}$ cells.

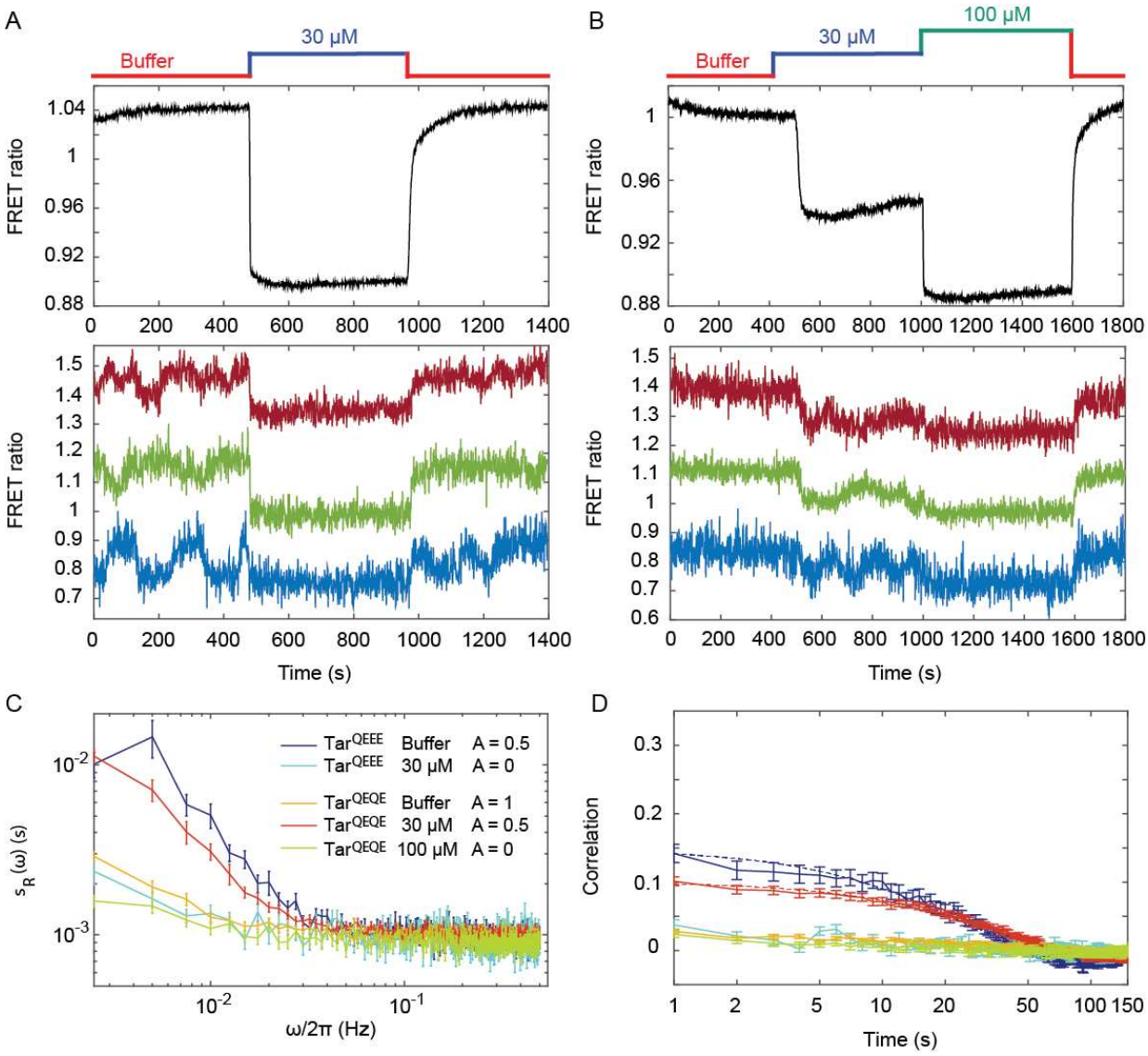

243

244 **Figure 2. Pathway activity fluctuations in Δ*cheR*Δ*cheB* cells.** (*A*) Time course of population-averaged (black;
245 upper panel) and typical single-cell (colors; lower panel) measurements of the FRET ratio for Δ*cheR*Δ*cheB* strain
246 expressing Tar^{QEEE} as the sole receptor. Measurements were performed as in Figure 1. Cells were first equilibrated
247 in buffer (red) and subsequently stimulated by addition (blue) and subsequent removal of 30 µM MeAsp, saturating
248 stimulus for this receptor. (*B*) Same as (A) but for Δ*cheR*Δ*cheB* strain expressing Tar^{QEQE} as the sole receptor and
249 upon stimulation with 30 µM (blue) and then 100 µM (green) MeAsp. Note that for this receptor, 30 µM MeAsp is
250 the sub-saturating stimulus whereas 100 µM MeAsp is the saturating stimulus. The measurement traces for single
251 cells in (A) and (B) have been shifted along the *y*-axis to facilitate visualization. (*C*) PSD of the single-cell FRET
252 ratio for Tar^{QEEE} in buffer (blue) or in 30 µM MeAsp (cyan), Tar^{QEQE} in buffer (orange), in 30 µM MeAsp (red) or in

100 μM MeAsp (yellow). (*D*) Corresponding time autocorrelation functions of the single-cell FRET ratio for indicated strains/conditions. Dashed lines show fits by single exponential decay. Error bars represent standard errors of the mean (SEM), and the sample sizes are 153 (Tar^{QEEE}, buffer), 65 (Tar^{QEEE}, 30 μM), 471 (Tar^{QEQE}, buffer), 404 (Tar^{QEQE}, 30 μM) and 136 (Tar^{QEQE}, 100 μM) single cells coming from at least three independent experiments in each case.

Role of receptor clustering in signaling noise

To investigate whether the observed fluctuations depend on clustering of chemotaxis receptors, we utilized a recently described CheW-X2 version of the adaptor protein CheW that disrupts formation of the receptor arrays without abolishing signaling [56]. This CheW mutant carries two amino acid replacements, R117D and F122S, which are believed to break the receptor arrays into smaller complexes consisting of two trimers of receptor dimers coupled to one CheA [44, 56]. The CheW-X2 is expressed at a level similar to the native CheW [44]. Consistent with reported functionality of such complexes [44, 56, 63], a Δ*cheR*Δ*cheB* strain expressing CheW-X2 and Tar^{QEQE} showed basal activity and response to MeAsp which were similar to the respective strain expressing the native CheW (Figure 3A and Figure 3 – Figure Supplement 1). Nevertheless, this strain showed no apparent long-term fluctuations in the pathway activity above the shot noise, even when its activity was tuned to an intermediate level by addition of 10 μM MeAsp (Figure 3A,B). Similarly, the array disruption allowed signaling but abolished the long-term activity fluctuations in $CheR^+$ $CheB^+$ cells equilibrated in buffer (Figure 3C,D). Importantly, buffer-adapted $CheR^+$ $CheB^+$ CheW-X2 cells had intermediate receptor activity and could respond to both attractant (MeAsp) and repellent (Ni^{2+}) stimuli, *i.e.*, both down- and upregulation of the pathway activity (Figure 3 – Figure Supplement 2). This confirms that the observed loss of fluctuations was not caused by locking the receptor in the extreme activity state.

In summary, these results demonstrate that the observed long-term fluctuations in activity, seen both with and without the receptor methylation system, require receptor clustering.

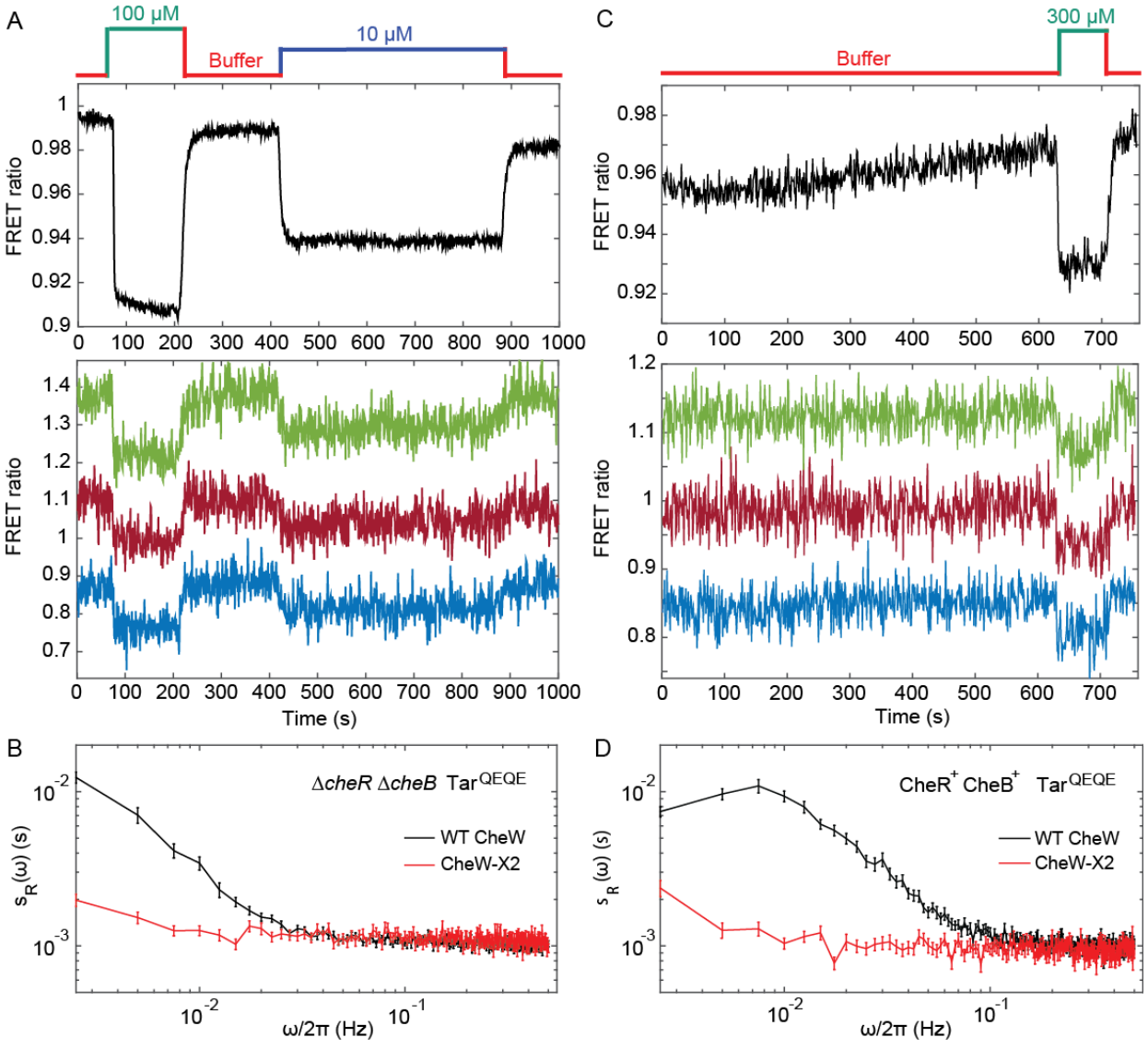

Figure 3. Fluctuation analysis in CheW-X2 cells. (*A*) Population-averaged (upper panel) and typical single-cell (lower panel) measurements of the FRET ratio for Δ*cheR*Δ*cheB* strain carrying CheW-X2 and Tar^{QEQE} as the sole receptor. Cells, which have a high activity in buffer, were first exposed to 100 μM MeAsp (saturating stimulus), and then to 10 μM MeAsp (sub-saturating stimulus), as indicated. The single-cell measurement traces have been shifted along the *y*-axis to facilitate visualization. (*B*) Power spectral density of the FRET ratio fluctuations in CheW-X2 Δ*cheR*Δ*cheB* Tar^{QEQE} cells at intermediate activity (i.e., with 10 μM MeAsp) (red) compared to the equivalent strain

carrying native (wild-type; WT) CheW and at 30 µM MeAsp (black – same data as Figure 2C). Error bars represent SEM, with sample sizes 404 (WT CheW; black) and 208 (CheW-X2; red) cells. (*C*) Same as (A) but for $CheR^+$ $CheB^+$ strain. The activity in buffer is at intermediate level (Figure 3 – Figure Supplement 2), with 300 µM MeAsp completely inhibiting the kinase activity. (*D*) Power spectral density of the FRET ratio fluctuations in $CheR^+$ $CheB^+$ CheW-X2 strain in buffer (red) compared to the native WT CheW (black – same data as Figure 1C). Error bars represent SEM, with sample sizes 265 (WT CheW; black) and 191 (CheW-X2; red) cells.

Fluctuation-dissipation relation for receptor clusters

We next used mathematical analysis to better understand the respective contributions of receptor clustering and the methylation enzymes to the observed fluctuations and to determine whether methylation-independent fluctuations are generated by some out-of-equilibrium random process. We considered the fluctuation-dissipation theorem (FDT), which postulates – *for systems at equilibrium* – that thermal fluctuations of a quantity are related, via temperature, to the response of this quantity to a small externally applied perturbation [64]. The FDT framework can be used to determine whether a system is at equilibrium, by comparing fluctuations and responses to small perturbations *via* their ratio, the so-called effective temperature $T_{\mathrm{eff}}(\omega)$ [65-68]. In equilibrium systems the FDT is satisfied and $T_{\mathrm{eff}}(\omega)$ equals the physical temperature *T*. In out-of-equilibrium (biological) systems, the deviation of $T_{\mathrm{eff}}(\omega)$ from *T* provides a first characterization of the underlying out-of-equilibrium noisy process generating the fluctuations, since $T_{\mathrm{eff}}(\omega)$ is linked to the energy scale and frequency content of such process [65-68].

In our case, the magnitude of activity fluctuations could be expressed as the PSD corrected for the measurement shot noise, $s_R(\omega) - \epsilon_n^2$, where ϵ_n^2 was experimentally determined as the PSD of the receptorless cells. We therefore define the effective temperature as:

$$\frac{T}{T_{\mathrm{eff}}(\omega)} = \frac{G_R(\omega)}{s_R(\omega) - \epsilon_n^2}. \qquad (1)$$

The dissipation $G_R(\omega)$ could be determined by formulating the fluctuation dissipation relation for the activity of individual receptors within the signaling array, using the Ising-like model [45, 69, 70] to describe cooperative receptor interactions as (see Appendix, section 1):

$$G_R(\omega) = -2\,\lambda^2\,\frac{3N^2\langle A\rangle(1-\langle A\rangle)}{N_T}\,\mathrm{Re}\big(\hat{\mathrm{g}}(\omega)\big). \qquad (2)$$

Here $\langle A\rangle$ is the average activity around which fluctuations occur, estimated from experimental data as described above, N_T is the total number of Tar dimers per cell, N is the average number of effectively coupled allosteric signaling units in the cluster, and λ is defined as before. Consistent with several recent reports [44, 56, 63] and with our analysis of the apparent response cooperativity in the CheW-X2 strain (Figure 3 – Figure Supplement 1 and Appendix, section 1.4), we assumed that signaling units within the cluster correspond to trimers of receptor dimers. Finally, $\mathrm{Re}\big(\hat{\mathrm{g}}(\omega)\big)$ is the real part of the Fourier transform of the normalized step response function $g(t)$, which could be experimentally determined by measuring the FRET response to sufficiently small (subsaturating) stepwise attractant stimulation as $g(t) = \Delta R(t)/(-\lambda \mathrm{X}_A^{\infty}\epsilon_0)$, where $(-\lambda \mathrm{X}_A^{\infty}\epsilon_0)$ is the normalized stimulation strength (see Appendix, section 1.3).

For subsaturating stimulation of the non-adapting Δ*cheR*Δ*cheB* cells (Figure 2B), the normalized step response function $g^{-}(t)$ exhibited a relatively rapid initial increase and then slowly approached its final value, possibly with a slight transient overshoot (Figure 4A). Nearly identical response dynamics was observed for weaker stimulations (Figure 4 – Figure Supplement 1), validating the small perturbation assumption of the FDT for this response function measurement. This slow response dynamics is consistent with a previous report that attributed it to gradual stimulation-dependent changes in packing of receptors within clusters [42]. Consistent with this interpretation, the CheW-X2 Δ*cheR*Δ*cheB* strain with disrupted

receptor clustering showed neither comparable latency nor overshoot in its response (Figure 3 – Figure Supplement 3).

As the pathway activity in the CheW-X2 in Δ*cheR*Δ*cheB* strain also showed no long-term fluctuations (Figure 3B,C), we hypothesized that these fluctuations might be indeed caused by the slow response dynamics stimulated by some random process. We thus calculated the corresponding dissipation using Equation (2), considering that under our conditions $N_T \sim 10^4$ [26] and $N \sim 14$ [26, 53, 58, 60] (see Table 1 for all parameter values). At low frequencies, the dissipation $G_R(\omega)$ was approximately equal to the shot-noise corrected $s_R(\omega)$ at $\langle A \rangle \simeq 0.5$ (Figure 4B), as predicted by Equation (1) for equilibrium systems where $T_{\mathrm{eff}}(\omega)$ equals T. Consistently, the corresponding ratio $T/T_{\mathrm{eff}}(\omega)$ was nearly independent of ω and close to unity in the range of frequencies for which $s_R(\omega)$ is above the measurement noise (Figure 4B *Inset*). This suggested that in absence of adaptation enzymes the system is close to equilibrium and thermal fluctuations are the major source of noise. Although the deviation of $T/T_{\mathrm{eff}}(\omega)$ from unity might indicate second-order contributions of out-of-equilibrium processes, it is comparable to what was observed for other equilibrium systems with measurement methods of similar precision [66, 71, 72]. Thus, an equilibrium model can fairly accurately describe the details of observed long-time activity fluctuations in Δ*cheR*Δ*cheB* cells. This agreement suggests that the receptor cluster in these cells largely acts as a passive system, where thermal fluctuations stimulate the long-term response dynamics, possibly due to slow changes in receptor packing within clusters, to generate activity fluctuations.

Furthermore, the PSD of Δ*cheR*Δ*cheB* cells followed the scaling $\langle A \rangle (1 - \langle A \rangle)$, which is expected from the underlying receptor activity being a two-state variable, as evident for subpopulations of cells sorted according to their activity (Figure 4 – Figure Supplement 2), with

354 which our FDT analysis is consistent (Equation (2)). Fluctuations were apparently unaffected by
355 the expression level of Tar, in the tested range of induction (Figure 4 – Figure Supplement 3). In
356 the FDT framework, this implies that N^2/N_T must be constant for varying receptor expression,
357 and previous measurements indeed suggest that the cooperativity rises with the expression level
358 of Tar^{QEQE} in a way that N^2/N_T remains unchanged [26].
359 To evaluate the respective effects of signal amplification and the slow dynamics of the cluster
360 activity response, we performed stochastic simulations of a simple model of sensory complexes
361 without adaptation and under thermal noise (see Appendix, section 4). In this model, receptors
362 are clustered in signaling teams that respond to allosterically amplified free energy changes on an
363 effective time scale averaging the fast switching dynamics and the slow dynamics of the receptor
364 cluster, which accounts qualitatively for the pathway behavior. Expectedly, larger amplification
365 led to larger fluctuations, and the time scale of the fluctuations followed the imposed response
366 time scale of the cluster. Less trivially, slower response also led to higher maximal amplitude of
367 the fluctuations (Figure 4 – Figure Supplement 4).
368

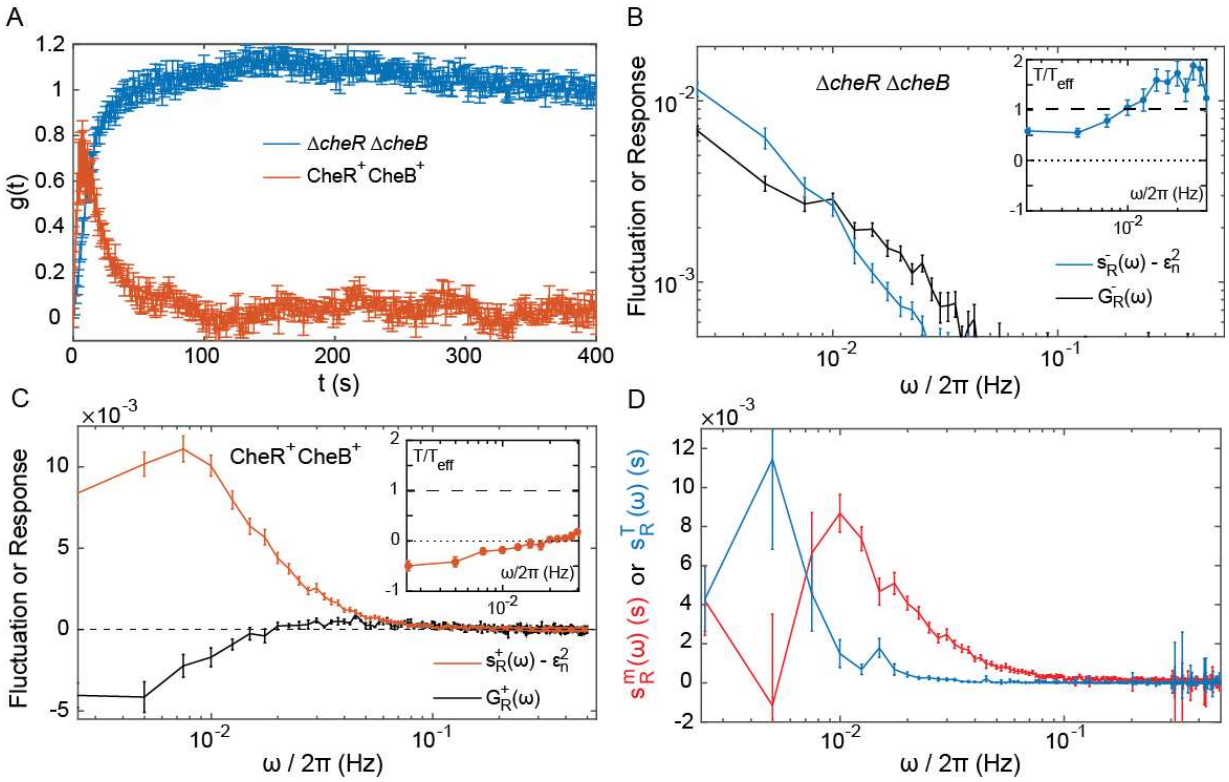

Figure 4. Fluctuation-dissipation analysis of the pathway activity. (*A*) Step response function $g(t)$ both in presence (red) and in absence (blue) of the adaptation enzymes, evaluated in cells expressing Tar^{QEQE} that respond to a step change from buffer to 0.3 µM MeAsp (CheR$^+$ CheB$^+$) or 30 µM MeAsp (Δ*cheR*Δ*cheB*). The step response function was calculated from the measurements shown in Figure 4 – Figure Supplement 5 and in Figure 2B as described in text and in Appendix, section 1.3. (*B,C*) The PSD of the FRET ratio fluctuations $s_R(\omega)$ at $\langle A \rangle = 0.5$ (blue in *B* and red in *C*), and the corresponding dissipation $G_R(\omega)$ (black) calculated using Equation (2), for Δ*cheR*Δ*cheB* (*B*) and CheR$^+$CheB$^+$ (*C*) cells. The measurement shot noise ϵ_n^2, determined as the PSD of the receptorless cells (Figure 1B), was subtracted from $s_R(\omega)$. *Insets* show the ratio between the physical and effective temperatures, calculated using Equation (1). Dashed and dotted lines in *B* and *C* indicate $T/T_{\text{eff}}(\omega) = 1$ and $T/T_{\text{eff}}(\omega) = 0$, respectively. (*D*) Contribution of thermal noise (blue) and the adaptation enzyme dynamics (red) to the PSD in CheR$^+$ CheB$^+$ cells, calculated from Equation (3) as explained in Appendix, section 3. In all panels, error bars represent SEM, with sample sizes for the power spectra calculations being 540 (Δ*cheR*Δ*cheB*) and 468 (CheR$^+$ CheB$^+$; aggregating data from cells expressing Tar^{QEQE} and Tar^{EEEE} as sole receptor) single cells from at least five biological replicates.

Out-of-equilibrium dynamics in presence of adaptation system

The normalized step response function of CheR$^+$ CheB$^+$ cells, $g^+(t)$ (Figure 4A), was determined using weak stimulation by 0.3 µM MeAsp, with the activity change $\Delta A/\langle A\rangle = 0.25$ (Figure 4 – Figure Supplement 5 and Appendix, section 1.3). Describing adaptation according to the classical two-state models of receptors [20, 60, 73], the responses of Δ*cheR*Δ*cheB* and CheR$^+$ CheB$^+$ cells could be linked via the rate of adaptation ω_{RB}, which yielded $\omega_{RB} = 0.06 \pm 0.01$ Hz (Appendix, section 2 and Figure 4 – Figure Supplement 6), consistent with previous estimates [14].

The corresponding dissipation $G_R^+(\omega)$, calculated as above according to Equation (2), differed strongly from the PSD of the activity fluctuations (Figure 4C), confirming that the system operates out of equilibrium. The corresponding $T/T_{\text{eff}}(\omega) << 1$ (Figure 4D *Inset*) is consistent with strong out-of-equilibrium drive. It decreased at low frequencies, crossing zero at $\omega/2\pi \simeq 0.015$ Hz where $T_{\text{eff}}(\omega)$ diverges (Figure 4 – Figure Supplement 7) and dissipation becomes negative. Such crossing indicates a transition to the range of frequencies where the active process dominates [66, 74], with the frequency of divergence of $T_{\text{eff}}(\omega)$ representing interplay between the time scales of the passive receptor response and adaptation (Appendix, section 2.2).

To further separate specific contributions of the methylation system and thermally activated receptor cluster rearrangements to the power spectrum of activity fluctuations in CheR$^+$ CheB$^+$ cells, we followed previous modeling approaches [75-77] (Appendix, section 3). Assuming that thermal noise behaves the same in presence and in absence of the methylation system, $s_R^+(\omega)$ can be decomposed into a ''thermal'' contribution $s_R^T(\omega)$ and a contribution of the methylation noise $s_R^m(\omega)$:

$$s_R^+(\omega) = s_R^m(\omega) + s_R^T(\omega) = s_R^m(\omega) + \left|\frac{g^+(\omega)}{g^-(\omega)}\right|^2 s_R^-(\omega). \quad (3)$$

Although relatively noisy, particularly at low frequencies, $s_R^m(\omega)$ inferred from equation (3) peaked around $\omega_{peak}/2\pi = 0.01$ Hz (Figure 4D), which equals the independently determined adaptation rate (see above), $\omega_{peak} \simeq \omega_{RB} = 0.06$ Hz. The contribution of the thermal noise $s_R^T(\omega)$ had a similar magnitude but dominated at lower frequencies. The power spectrum of the CheR and CheB binding events was inferred from $s_R^m(\omega)$ using the previous model and previous conclusion that the methylation-dependent activity fluctuations mainly arise from the intermittent binding of the small number of CheR and CheB molecules to the receptors [33]. This spectrum was consistent with the common assumption that CheR (CheB) loads and acts only on the inactive (active) receptor (Appendix, section 3 and Figure 4 – Figure Supplement 8).

We further extended our simulation model of the receptor array composed of independent signaling teams, to test whether we can reproduce the observed power spectrum in presence of adaptation enzymes. Consistent with the large excess of receptors compared to the methylation enzymes [29], in these simulations only one CheR (or CheB) molecule can bind to the inactive (respectively active) receptor team, methylate (respectively demethylate) the receptors, and unbind once the team has turned active (respectively inactive) (Appendix, section 4). The simulations agreed qualitatively well with the experiments, including the power spectra of CheR/CheB binding and effective temperature (Figure 4 – Figure Supplement 9), although absolute amplitudes of the fluctuations were clearly underestimated by the model, as already observed in a previous theoretical work [74]. The simulation also reproduced the loss of slow fluctuations upon disruption of clusters in $CheR^+$ $CheB^+$ cells, which arises from the dependence of $s_R(\omega)$ on the size N of signaling teams. In contrast, simulating less efficient neighborhood

assistance by reducing the (de)methylation rate of the bound enzymes had only modest effects (Figure 4 – Figure Supplement 9C).

Discussion

Stochastic activity fluctuations are likely to have major impact on signal processing within cellular networks [1, 3]. Nevertheless, direct visualization and characterization of such fluctuations at the posttranslational level remain limited to a small number of cases [78, 79] primarily due to high requirements for the sensitivity and time resolution of the necessary single-cell measurements. Although fluctuations of the signaling activity can in some cases be deduced from the downstream output of the network, either gene expression [80, 81] or behavior [9, 10, 14, 33], this output may strongly filter and reshape fluctuations. Consequently, the theoretical framework for the analysis of noise at the posttranslational level remains less developed than for variations in gene expression [4, 6].

Here we directly monitored activity fluctuations in the chemotaxis pathway of *E. coli*, a common model for quantitative analysis of signal transduction [43, 82, 83]. One fascinating feature of the chemotaxis pathway is the amplification of chemotactic signals through cooperative interactions within the clusters (arrays) of chemoreceptors, where at least ~10-20 receptor dimers show concerted transitions between active and inactive states [24, 25, 45-48]. The pathway is also robust against external and internal perturbations, largely thanks to its methylation-based adaptation system [20, 52, 84-86]. At the same time, the stochastic activity of the adaptation enzymes was also proposed as the reason for the observed strong variability in the signaling output, *i.e.* the duration of straight runs of the swimming cells [9, 10, 33]. Indeed, inspired by so-

called fluctuation-response theorems, previous analyses established a fluctuation-response relation between the adaptation time to stimuli (called response time) and the typical time scale of fluctuations of the tumbling rate in individual *E. coli* cells [10, 14] – which we confirmed at the level of CheY phosphorylation ($\omega_{peak} \simeq \omega_{RB}$) – demonstrating that behavioral fluctuations originate within the chemotaxis pathway and pointing to the methylation system as their likely cause. Subsequently, the fluctuations in straight run durations were proposed to enhance environmental exploration, partly since the occasional long run allows exploring wider territories [10, 15, 37, 39, 40].

Here we combined experimental and mathematical analyses to demonstrate that both, the adaptation system and receptor clustering contribute to the signaling noise in the chemotaxis pathway. Experimentally, we adapted the FRET-based assay that was previously applied to study average signaling properties in cell populations [18, 24, 26, 42, 44, 50-60], to be used at the single-cell level. Whereas previous studies have relied on the output provided by flagellar motor rotation [9, 14], using FRET enabled us to characterize the activity fluctuations directly, before their amplification by the motor. Our measurements showed that fluctuations can be comparable to the average adapted activity of the pathway and thus significantly larger than previous estimates [32]. This surprisingly large amplitude of fluctuations indicates concerted variations of receptor activity across the signaling arrays containing hundreds to thousands of receptors. Furthermore, we showed that the stochasticity of receptor methylation could not be the sole cause of the pathway noise, because activity fluctuations were also observed in absence of the methylation system. In contrast, disruption of receptor clustering completely abolished these long-term activity fluctuations, even in presence of the methylation system, implying that receptor interactions are essential for the observed fluctuations.

To better understand the nature of the observed fluctuations, we applied analysis based on the fluctuation-dissipation theorem (FDT), following a recent theoretical study [74]. The FDT establishes a fundamental relationship between thermal fluctuations and the response to externally applied perturbations for an equilibrium system. Although being a powerful tool for studying equilibrium and out-of-equilibrium systems in physics [64], so far it has found only limited application in biology [6, 65, 67, 87, 88]. For the chemotaxis system, the FDT in its equilibrium form was used to predict the magnitude of thermally activated ligand binding noise with implications for maximal sensing accuracy [77, 88]. The present approach is also complementary to the previous fluctuation-response analysis mentioned above [10, 14], itself conceptually related to the fluctuation theorems extending the FDT for certain systems in non-equilibrium steady states [14, 89]. Comparison of fluctuations and dissipation to evaluate whether the system deviates from the FDT, together with the analysis of mutants deficient in adaptation and/or clustering, enabled to identify multiple factors contributing to the pathway noise. These factors include (i) the input thermal noise, (ii) the amplification of this noise by cooperative interactions among receptors, (iii) the delayed response function of receptor clusters, and (iv) the dynamics of the methylation system (Figure 5).

Unexpectedly, the activity fluctuations in absence of the adaptation system could be explained for the most part by thermal noise acting on the receptors, which is amplified through the cooperative interactions of clustered receptors and subsequently converted into long-term pathway activity fluctuations by their slow response dynamics (Figure 5A). The contribution of out-of-equilibrium processes to these activity fluctuations seems to be minor if any. This phenomenon demonstrates that thermal noise can induce measurable fluctuations in activity of a cellular network, even in absence of active processes that are usually considered to be the main

497 contributors to cellular dynamics. Even more striking is the amplitude of these fluctuations,
498 suggesting that up to a half of the chemoreceptor array – that may contain thousands of receptors
499 – flips its activity.
500 The slow cluster dynamics was recently observed using fluorescence anisotropy measurements
501 and attributed to the stimulation-induced changes in packing of receptors within clusters [42].
502 Indeed, in our experiments both slow response and activity fluctuations were abolished by
503 mutations that disrupt clustering, suggesting that it corresponds to some large-scale plasticity
504 within the receptor array [44]. Interestingly, such stimulation-induced slow reconfiguration had
505 been also proposed to modulate cooperativity within the receptor array in an earlier theoretical
506 study [69]. Although the precise mechanism behind this slow dynamics was not yet
507 characterized, meaning that it could neither be experimentally disentangled from signal
508 amplification nor mechanistically modeled, our simulations suggest that while slow dynamics
509 sets the time scale of activity fluctuations, both this dynamics and amplification contribute to
510 their amplitude. It thus seems that this previously little considered feature of the receptor array
511 plays a large role in producing and shaping the activity fluctuations.
512 Our analysis also suggests that an effective subunit of the allosteric signaling teams corresponds
513 to one trimer of dimers, rather than a dimer itself as assumed in previous computational models
514 [26, 73]. This conclusion is consistent with several recent studies [44, 56, 63], and it could be
515 easily reconciled with the previous formulations of the Monod-Wyman-Changeux models by
516 rescaling the free-energy change per methylated glutamate by a factor of three. Since large size
517 of the cooperative units implies fewer units per receptor array, it further helps to account for the
518 large activity fluctuations even in absence of the methylation enzymes.

519 Notably, on the studied range of time scales the previously proposed contribution of the high-
520 frequency ligand binding noise [77, 88] to overall fluctuations must be very small, since the
521 observed power spectral densities depended on activity but not on the absolute ligand
522 concentration. The dynamics of CheY/CheZ interaction is also unlikely to contribute to the
523 observed fluctuations because the turnover rate of this complex (> 1 Hz) [29, 52] is above the
524 frequency range of our experiments.
525 In the presence of the adaptation system the noise within receptor arrays is apparently added to
526 the noise coming from the stochasticity of methylation events (Figure 5B), with both noise
527 sources having comparable strength. The adaptation system not only shifts the frequency
528 spectrum of fluctuations but also eliminates the latency of the response to stimuli, thus likely
529 accelerating the response through its negative feedback activity. The statistics of methylation
530 events inferred from the power spectra was compatible with previous understanding of the
531 enzyme kinetics, including the hypothesis that methylation noise is enhanced by the
532 ultrasensitivity to changes in the ratio of methylation enzymes [9, 10]. Nevertheless, receptor
533 clustering is required for the observed activity fluctuations even in presence of the adaptation
534 system (Figure 5C), likely because of signal amplification as well as accelerated adaptation
535 dynamics within clusters due notably to assistance neighborhoods [30, 33, 56]. Our simulations
536 suggested that the former likely plays a more prominent role in generating large activity
537 fluctuations.
538 Altogether, the overall picture of the signaling noise in the chemotaxis pathway is more complex
539 than previously suggested, with the noise being first processed through a slow responding
540 amplifier (the chemoreceptor cluster) and then fed back through the methylation system,

resulting in complex colored fluctuations of the pathway activity and therefore of the swimming behavior.

More generally, our study provides another example of the general relation between fluctuations and response in biological systems and it demonstrates that FDT-based analysis can distinguish between active and passive processes also within an intracellular network. Although activity fluctuations in biological systems are commonly shaped by active, out-of-equilibrium processes, meaning that in many cases the FDT will not be satisfied [14], the properties of a system can nevertheless be inferred when studying the deviation of its behavior from the FDT [65-67, 87]. The approach of quantifying such deviations by means of an effective temperature, or fluctuation-dissipation ratio, has been used in a variety of out-of-equilibrium systems [68], from glasses to biological systems. Although in some systems, *e.g.* glasses, this ratio can have indeed properties normally associated with the thermodynamic temperature, in biological systems the effective temperature rather relates to the energy scale and frequency content of the underlying out-of-equilibrium processes. This relation was previously demonstrated for several systems, including the hair bundle of the inner ear [66] and active transport in eukaryotic cells [65, 67, 87], and we show that it also applies to a signaling pathway. Notably, the present analysis differs both in its aims and technicalities from the aforementioned fluctuation-response analysis [10, 14]. For instance, the FDT breakdown in $CheR^{+}CheB^{+}$ cells does not contradict the previously observed relation between fluctuation and adaptation time scales, since these two observations provide different information: that the noise source encompasses an out-of-equilibrium process and that the fluctuations originate in the chemotaxis pathway, respectively. An interesting emergent feature of our analysis is the negative effective temperature, which arises as a hallmark of the delayed adaptive negative feedback [74]. A similar effect was also observed in inner ear

hair bundles, where it is related to the mechanical adaptation feedback [66]. Negative dissipation associated to the negative temperature was predicted to indicate a reversal of causality, induced here by adaptation [74]: Whereas positive dissipation means that changes in receptor free energy induce activity changes, negative dissipation results from the methylation system counteracting preceding activity changes [74, 76, 90] and actively translating them into free energy changes, thus opposing the passive behavior of the receptors. Importantly, because the FDT-based analysis requires only knowledge of system's fluctuations and its response, it is widely applicable for studying dynamics of diverse cell signaling processes, including those where molecular details are not known.

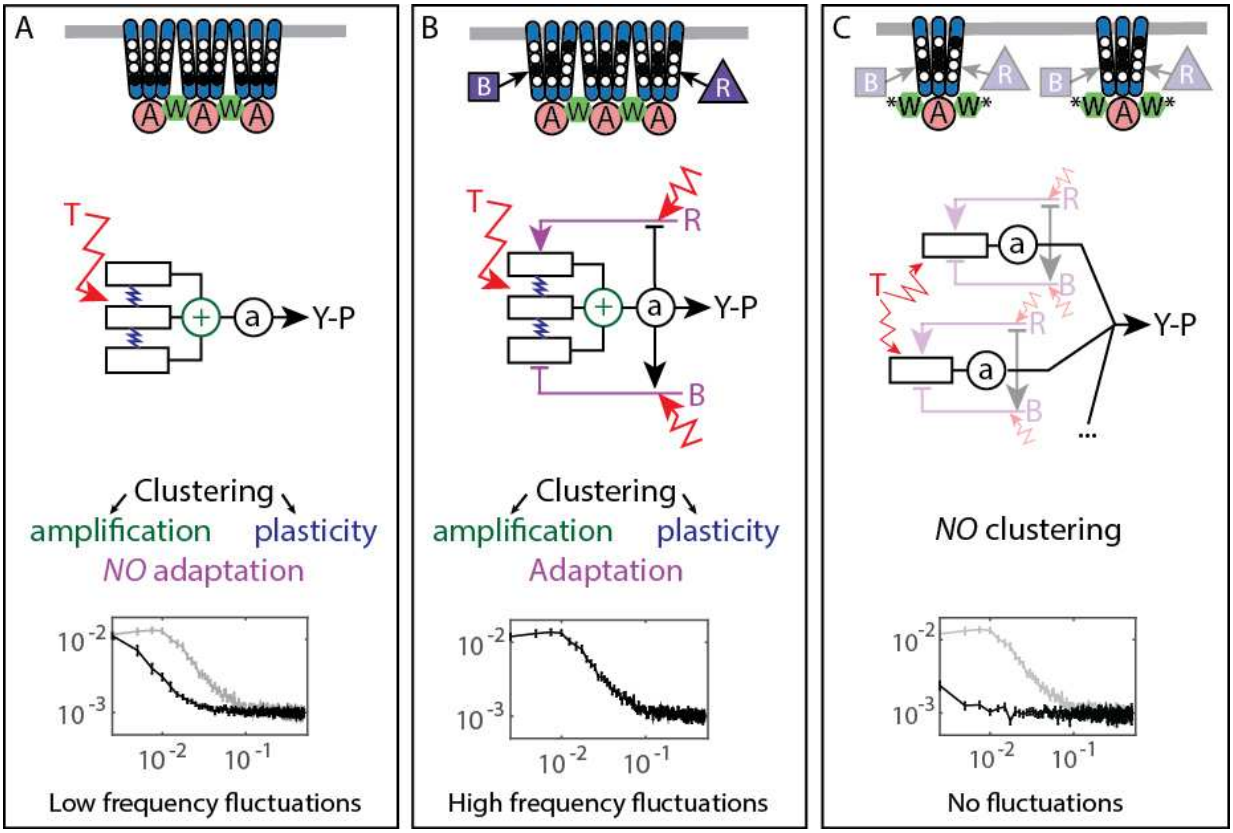

Figure 5. Multiple sources of signaling fluctuation in the chemotaxis pathway. (*A*) In the absence of adaptation enzymes, thermal fluctuations stimulating – and amplified by – the dynamic receptor cluster lead to low frequency fluctuations (<0.01 Hz) around intermediate cluster activity. The blue springs symbolize the plasticity of the receptor

array, the green ⊕ its cooperativity. (*B*) In adapted wild-type cells, thermal fluctuations and fluctuations in the dynamics of CheR and CheB are amplified by the dynamic chemoreceptor cluster, which leads to fluctuations of the activity at frequencies around 0.03 Hz. (*C*) In the absence of clustering, responsive but non-amplifying receptor complexes do not produce observable activity fluctuations, whether or not adaptation enzymes are present. Graphs show the PSD of the FRET ratio measured in each respective case (black). In (A,C) the wild-type curve is shown for comparison (gray).

Materials and methods

Cell growth, media and sample preparation

E. coli strains and plasmids are listed in Supplementary file S1A and S1B, respectively. Cells carrying two plasmids that encode respectively Tar in the indicated modification states and the FRET pair were grown at 30°C overnight in tryptone broth (TB) supplemented with appropriate antibiotics. The culture was subsequently diluted 17:1000 in TB containing antibiotics, 2 µM salicylate (unless otherwise stated) for induction of Tar and 200 µM isopropyl β-D-1-thiogalactopyranoside (IPTG) for induction of the FRET pair, and grown at 34°C under vigorous shaking (275 rpm) to an OD_{600} = 0.55. Bacteria were harvested by centrifugation, washed thrice in tethering buffer (10 mM KPO_4, 0.1 mM EDTA, 1 µM methionine, 10 mM lactic acid, pH 7) and stored at least 20 minutes at 4°C prior to the experiments.

Microscopy

Bacterial cells were attached to poly-lysine coated slides which were subsequently fixed at the bottom of a custom-made, air-tight flow chamber, which enables a constant flow of fresh tethering buffer using a syringe pump (Pump 11 Elite, Harvard Apparatus, Holliston,

Massachusetts, United States) at 0.5 ml/min. This flow was further used to stimulate cells with indicated concentrations of α-methyl-D,L-aspartate (MeAsp). The cells were observed at 40x magnification (NA = 0.95) using an automated inverted microscope (Nikon T*i* Eclipse, Nikon Instruments, Tokyo, Japan) controlled by the NIS-Elements AR software (Nikon Instruments). The cells were illuminated using a 436/20 nm filtered LED light (X-cite exacte, Lumen Dynamics, Mississauga, Canada), and images were continuously recorded at a rate of 1 frame per second in two spectral channels corresponding to CFP fluorescence (472/30 nm) and YFP fluorescence (554/23 nm) using an optosplit (OptoSplit II, CAIRN Research, Faversham, United Kingdom) and the Andor Ixon 897-X3 EM-CCD camera (Andor Technology, Belfast, UK) with EM Gain 300 and exposure time of 1 s (Figure 1 – Figure Supplement 1B). For each measurement, the field of view was chosen to contain both a small region of high density with confluent cells and a few hundred well-separated single cells (Figure 1 – Figure Supplement 1C). During our approximately 30 min long measurements, the focus was maintained using the Nikon perfect focus system.

Image processing and data analysis

The image analysis was performed using the NIS-Elements AR software. The CFP and YFP images, each recorded by a half of the camera chip (256 x 512 px^2, 1 px = 0.40 µm), were aligned with each other by manual image registration. A gray average of the two channels was then delineated to enhance contrast and create binary masks with a user-defined, experiment-specific threshold. Individual cells were detected by segmentation of the thresholded image into individual objects, filtered according to size (3-50 $µm^2$) and shape (excentricity < 0.86). This step resulted in a collection of distinct regions of interest (ROIs) for each frame of the movie.

The ROIs were then tracked from frame to frame, using the NIS build-in tracking algorithm. Only ROIs that could be tracked over the entire duration of the experiment were further analyzed. The selected ROIs were then inspected manually and those not representing individual single cells well attached to the cover glass were discarded. Each individual measurement contained on the order of 100 tracked single cells.

All further analyses were carried out using MATLAB 8.4 R2014b (The MathWorks, Inc., Natick, Massachusetts, United States). For each tracked cell, the average CFP and YFP values over the ROI were extracted as a function of time. These values were also extracted for an ROI corresponding to the confluent population of cells. The ratio R of the YFP signal to the CFP signal was computed for both the single cells and the population, with the population response being used as a reference. Cells with a FRET ratio change of less than 10% of the population response were discarded as unresponsive. The PSD was computed over T=400-frames long segments as

$$s_R(\omega) = \frac{1}{T}\left\langle \frac{\widehat{R_i}(\omega)\widehat{R_i}^*(\omega)}{\overline{R_i}^2} \right\rangle_i , \quad (5)$$

where $\widehat{R_i}(\omega)$ is the discrete Fourier transform of the FRET ratio of cell i at frequency $\omega/2\pi$, $\widehat{R_i}^*$ its complex conjugate, $\overline{\cdot}$ represents a temporal average over the given time interval and $\langle\cdot\rangle_i$ an average over all single cells considered. The error for the PSD was evaluated as $\frac{1}{N_c T}\mathrm{var}\left(\frac{\widehat{R_i}(\omega)\widehat{R_i}^*(\omega)}{\overline{R_i}^2}\right)_i$, where N_c is the number of cells. The time autocorrelation function is simply the inverse Fourier transform of the PSD. The time autocorrelation functions were fitted by $C(t) = C_0 \exp(-t/\tau_0)$, for $t > 0$ to measure the correlation time τ_0, C_0 being a free parameter accounting for the camera white shot noise. Although this fit was moderately accurate ($0.96 \leq R^2 \leq 0.98$ in all cases), it provided a simple estimate of the fluctuation time scale.

Quantification of measurement noise

Contributions of technical fluctuations (vibrations, focus drift, *etc.*) and of the camera shot noise to the noise on the FRET ratio was quantified using fluorescent beads (BD FACSDiva^{TM} CS&T Research beads #655050) that emit both in CFP and in YFP channels. The resulting shot noise was found to be perfectly white (Figure 1 – Figure Supplement 3A). Additional negative control experiments were performed using a receptorless strain, where no CheA-based signaling occurs. In this case, the noise in FRET ratio was also mostly white, except at very low frequency (Figure 1 – Figure Supplement 3B). Where indicated, the power spectra of other strains were corrected by subtracting the power spectrum of the receptorless strain, to obtain the 'pure' activity fluctuation spectra.

Evaluation of the conversion factor λ

The value of λ, 0.10 ± 0.01, converting FRET ratio changes to kinase activity changes, was estimated using data for the Δ*cheR*Δ*cheB* Tar^{QEQE} strain as $\lambda = \langle \bar{R}\,(0) \rangle - \langle \bar{R}(100\,\mu M) \rangle$, the difference, averaged over all cells, between the FRET ratio in buffer, where the activity should be maximal (i.e., equal to one), and the ratio upon saturating stimulation with 100 µM MeAsp. A similar value $\lambda = 0.09 \pm 0.01$ could be estimated in the adaptation-proficient strains, as the difference between the minimal FRET ratio value reached just after stimulation with 100 µM MeAsp and the maximal value reached upon removal of this stimulus. However, this latter value was slightly less precise because it is not certain that full receptor activity is reached upon stimulation removal, and the more reliable Δ*cheR*Δ*cheB* value was used in all cases.

Activity sorting

For Tar^{QEQE} receptors in non-adapting strains, we assumed that all the receptors are fully active in buffer conditions and fully inactive upon stimulation with 100 µM MeAsp. The pathway activity in each cell was thus evaluated as $A = 1 - \frac{\bar{R}(preStim-30\mu M) - \bar{R}(30\ \mu M)}{\bar{R}\ (preStim-100\ \mu M) - \bar{R}(100\ \mu M)}$. The use of the two different prestimulus values in buffer enables to minimize the effect of FRET baseline variation due to bleaching of fluorophores during image acquisition. Cells were then sorted according to their activity and divided into n equally populated subpopulations, and for each subpopulation the average PSD $\langle s_R(\omega)\rangle_A$ at average activity A of the subpopulation was evaluated for the set of frequencies displayed in Figure 4 – Figure Supplement 2. This procedure was implemented for several values of n, namely $n = 10, 9, 6, 5$ and 4, and the whole resulting data was used to plot $\langle s_R(\omega)\rangle_A$ as a function of A (Figure 4 – Figure Supplement 2A).

Acknowledgements

The authors would like to thank R. Somavanshi for assistance with experiments and N.S. Wingreen and S.M. Murray for comments on the manuscript.

Competing Interests

The authors declare no competing interests.

References

[1] ten Wolde P. R., Becker N. B., Ouldridge T. E. and Mugler A. *Fundamental Limits to Cellular Sensing.* Journal of Statistical Physics (2016) **162**, 1395, doi:10.1007/s10955-015-1440-5

[2] Rao C. V., Wolf D. M. and Arkin A. P. *Control, exploitation and tolerance of intracellular noise.* Nature (2002) **420**, 231, doi:10.1038/nature01258

[3] Tsimring L. S. *Noise in biology.* Reports on Progress in Physics (2014) **77**, doi:10.1088/0034-4885/77/2/026601

[4] Raj A. and van Oudenaarden A. *Nature, Nurture, or Chance: Stochastic Gene Expression and Its Consequences.* Cell (2008) **135**, 216, doi:10.1016/j.cell.2008.09.050

[5] Elowitz M. B., Levine A. J., Siggia E. D. and Swain P. S. *Stochastic gene expression in a single cell.* Science (2002) **297**, 1183, doi:10.1126/science.1070919

[6] Paulsson J. *Summing up the noise in gene networks.* Nature (2004) **427**, 415, doi:10.1038/nature02257

[7] Balazsi G., van Oudenaarden A. and Collins J. J. *Cellular Decision Making and Biological Noise: From Microbes to Mammals.* Cell (2011) **144**, 910, doi:10.1016/j.cell.2011.01.030

[8] Eldar A. and Elowitz M. B. *Functional roles for noise in genetic circuits.* Nature (2010) **467**, 167, doi:10.1038/nature09326

[9] Korobkova E., Emonet T., Vilar J. M. G., Shimizu T. S. and Cluzel P. *From molecular noise to behavioural variability in a single bacterium.* Nature (2004) **428**, 574, doi:10.1038/nature02404

[10] Emonet T. and Cluzel P. *Relationship between cellular response and behavioral variability in bacterial chernotaxis.* Proceedings of the National Academy of Sciences of the United States of America (2008) **105**, 3304, doi:10.1073/pnas.0705463105

[11] Berg H. C. and Brown D. A. *Chemotaxis in Escherichia-Coli Analyzed by 3-Dimensional Tracking.* Nature (1972) **239**, 500, doi:10.1038/239500a0

[12] Dufour Y. S., Gillet S., Frankel N. W., Weibel D. B. and Emonet T. *Direct Correlation between Motile Behavior and Protein Abundance in Single Cells.* Plos Computational Biology (2016) **12**, e1005041, doi:10.1371/journal.pcbi.1005041

[13] Spudich J. L. and Koshland D. E., Jr. *Non-genetic individuality: chance in the single cell.* Nature (1976) **262**, 467, doi:10.1038/262467a0

[14] Park H., Pontius W., Guet C. C., Marko J. F., Emonet T. and Cluzel P. *Interdependence of behavioural variability and response to small stimuli in bacteria.* Nature (2010) **468**, 819, doi:10.1038/nature09551

[15] He R., Zhang R. J. and Yuan J. H. *Noise-Induced Increase of Sensitivity in Bacterial Chemotaxis.* Biophysical Journal (2016) **111**, 430, doi:10.1016/j.bpj.2016.06.013

[16] Parkinson J. S., Hazelbauer G. L. and Falke J. J. *Signaling and sensory adaptation in Escherichia coli chemoreceptors: 2015 update.* Trends in Microbiology (2015) **23**, 257, doi:10.1016/j.tim.2015.03.003

[17] Colin R. S., Victor. *Emergent properties of bacterial chemotaxis pathway.* Current Opinion in Microbiology (2017) **39**, 24, doi:10.1016/j.mib.2017.07.004

[18] Shimizu T. S., Tu Y. and Berg H. C. *A modular gradient-sensing network for chemotaxis in Escherichia coli revealed by responses to time-varying stimuli.* Mol Syst Biol (2010) **6**, 382, doi:10.1038/msb.2010.37

[19] Sourjik V. and Berg H. C. *Binding of the Escherichia coli response regulator CheY to its target measured in vivo by fluorescence resonance energy transfer.* Proceedings of the National Academy of Sciences of the United States of America (2002) **99**, 12669, doi:10.1073/pnas.192463199

[20] Barkai N. and Leibler S. *Robustness in simple biochemical networks.* Nature (1997) **387**, 913, doi:10.1038/43199

[21] Hansen C. H., Endres R. G. and Wingreen N. S. *Chemotaxis in Escherichia coli: A Molecular Model for Robust Precise Adaptation.* PLoS Computational Biology (2008) **4**, e1, doi:10.1371/journal.pcbi.0040001

[22] Tu Y., Shimizu T. S. and Berg H. C. *Modeling the chemotactic response of Escherichia coli to time-varying stimuli.* Proceedings of the National Academy of Sciences of the United States of America (2008) **105**, 14855, doi:10.1073/pnas.0807569105

[23] Dunten P. and Koshland D. E. *Tuning the Responsiveness of a Sensory Receptor Via Covalent Modification.* Journal of Biological Chemistry (1991) **266**, 1491,

[24] Sourjik V. and Berg H. C. *Functional interactions between receptors in bacterial chemotaxis.* Nature (2004) **428**, 437, doi:10.1038/nature02406

[25] Li G. Y. and Weis R. M. *Covalent modification regulates ligand binding to receptor complexes in the chemosensory system of Escherichia coli.* Cell (2000) **100**, 357, doi:10.1016/S0092-8674(00)80671-6

[26] Endres R. G., Oleksiuk O., Hansen C. H., Meir Y., Sourjik V. and Wingreen N. S. *Variable sizes of Escherichia coli chemoreceptor signaling teams.* Molecular Systems Biology (2008) **4**, 211, doi:10.1038/Msb.2008.49

[27] Rice M. S. and Dahlquist F. W. *Sites of Deamidation and Methylation in Tsr, a Bacterial Chemotaxis Sensory Transducer.* Journal of Biological Chemistry (1991) **266**, 9746,

[28] Kehry M. R., Bond M. W., Hunkapiller M. W. and Dahlquist F. W. *Enzymatic Deamidation of Methyl-Accepting Chemotaxis Proteins in Escherichia-Coli Catalyzed by the Cheb Gene-Product.* Proceedings of the National Academy of Sciences of the United States of America (1983) **80**, 3599, doi:10.1073/pnas.80.12.3599

[29] Li M. S. and Hazelbauer G. L. *Cellular stoichiometry of the components of the chemotaxis signaling complex.* Journal of Bacteriology (2004) **186**, 3687, doi:10.1128/Jb.186.12.3687-3694.2004

[30] Li M. S. and Hazelbauer G. L. *Adaptational assistance in clusters of bacterial chemoreceptors.* Molecular Microbiology (2005) **56**, 1617, doi:10.1111/j.1365-2958.2005.04641.x

[31] Schulmeister S., Ruttorf M., Thiem S., Kentner D., Lebiedz D. and Sourjik V. *Protein exchange dynamics at chemoreceptor clusters in Escherichia coli.* Proceedings of the National Academy of Sciences of the United States of America (2008) **105**, 6403, doi:10.1073/pnas.071061110

[32] Tu Y. and Grinstein G. *How white noise generates power-law switching in bacterial flagellar motors.* Physical review letters (2005) **94**, 208101, doi:10.1103/PhysRevLett.94.208101

[33] Pontius W., Sneddon M. W. and Emonet T. *Adaptation Dynamics in Densely Clustered Chemoreceptors.* Plos Computational Biology (2013) **9**, e1003230, doi:10.1371/journal.pcbi.1003230

[34] Cluzel P., Surette M. and Leibler S. *An ultrasensitive bacterial motor revealed by monitoring signaling proteins in single cells.* Science (2000) **287**, 1652, doi:10.1126/science.287.5458.1652

[35] Taute K. M., Gude S., Tans S. J. and Shimizu T. S. *High-throughput 3D tracking of bacteria on a standard phase contrast microscope.* Nature Communication (2015) **6**, 8776, doi:10.1038/ncomms9776

[36] Viswanathan G. M., Buldyrev S. V., Havlin S., da Luz M. G. E., Raposo E. P. and Stanley H. E. *Optimizing the success of random searches.* Nature (1999) **401**, 911, doi:10.1038/44831

[37] Matthaus F., Jagodic M. and Dobnikar J. *E. coli Superdiffusion and Chemotaxis-Search Strategy, Precision, and Motility.* Biophysical Journal (2009) **97**, 946, doi:10.1016/j.bpj.2009.04.065

[38] Benichou O., Loverdo C., Moreau M. and Voituriez R. *Intermittent search strategies.* Reviews of Modern Physics (2011) **83**, doi:10.1103/RevModPhys.83.81

[39] Matthaus F., Mommer M. S., Curk T. and Dobnikar J. *On the Origin and Characteristics of Noise-Induced Levy Walks of E. Coli.* Plos One (2011) **6**, e18623, doi:10.1371/journal.pone.0018623

[40] Flores M., Shimizu T. S., ten Wolde P. R. and Tostevin F. *Signaling Noise Enhances Chemotactic Drift of E. coli.* Physical Review Letters (2012) **109**, 148101, doi:10.1103/PhysRevLett.109.148101

[41] Gegner J. A., Graham D. R., Roth A. F. and Dahlquist F. W. *Assembly of an Mcp Receptor, Chew, and Kinase Chea Complex in the Bacterial Chemotaxis Signal Transduction Pathway.* Cell (1992) **70**, 975, doi:10.1016/0092-8674(92)90247-A

[42] Frank V. and Vaknin A. *Prolonged stimuli alter the bacterial chemosensory clusters.* Molecular Microbiology (2013) **88**, 634, doi:10.1111/mmi.12215

[43] Tu Y. *Quantitative modeling of bacterial chemotaxis: signal amplification and accurate adaptation.* Annual Review of Biophysics (2013) **42**, 337, doi:10.1146/annurev-biophys-083012-130358

[44] Pinas G. E., Frank V., Vaknin A. and Parkinson J. S. *The source of high signal cooperativity in bacterial chemosensory arrays.* Proceedings of the National Academy of Sciences of the United States of America (2016) **113**, 3335, doi:10.1073/pnas.1600216113

[45] Duke T. A. J. and Bray D. *Heightened sensitivity of a lattice of membrane receptors.* Proceedings of the National Academy of Sciences of the United States of America (1999) **96**, 10104, doi:10.1073/pnas.96.18.10104

[46] Mello B. A. and Tu Y. *Quantitative modeling of sensitivity in bacterial chemotaxis: the role of coupling among different chemoreceptor species.* Proceedings of the National

Academy of Sciences of the United States of America (2003) **100**, 8223, doi:10.1073/pnas.1330839100

[47] Monod J., Wyman J. and Changeux J. P. *On Nature of Allosteric Transitions - a Plausible Model.* Journal of Molecular Biology (1965) **12**, 88, doi:10.1016/S0022-2836(65)80285-6

[48] Keymer J. E., Endres R. G., Skoge M., Meir Y. and Wingreen N. S. *Chemosensing in Escherichia coli: Two regimes of two-state receptors.* Proceedings of the National Academy of Sciences of the United States of America (2006) **103**, 1786, doi:10.1073/pnas.0507438103

[49] Mello B. A. and Tu Y. *An allosteric model for heterogeneous receptor complexes: understanding bacterial chemotaxis responses to multiple stimuli.* Proc Natl Acad Sci U S A (2005) **102**, 17354, doi:10.1073/pnas.0506961102

[50] Sourjik V., Vaknin A., Shimizu T. S. and Berg H. C. *In vivo measurement by FRET of pathway activity in bacterial chemotaxis.* Methods Enzymology (2007) **423**, 365, doi:10.1016/S0076-6879(07)23017-4

[51] Sourjik V. and Berg H. C. *Receptor sensitivity in bacterial chemotaxis.* Proceedings of the National Academy of Sciences of the United States of America (2002) **99**, 123, doi:10.1073/pnas.011589998

[52] Oleksiuk O., Jakovljevic V., Vladimirov N., Carvalho R., Paster E., Ryu W. S., Meir Y., Wingreen N. S., Kollmann M. and Sourjik V. *Thermal robustness of signaling in bacterial chemotaxis.* Cell (2011) **145**, 312, doi:10.1016/j.cell.2011.03.013

[53] Neumann S., Vladimirov N., Krembel A. K., Wingreen N. S. and Sourjik V. *Imprecision of Adaptation in Escherichia coli Chemotaxis.* PLoS ONE (2014) **9**, e84904, doi:10.1371/journal.pone.0084904

[54] Krembel A. K., Neumann S. and Sourjik V. *Universal response-adaptation relation in bacterial chemotaxis.* Journal of Bacteriology (2014) JB.02171, doi:10.1128/JB.02171-14

[55] Meir Y., Jakovljevic V., Oleksiuk O., Sourjik V. and Wingreen N. S. *Precision and Kinetics of Adaptation in Bacterial Chemotaxis.* Biophysical Journal (2010) **99**, 2766, doi:10.1016/j.bpj.2010.08.051

[56] Frank V., Pinas G. E., Cohen H., Parkinson J. S. and Vaknin A. *Networked Chemoreceptors Benefit Bacterial Chemotaxis Performance.* MBio (2016) **7**, e01824, doi:10.1128/mBio.01824-16

[57] Krembel A., Colin R. and Sourjik V. *Importance of Multiple Methylation Sites in Escherichia coli Chemotaxis.* PLoS One (2015) **10**, e0145582, doi:10.1371/journal.pone.0145582

[58] Neumann S., Lovdok L., Bentele K., Meisig J., Ullner E., Paldy F. S., Sourjik V. and Kollmann M. *Exponential Signaling Gain at the Receptor Level Enhances Signal-to-Noise Ratio in Bacterial Chemotaxis.* Plos One (2014) **9**, e0087815, doi:10.1371/journal.pone.0087815

[59] Neumann S., Grosse K. and Sourjik V. *Chemotactic signaling via carbohydrate phosphotransferase systems in Escherichia coli.* Proceedings of the National Academy of Sciences of the United States of America (2012) **109**, 12159, doi:10.1073/pnas.1205307109

[60] Clausznitzer D., Oleksiuk O., Løvdok L., Sourjik V. and Endres R. G. *Chemotactic Response and Adaptation Dynamics in Escherichia coli.* PLoS Computational Biology (2010) **6**, e1000784, doi:10.1371/journal.pcbi.1000784

[61] Berg H. C. and Tedesco P. M. *Transient-Response to Chemotactic Stimuli in Escherichia-Coli.* Proceedings of the National Academy of Sciences of the United States of America (1975) **72**, 3235, doi:10.1073/pnas.72.8.3235

[62] Gasquet C. and Witomski P. *Fourier analysis and applications: filtering, numerical computation, wavelets, volume 30 of Texts in applied mathematics.* (1999) Springer-Verlag, Berlin, Germany

[63] Li M. and Hazelbauer G. L. *Selective allosteric coupling in core chemotaxis signaling complexes.* Proceedings of the National Academy of Sciences of the United States of America (2014) **111**, 15940, doi:10.1073/pnas.1415184111

[64] Kubo R. *Fluctuation-Dissipation Theorem.* Reports on Progress in Physics (1966) **29**, 255, doi:10.1088/0034-4885/29/1/306

[65] Robert D., Nguyen T. H., Gallet F. and Wilhelm C. *In Vivo Determination of Fluctuating Forces during Endosome Trafficking Using a Combination of Active and Passive Microrheology.* Plos One (2010) **5**, e10046, doi:10.1371/journal.pone.0010046

[66] Martin P., Hudspeth A. J. and Julicher F. *Comparison of a hair bundle's spontaneous oscillations with its response to mechanical stimulation reveals the underlying active process.* Proceedings of the National Academy of Sciences of the United States of America (2001) **98**, 14380, doi:10.1073/pnas.251530598

[67] Mizuno D., Tardin C., Schmidt C. F. and MacKintosh F. C. *Nonequilibrium mechanics of active cytoskeletal networks.* Science (2007) **315**, 370, doi:10.1126/science.1134404

[68] Cugliandolo L. F. *The effective temperature.* Journal of Physics a-Mathematical and Theoretical (2011) **44**, doi:10.1088/1751-8113/44/48/483001

[69] Hansen C. H., Sourjik V. and Wingreen N. S. *A dynamic-signaling-team model for chemotaxis receptors in Escherichia coli.* Proceedings of the National Academy of Sciences of the United States of America (2010) **107**, 17170, doi:10.1073/pnas.1005017107

[70] Shimizu T. S., Aksenov S. V. and Bray D. *A spatially extended stochastic model of the bacterial chemotaxis signalling pathway.* Journal of Molecular Biology (2003) **329**, 291, doi:10.1016/S0022-2836(03)00437-6

[71] Wang P., Song C. M. and Makse H. A. *Dynamic particle tracking reveals the ageing temperature of a colloidal glass.* Nature Physics (2006) **2**, 526, doi:10.1038/nphys366

[72] Abou B. and Gallet F. *Probing a nonequilibrium Einstein relation in an aging colloidal glass.* Physical Review Letters (2004) **93**, 160603, doi:10.1103/PhysRevLett.93.160603

[73] Mello B. A. and Tu Y. *Effects of adaptation in maintaining high sensitivity over a wide range of backgrounds for Escherichia coli chemotaxis.* Biophysical journal (2007) **92**, 2329, doi:10.1529/biophysj.106.097808

[74] Sartori P. and Tu Y. H. *Free Energy Cost of Reducing Noise while Maintaining a High Sensitivity.* Physical Review Letters (2015) **115**, 118102, doi:10.1103/PhysRevLett.115.118102

[75] Clausznitzer D. and Endres R. G. *Noise characteristics of the Escherichia coli rotary motor.* Bmc Systems Biology (2011) **5**, 151, doi:10.1186/1752-0509-5-151

[76] Sartori P. and Tu Y. *Noise filtering strategies in adaptive biochemical signaling networks: Application to E. coli chemotaxis.* Journal of statistical physics (2011) **142**, 1206, doi:10.1007/s10955-011-0169-z

[77] Aquino G., Clausznitzer D., Tollis S. and Endres R. G. *Optimal receptor-cluster size determined by intrinsic and extrinsic noise.* Physical Review E (2011) **83**, 021914, doi:10.1103/Physreve.83.021914

[78] Conlon P., Gelin-Licht R., Ganesan A., Zhang J. and Levchenko A. *Single-cell dynamics and variability of MAPK activity in a yeast differentiation pathway.* Proceedings of the National Academy of Sciences of the United States of America (2016) **113**, E5896, doi:10.1073/pnas.1610081113

[79] Aoki K., Kumagai Y., Sakurai A., Komatsu N., Fujita Y., Shionyu C. and Matsuda M. *Stochastic ERK Activation Induced by Noise and Cell-to-Cell Propagation Regulates Cell Density-Dependent Proliferation.* Molecular Cell (2013) **52**, 529, doi:10.1016/j.molcel.2013.09.015

[80] Paliwal S., Iglesias P. A., Campbell K., Hilioti Z., Groisman A. and Levchenko A. *MAPK-mediated bimodal gene expression and adaptive gradient sensing in yeast.* Nature (2007) **446**, 46, doi:10.1038/nature05561

[81] Bowsher C. G. and Swain P. S. *Identifying sources of variation and the flow of information in biochemical networks.* Proceedings of the National Academy of Sciences of the United States of America (2012) **109**, E1320, doi:10.1073/pnas.1119407109

[82] Sourjik V. and Wingreen N. S. *Responding to chemical gradients: bacterial chemotaxis.* Current Opinion in Cell Biology (2012) **24**, 262, doi:10.1016/j.ceb.2011.11.008

[83] Micali G. and Endres R. G. *Bacterial chemotaxis: information processing, thermodynamics, and behavior.* Current Opinion in Microbiology (2016) **30**, 8, doi:10.1016/j.mib.2015.12.001

[84] Yi T. M., Huang Y., Simon M. I. and Doyle J. *Robust perfect adaptation in bacterial chemotaxis through integral feedback control.* Proceedings of the National Academy of Sciences of the United States of America (2000) **97**, 4649, doi:10.1073/pnas.97.9.4649

[85] Kollmann M., Lovdok L., Bartholome K., Timmer J. and Sourjik V. *Design principles of a bacterial signalling network.* Nature (2005) **438**, 504, doi:10.1038/nature04228

[86] Alon U., Surette M. G., Barkai N. and Leibler S. *Robustness in bacterial chemotaxis.* Nature (1999) **397**, 168, doi:10.1038/16483

[87] Chevry L., Colin R., Abou B. and Berret J. F. *Intracellular micro-rheology probed by micron-sized wires.* Biomaterials (2013) **34**, 6299, doi:10.1016/j.biomaterials.2013.05.002

[88] Bialek W. and Setayeshgar S. *Physical limits to biochemical signaling.* Proceedings of the National Academy of Sciences of the United States of America (2005) **102**, 10040, doi:10.1073/pnas.0504321102

[89] Seifert U. *Stochastic thermodynamics, fluctuation theorems and molecular machines.* Reports on Progress in Physics (2012) **75**, 126001, doi:10.1088/0034-4885/75/12/126001

[90] Lan G., Sartori P., Neumann S., Sourjik V. and Tu Y. H. *The energy-speed-accuracy trade-off in sensory adaptation.* Nature Physics (2012) **8**, 422, doi:10.1038/Nphys2276

[91] Skoge M. L., Endres R. G. and Wingreen N. S. *Receptor-receptor coupling in bacterial chemotaxis: Evidence for strongly coupled clusters.* Biophysical Journal (2006) **90**, 4317, doi:10.1529/biophysj.105.079905

[92] Kalinin Y. V., Jiang L., Tu Y. and Wu M. *Logarithmic sensing in Escherichia coli bacterial chemotaxis.* Biophys J (2009) **96**, 2439, doi:10.1016/j.bpj.2008.10.027

[93] Vladimirov N., Lovdok L., Lebiedz D. and Sourjik V. *Dependence of Bacterial Chemotaxis on Gradient Shape and Adaptation Rate.* Plos Computational Biology (2008) **4**, e1000242, doi:10.1371/journal.pcbi.1000242

[94] Berg H. C. *The rotary motor of bacterial flagella.* Annual Review of Biochemistry (2003) **72**, 19, doi:10.1146/annurev.biochem.72.121801.161737

[95] Peng C. K., Mietus J., Hausdorff J. M., Havlin S., Stanley H. E. and Goldberger A. L. *Long-range anticorrelations and non-Gaussian behavior of the heartbeat.* Phys Rev Lett (1993) **70**, 1343, doi:10.1103/PhysRevLett.70.1343

[96] Clausznitzer D., Oleksiuk O., Lovdok L., Sourjik V. and Endres R. G. *Chemotactic Response and Adaptation Dynamics in Escherichia coli.* Plos Computational Biology (2010) **6**, e1000784, doi:10.1371/journal.pcbi.1000784

Supplementary Figures

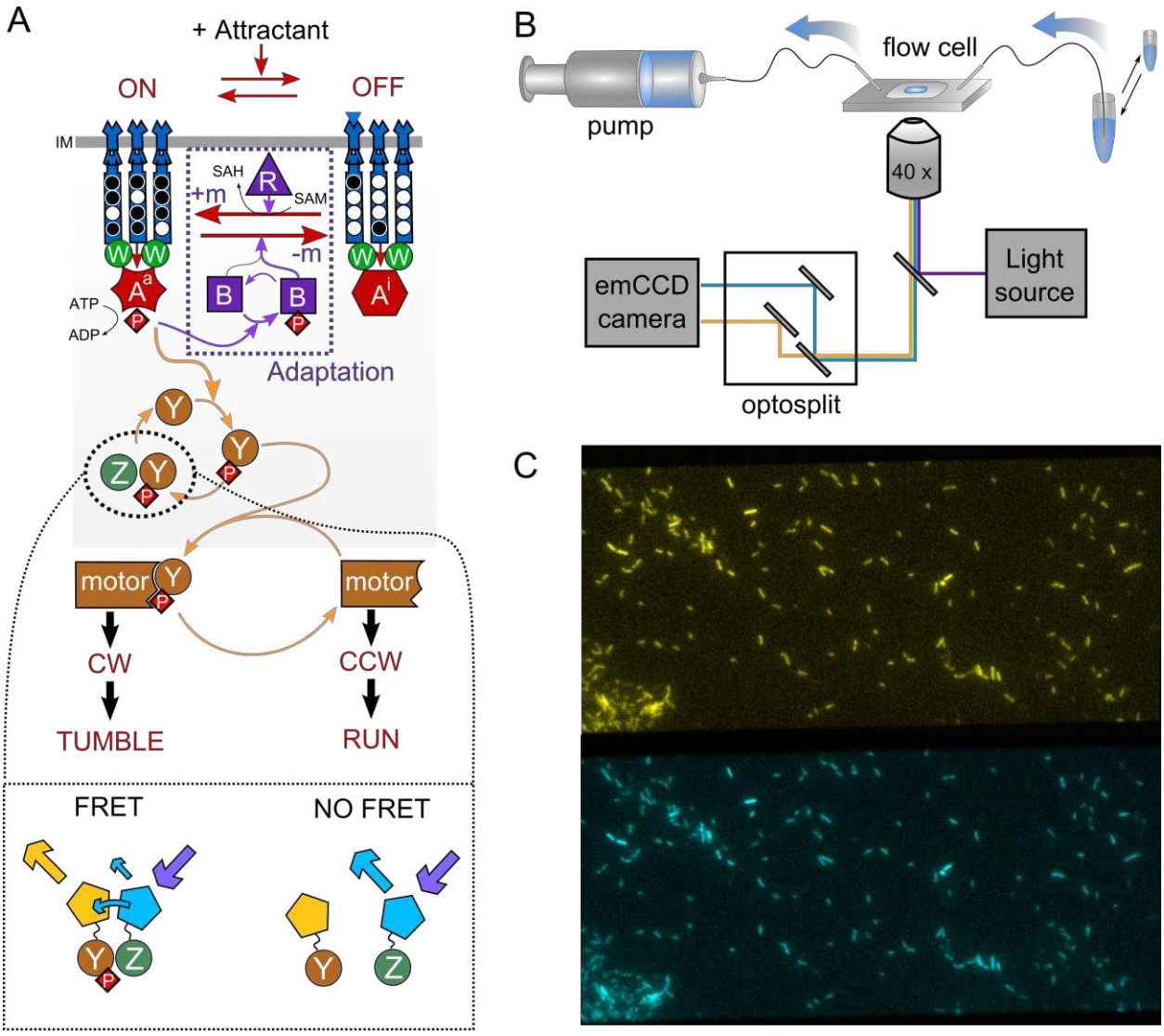

963

964 **Figure 1 – Figure Supplement 1. Schematic representation of the FRET experiment.** (A)
965 The phosphorylation-dependent monitoring of the chemotaxis pathway activity via FRET. CheY
966 and CheZ are tagged with the two components of a FRET pair of fluorophores, so that the level
967 of energy transfer represents the amount of CheY-CheZ interaction. This quantity reflects then
968 the fraction of phosphorylated CheY-P, which represents the average fraction of active CheA
969 (A^a) on the second time scale, because of the rapid cycle of (de)phosphorylation of CheY by
970 $CheA^a$ and CheZ. See text for further explanations. (B) Schematic of the experimental device.
971 Media containing chemoeffectors are flown over the cells attached to a coverslip. Cell

fluorescence is observed simultaneously in two spectral channels separated by an optosplit and an EM-CCD camera. (C) Typical recorded image, showing in the order of a hundred single cells and a small group of cells, the FRET measurement of which is used as a reference during the experiment.

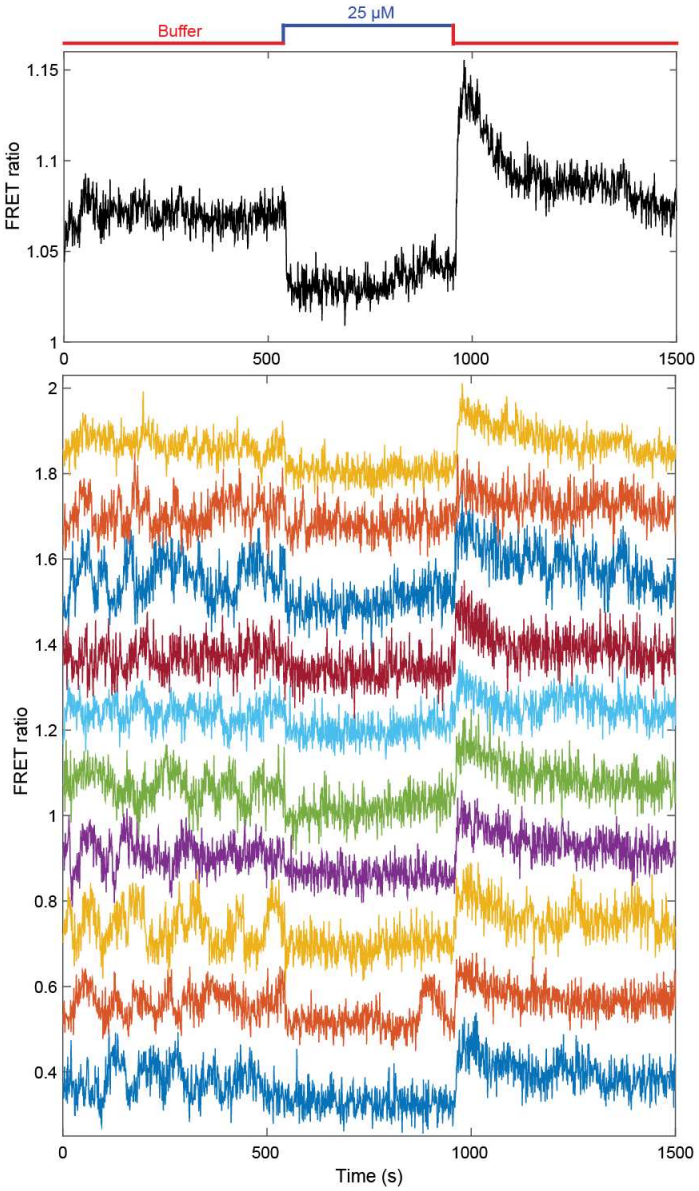

Figure 1 – Figure Supplement 2. Additional FRET measurement for CheR^{+} CheB^{+} cells. Population averaged FRET ratio (top) and corresponding single cell FRET ratios (bottom), for a typical FRET experiment, with adaptation-proficient strain expressing Tar^{QEQE} as the sole receptor. Cells initially adapted in buffer were stimulated with 25 µM MeAsp, before returning to buffer. FRET ratios for individual cells have been shifted to facilitate visualization.

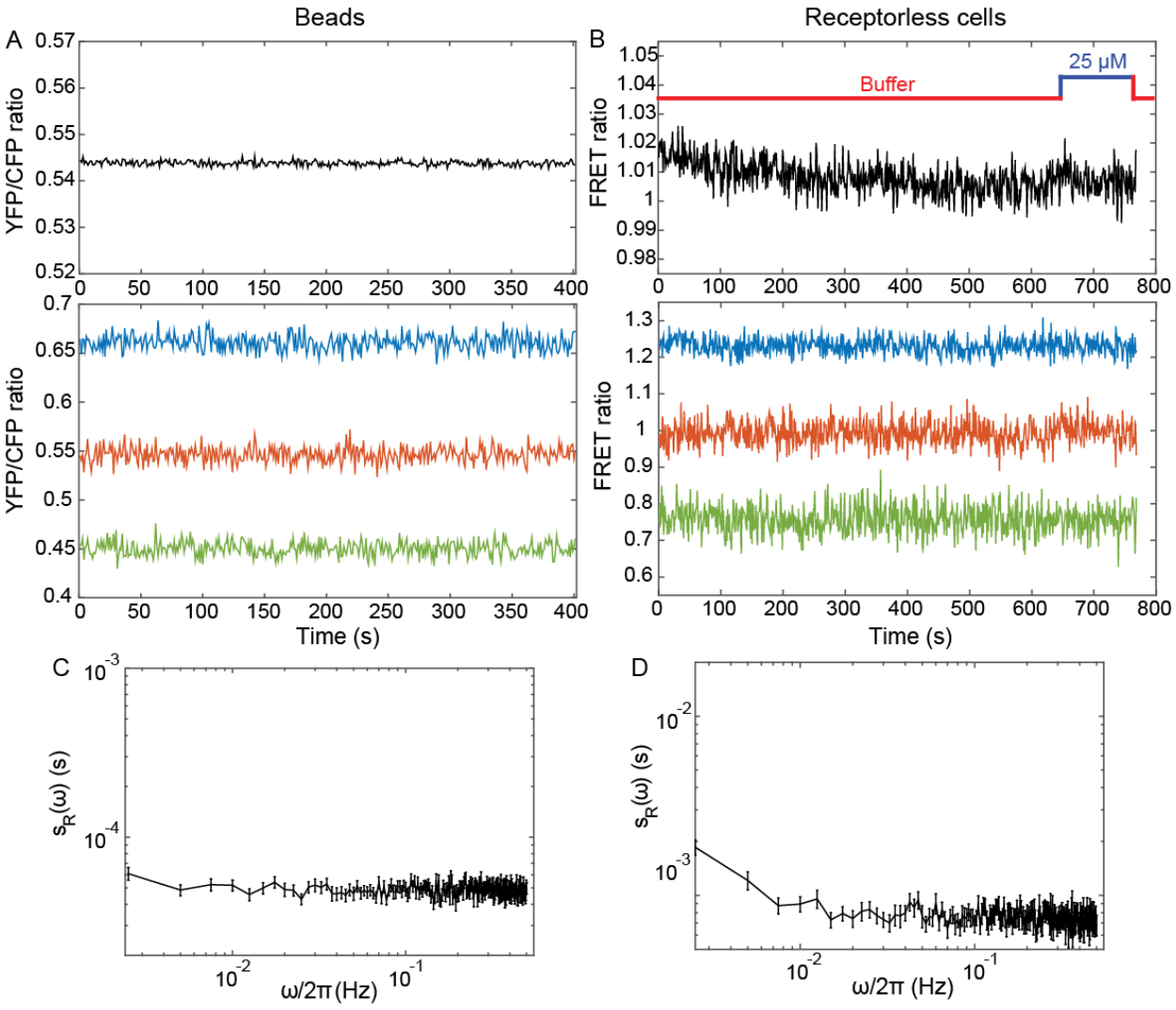

Figure 1 – Figure Supplement 3. Negative controls. (A,B) Average (top) and individual (bottom) measurements of the YFP/CFP ratio for fluorescent beads emitting both in CFP and YFP channels (A) and for receptorless cells expressing FRET pair (B). (C,D) The corresponding PSDs of the fluorescent beads and of the receptorless cells. Error bars represent standard errors of the mean (SEM) and sample sizes are 189 (beads) and 103 (receptorless strain) single objects.

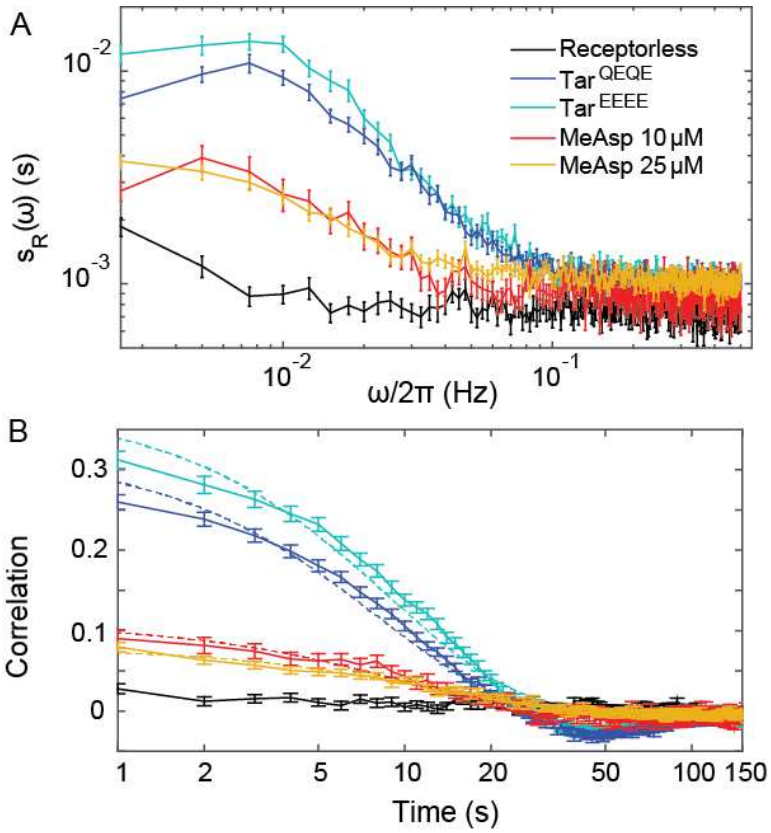

Figure 1 – Figure Supplement 4. Additional analyses for CheR$^+$ CheB$^+$ cells. Same as Figure 1B,C but also including the PSDs (A) and time autocorrelation functions (B) of the FRET ratio measured for CheR$^+$ CheB$^+$ cells expressing Tar^{EEEE} and adapted in buffer or expressing Tar^{QEQE} and adapted to 25 µM MeAsp. The error bars represent SEM, and the sample sizes are 103 (receptorless strain), 203 (Tar^{EEEE} in buffer), 265 (Tar^{QEQE} in buffer), 69 (10 µM) and 219 (25 µM) single cells coming from at least three independent experiments in each case.

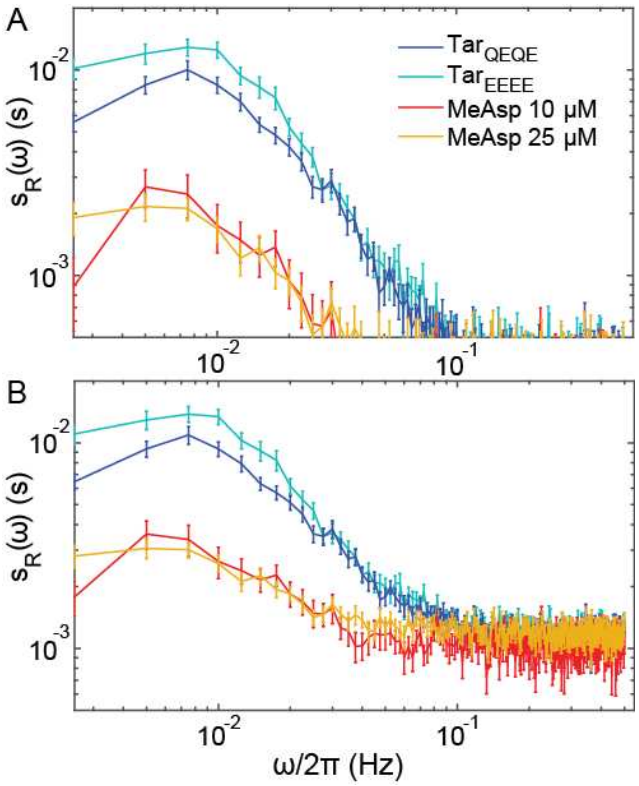

Figure 1 – Figure Supplement 5. Correction of the PSDs for CheR$^+$ CheB$^+$ cells for measurement noise. (A) The PSDs for the different conditions (colors as in Figure Supplement 4) from which the PSD of the receptorless strain (representing measurement noise) was subtracted. (B) Same curves as (A) but with added constant value (9×10^{-4} s), in order to compare with Figure 1B. Statistics is as in Figure 1 – Figure supplement 4.

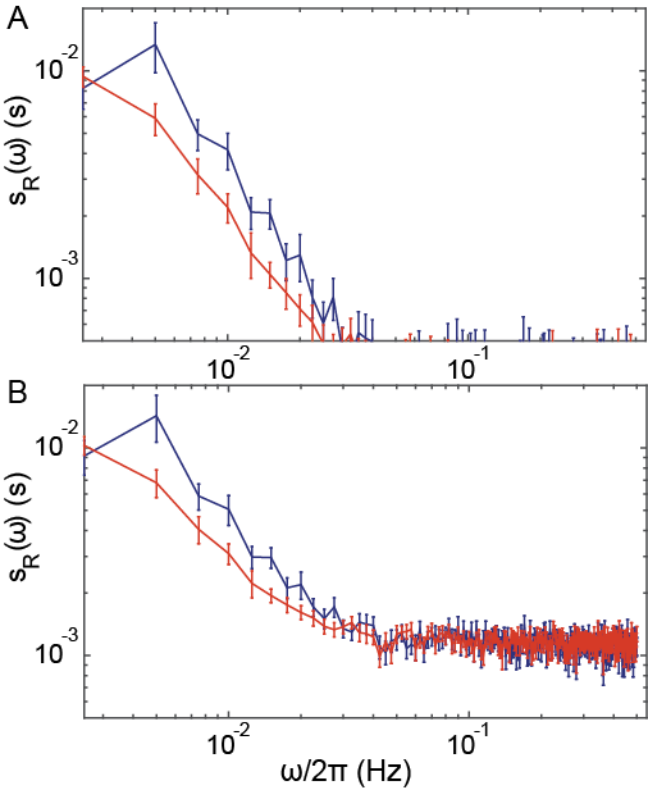

Figure 2 – Figure Supplement 1. Correction of the PSDs for Δ*cheR*Δ*cheB* cells for measurement noise. Same as Figure 1 – Figure Supplement 5 but for Δ*cheR*Δ*cheB* cells. Statistics is as in the main Figure 2.

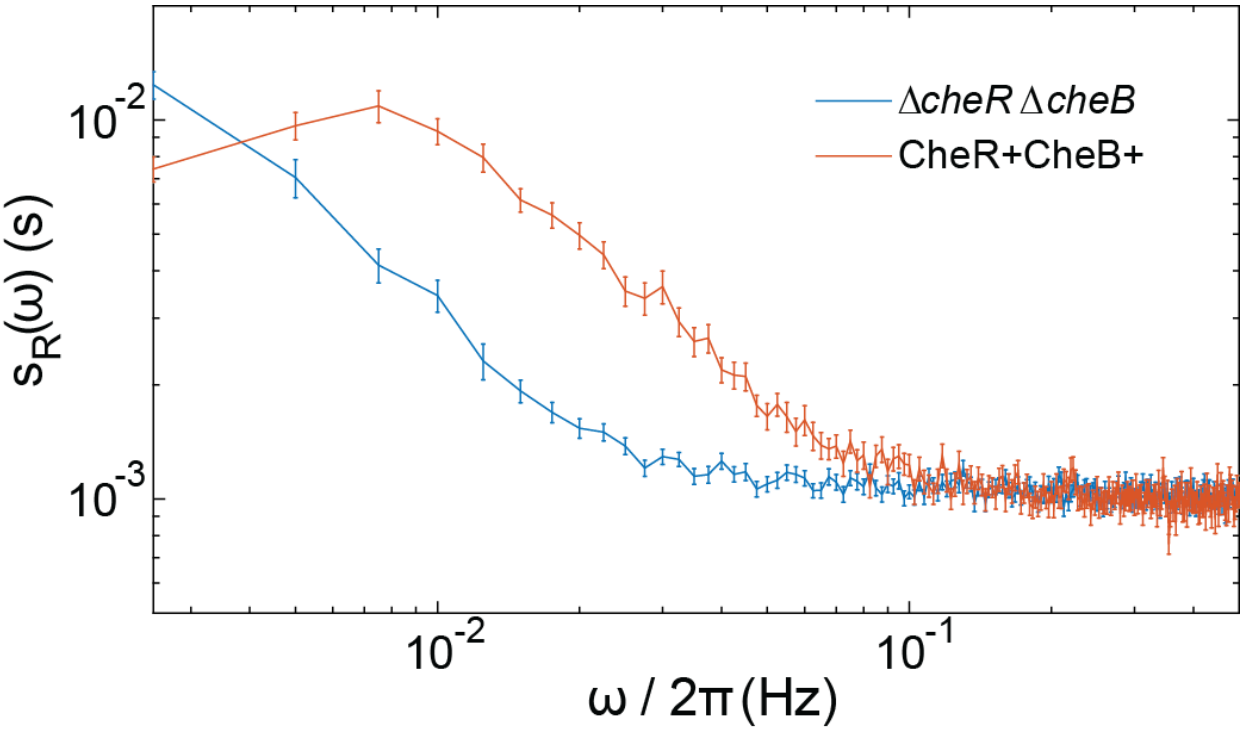

Figure 2 – Figure Supplement 2. Comparison of Δ*cheR*Δ*cheB* and CheR$^+$ CheB$^+$ power spectra. The PSDs of the FRET ratio are plotted for the Δ*cheR*Δ*cheB* strain expressing Tar^{QEQE} as sole receptor and stimulated with 30 µM MeAsp (blue) and the CheR$^+$ CheB$^+$ strain expressing Tar^{QEQE} as sole receptor and adapted in buffer (red). The error bars represent standard errors of the mean (SEM), and the sample sizes are 265 (CheR$^+$ CheB$^+$) and 540 (Δ*cheR*Δ*cheB*) single cells coming from at least three independent experiments in each case.

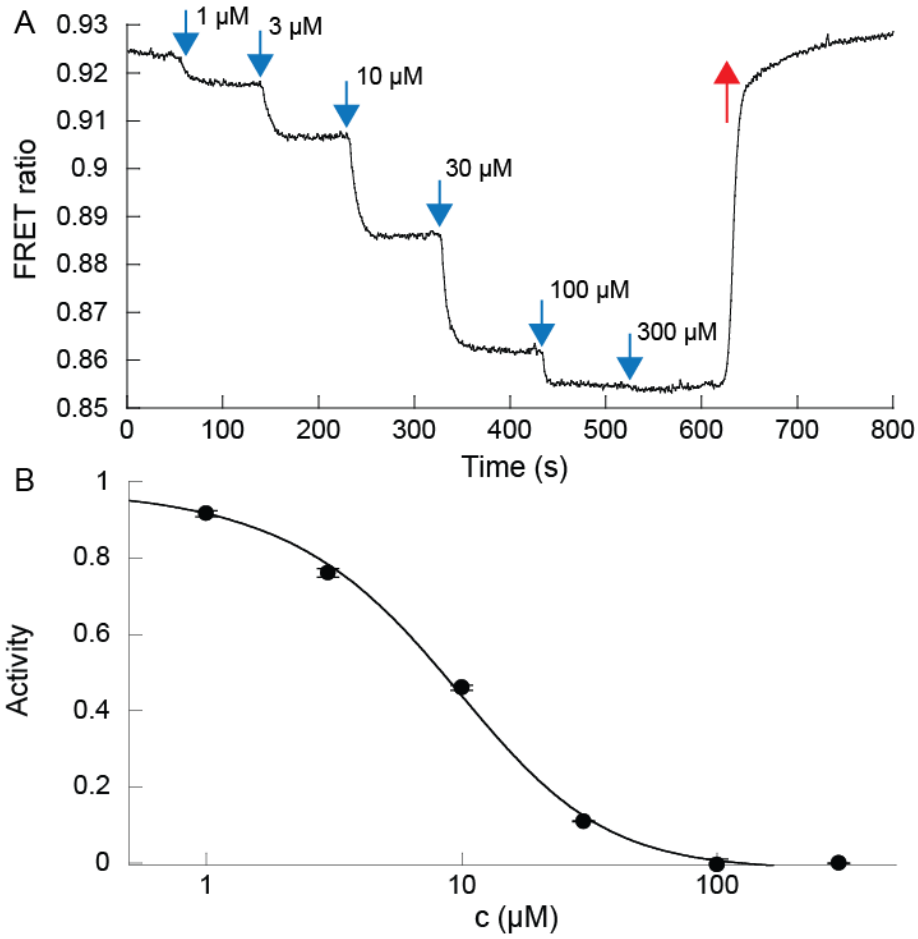

Figure 3 – Figure Supplement 1. Dose response to MeAsp of Δ*cheR*Δ*cheB* CheW-X2 cells expressing Tar^{QEQE}. (*A*) Example of the FRET ratio (R) decreasing as increasing amounts of MeAsp were delivered to the cells. (*B*) The activity averaged over two biological replicates was estimated as $(R(c) - R_{min})/(R_{max} - R_{min})$, plotted as a function of MeAsp concentration *c*, and fitted using the Monod-Wyman-Changeux model, assuming a free energy difference in absence of ligand $\gamma(m = 2) = -1$, yielding a cooperativity number N = 1.73 and a binding constant to inactive receptors K_{OFF} = 3.92 μM. Fitting with a Hill function yields a Hill exponent H = 1.4 and a concentration of half-maximal response EC_{50} = 8.3 μM. Error bars indicate SEM. Measurements were carried out on confluent populations of cells.

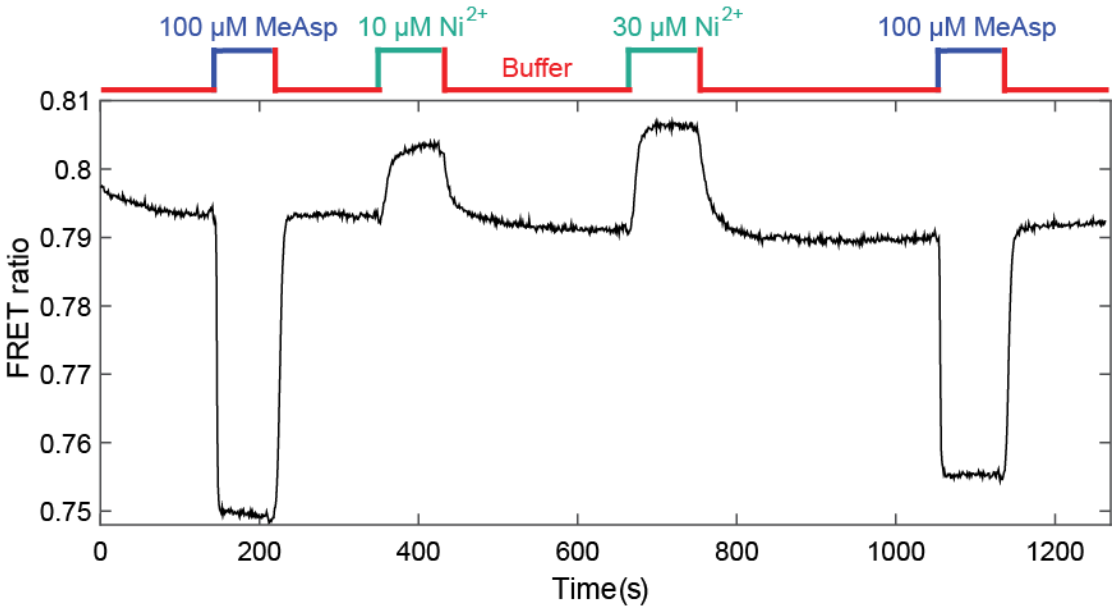

Figure 3 – Figure Supplement 2. Response of CheR^{+} CheB^{+} strain expressing CheW-X2 and Tar^{QEQE} to attractant MeAsp and repellent Ni^{2+}. The activity dropped in response to MeAsp and increased in response to Ni^{2+}, added at indicated concentrations, demonstrating that the cells have indeed an intermediate level of adapted kinase activity. The buffer for this experiment did not contain EDTA, an ion chelator for Ni^{2+}.

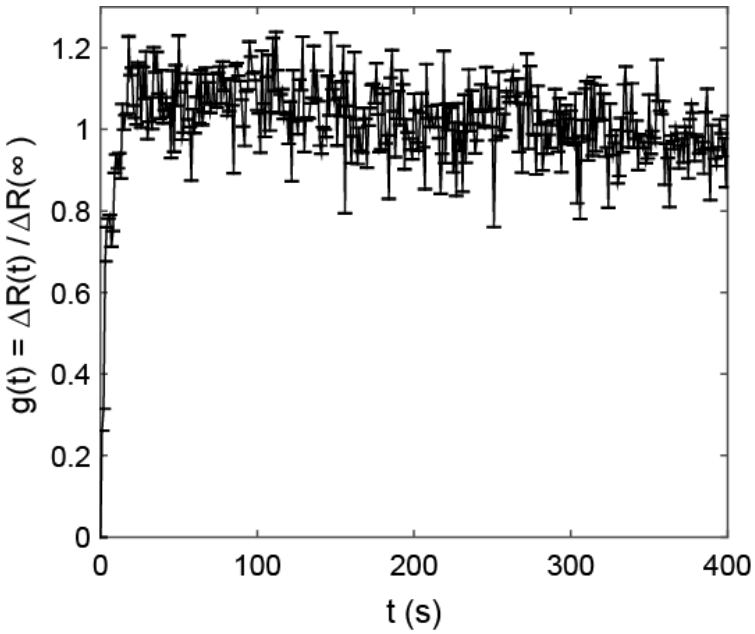

Figure 3 – Figure Supplement 3. Response function for Δ*cheR*Δ*cheB* CheW-X2 cells expressing Tar^{QEQE} as sole receptor. The strain was subjected to 10 µM MeAsp to measure the response. Error bars indicate SEM and sample size is 120 single cells, in 3 biological replicates.

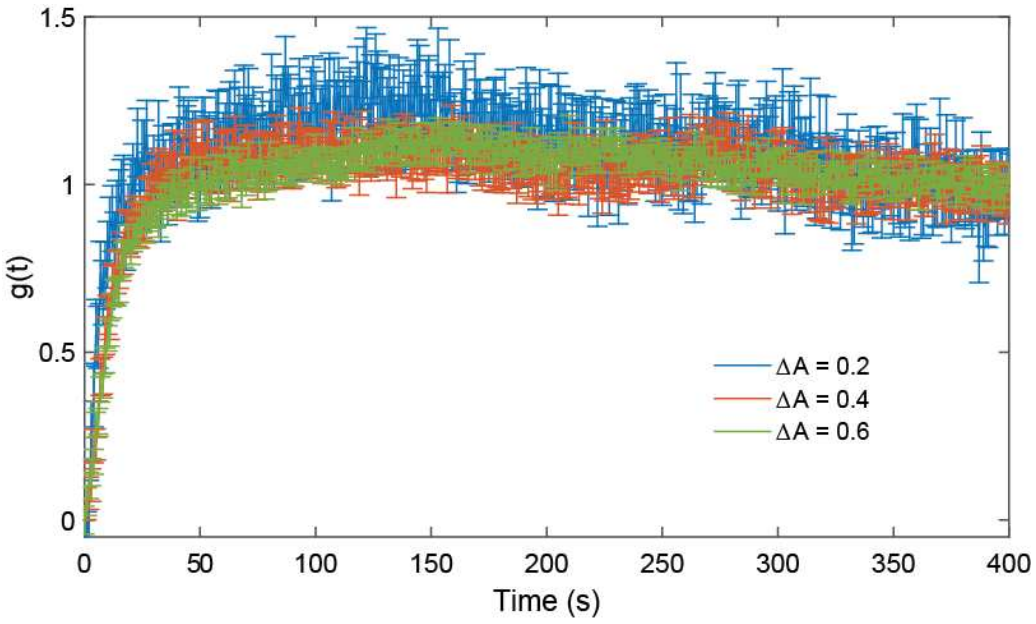

Figure 4 – Figure Supplement 1. Validation of the linear response regime in Δ*cheR*Δ*cheB* cells. Response functions measured for stimulations by increasing MeAsp concentration from 25 to 30 µM, corresponding to an average activity change of 0.2 (blue), from 0 to 25 µM, corresponding to an average activity change of 0.4 (red), and from 0 to 30 µM corresponding to an average activity change of 0.6 (green; data from the main figure). Error bars represent SEM and sample sizes are 339 ($\Delta A = 0.2$ and $\Delta A = 0.4$) and 540 ($\Delta A = 0.6$) single cells in at least three biological replicates.

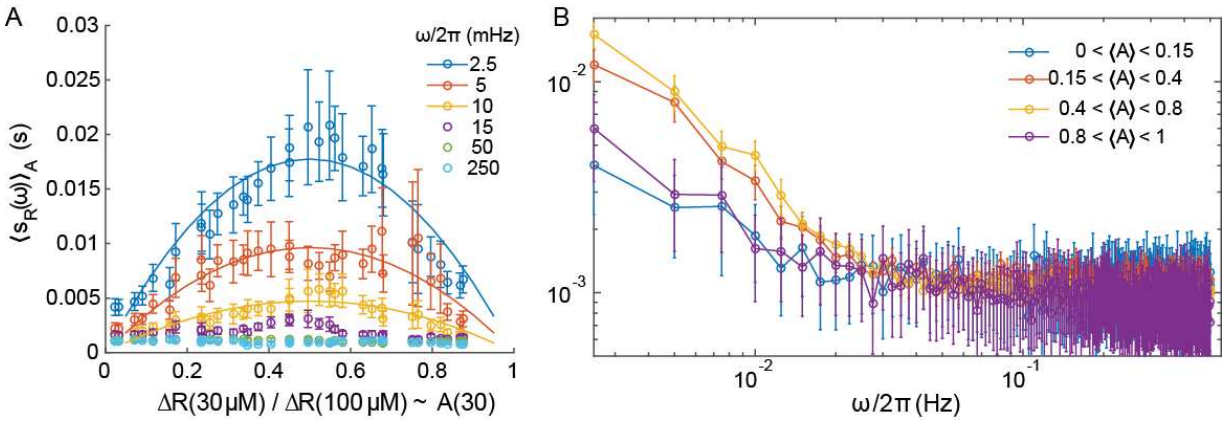

Figure 4 – Figure Supplement 2. Power spectral density computed on subsets of the cell populations sorted according to their activity. (A) The PSD as a function of the average activity of the subsets, for the indicated frequencies (dots) in the Δ*cheR*Δ*cheB* strain expressing Tar^{QEQE}. The lines correspond to best fits by $\langle s_R(\omega)\rangle_A = C(\omega)A(30)\big(1 - A(30)\big)$ for each frequency considered. (B) The PSD as a function of frequency for subsets of cells sorted according to their activity as indicated in the legend. The error bars correspond to SEM, sample sizes are as described in Materials and methods, varying from 54 to 135 cells depending on the point, taken from at least 5 biological replicates.

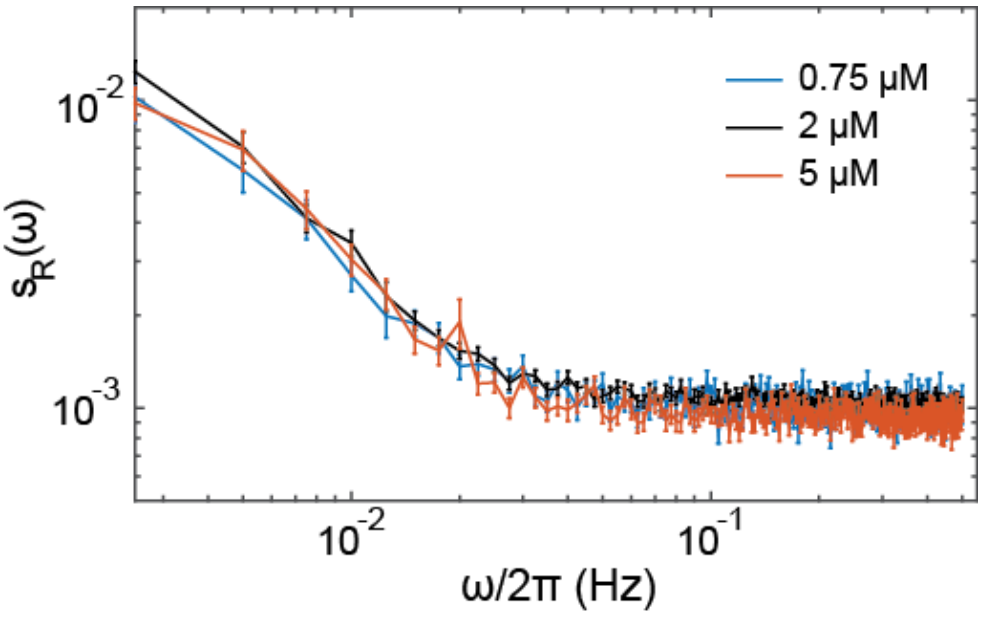

Figure 4 – Figure Supplement 3. Effect of the receptor expression level on the noise in Δ*cheR*Δ*cheB* cells. The Δ*cheR*Δ*cheB* strain expressing Tar^{QEQE} as the sole receptor from a plasmid under salicylate induction, was induced by 0.75 μM, 2 μM (standard experimental condition used in the main text) or 5μM salicylate, resulting in approximately two-fold difference between the protein numbers [26]. The power spectral density of fluctuation in cells prestimulated with 30 μM MeAsp, with average activity A = 0.5, was the same in all conditions. Error bars indicate SEM and sample sizes are 237 (5μM), 540 (2 μM) and 187 (0.75 μM) cells in at least three biological replicates.

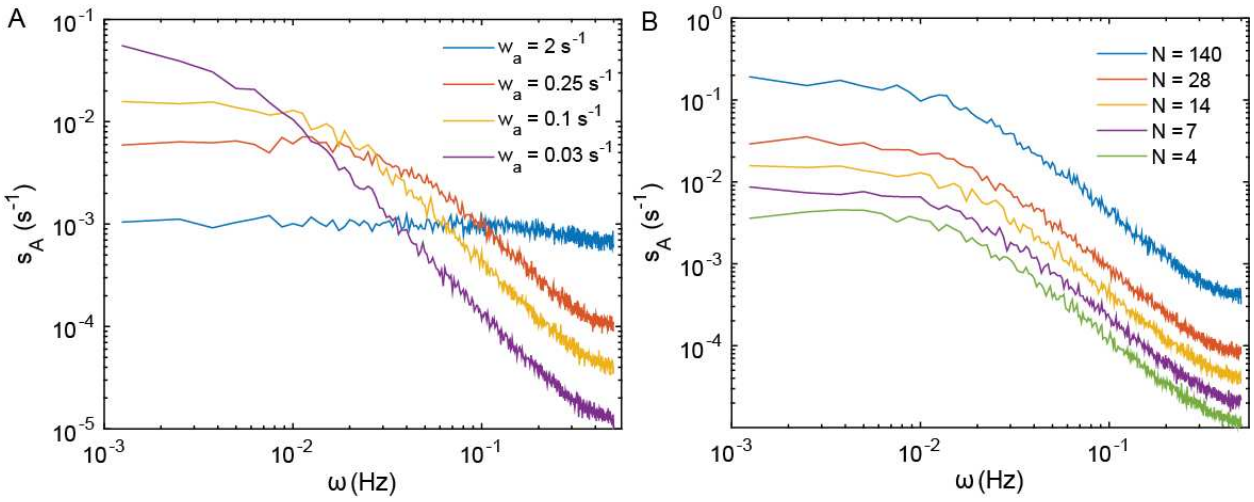

1077

1078 **Figure 4 – Figure Supplement 4. Power spectra of thermal fluctuations in a simulated**
1079 **model of the sensory cluster.** The model describes behavior of cooperative receptor complexes
1080 without adaptation (see Appendix, section 4). Dependence of the PSD of the mean activity of the
1081 receptor cluster $s_A(\omega)$ on the rate of cluster response w_a to free energy perturbations at fixed
1082 number of allosteric units per team N = 14 (A) and on N at fixed w_a = 0.25 s^{-1} (B). The total
1083 number of chemoreceptors was kept constant in all cases.

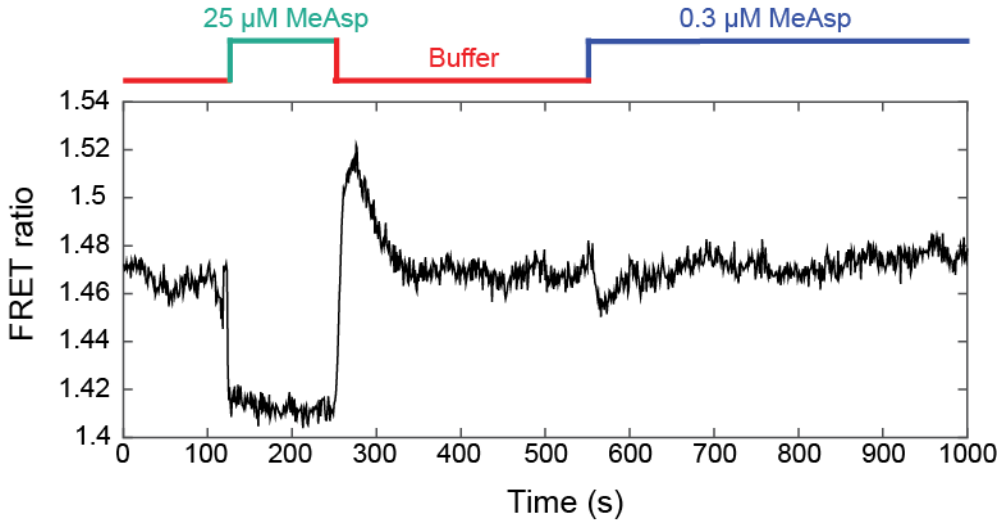

Figure 4 – Figure Supplement 5. Example of FRET measurement used for the evaluation of $g^{+}(t)$. A CheR^{+} CheB^{+} strain expressing Tar^{QEQE} as sole receptor and the CheY-YFP/CheZ-CFP FRET pair, equilibrated in buffer (red), was briefly stimulated with a saturating amount of MeAsp (25 µM; green) to evaluate the FRET ratio at zero activity, re-equilibrated in buffer, and then stimulated with a subsaturating amount of MeAsp (0.3 µM; blue). The FRET ratio was measured on an area of confluent cells. Normalized responses to 0.3 µM MeAsp from five independent replicates of this experiment were averaged to compute the step response function of Figure 4A.

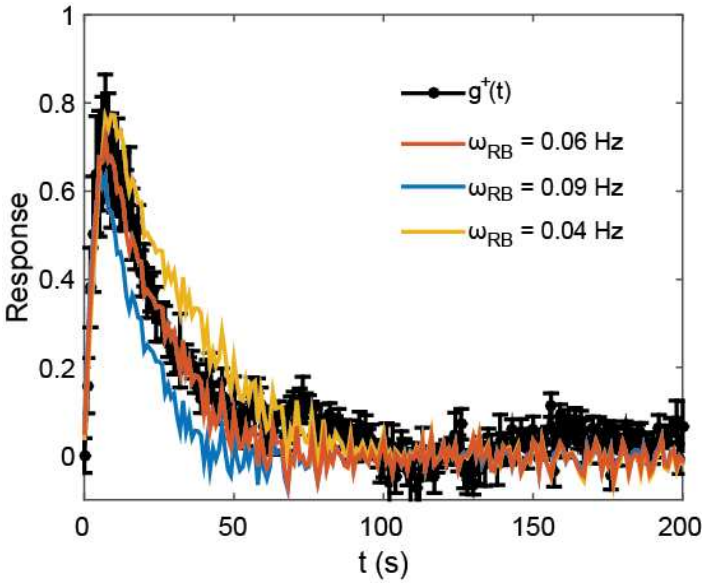

Figure 4 – Figure Supplement 6. Evaluation of the adaptation time. The normalized step response function in CheR$^+$ CheB$^+$, $g^+(t)$, from Figure 4A is plotted alongside its fits by Equation (A.30) of the Appendix, using the normalized step response function in Δ*cheR*Δ*cheB* strain, $g^-(t)$, and the rate of adaptation at the activity level ω_{RB}, for various values of ω_{RB}. The best fit was with $\omega_{RB} = 0.06$. The response function was measured over five areas of confluent cells from as many independent experiments.

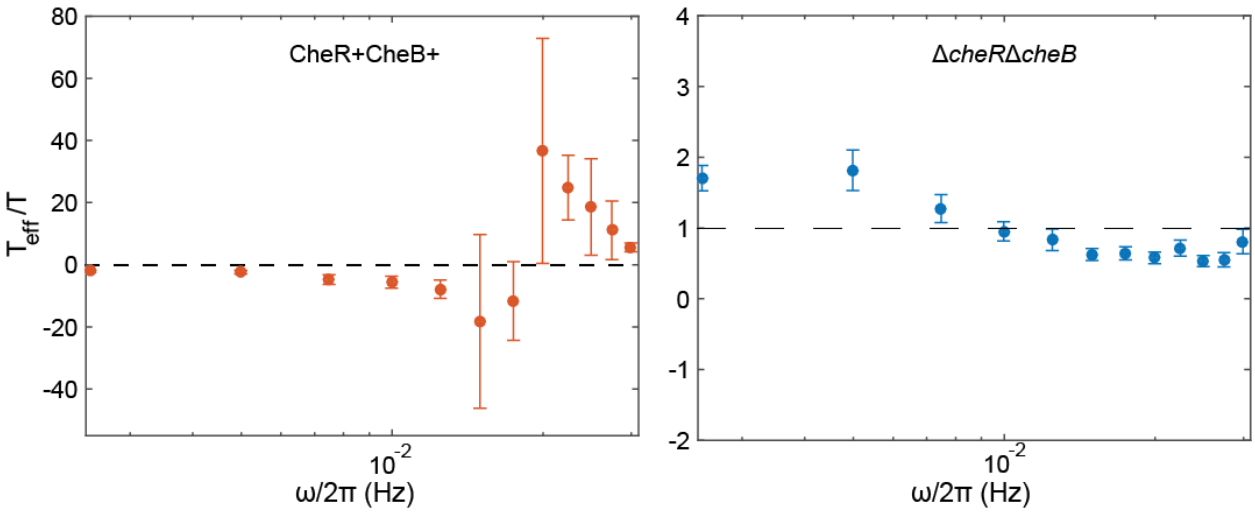

Figure 4 – Figure Supplement 7. Calculated effective temperatures. Plots show the inverse of the quantities plotted in insets of Figure 4B,C, for Δ*cheR*Δ*cheB* and for $CheR^+$ $CheB^+$ cells respectively. Dashed lines represent $T_{\mathrm{eff}} = 0$ ($CheR^+$ $CheB^+$) and $T_{\mathrm{eff}} = T$ (Δ*cheR*Δ*cheB*). Error bars and statistics are as in the main figure.

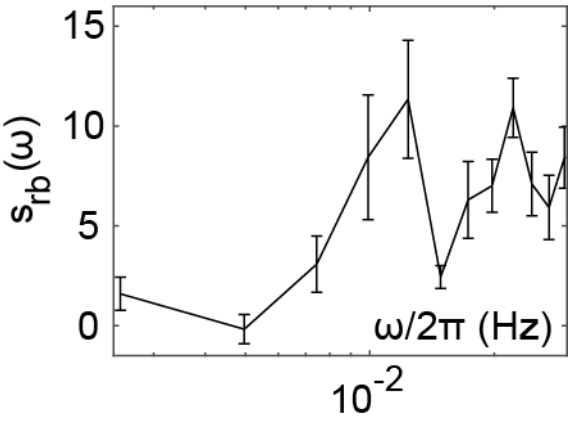

Figure 4 – Figure Supplement 8. Inferred spectrum of the binding dynamics of CheR and CheB. Spectrum was calculated in the frequency range where measurement noise is not dominant, using Equation (A.37). Error bars represent SEM, sample size as in the main figure.

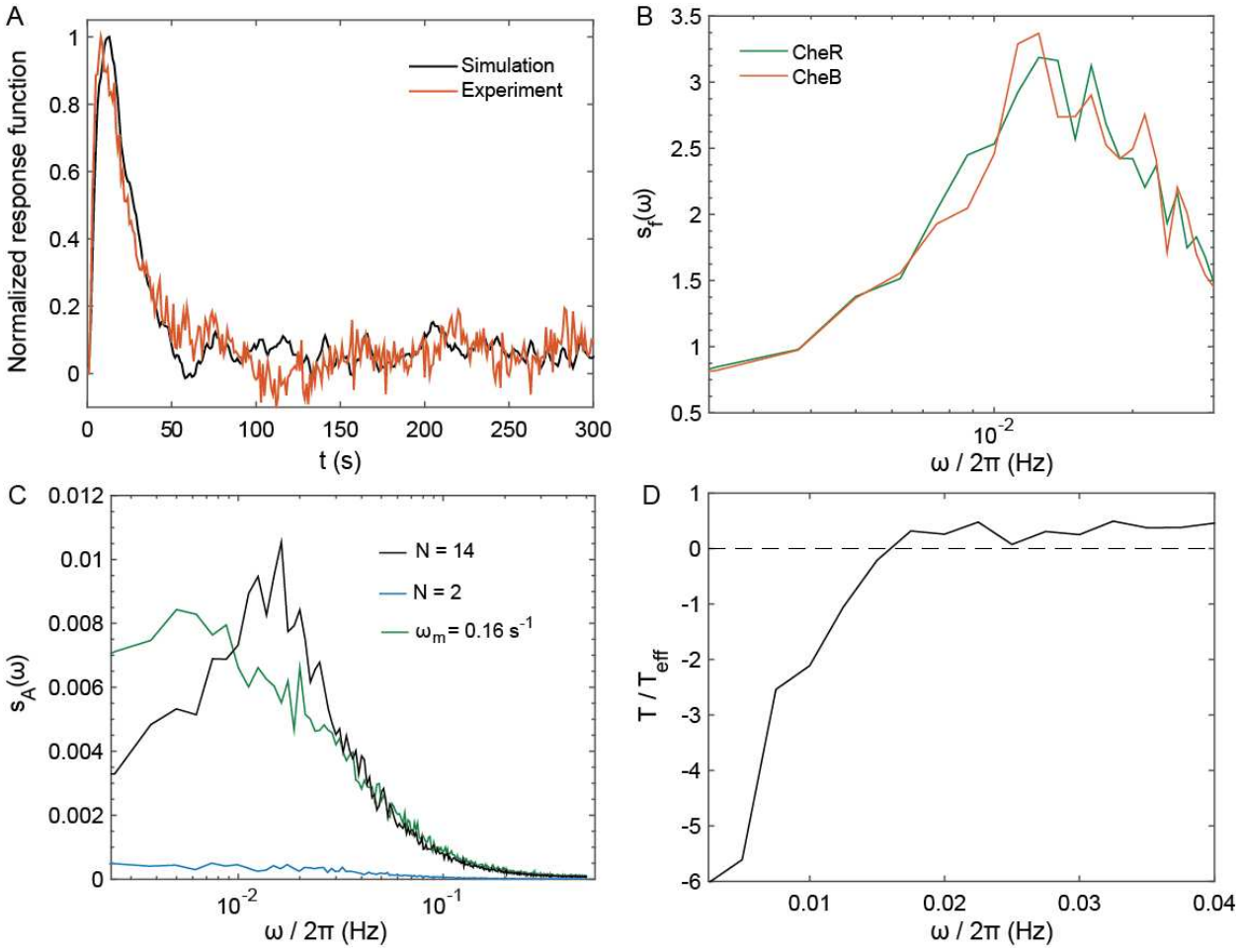

Figure 4 – Figure Supplement 9. Simulation of the pathway activity fluctuations in adapting cells. (A) Simulated response function for the model described in section 4 of Appendix. Comparison with experiments was used to calibrate the time scales of the model. A unique time scale $w_a = 0.25$ s^{-1} was used to model the response of the cluster to free energy perturbations, averaging fast switching and long-term cluster dynamics, which is then not fully accounted for in this model (as in Figure Supplement 4). (B) Power spectrum of CheR and CheB binding to the receptors, showing features similar to its experimental equivalent, plotted in inset of Figure 4D. (C) The PSD of the level of phosphorylated CheY in the model simulations (black), which shows similarities with the contribution of methylation-enzymes dynamics to the

PSD of the FRET ratio plotted in main Figure 4D. The PSD amplitude in the simulation was 100 times smaller than its experimental counterpart (since $s_R = \lambda^2 s_A \simeq 0.01\, s_A$), indicating that activity perturbations 10 times smaller than in experiment. The PSD was also determined when the cooperativity was reduced from its standard value of 14 to 2, mimicking the CheW-X2 strain (blue); and when the specific rate of (de)methylation was decreased from its standard value $\omega_m = 1$ to 0.16 s^{-1}, mimicking reduced efficiency of (de)methylation in absence of neighborhood assistance (green). (D) Inverse effective temperature inferred from (A) and (C) in the simulations, showing behavior similar to the experiments, notably the characteristic sign inversion as in Figure 4C. Differences emerged at very low frequencies, presumably because the model does not take long-term receptor array dynamics into account. In the simulated MWC model of cooperative teams, the fluctuation-dissipation relation can be written for the receptor team, which leads to effective temperature values similar to the experiments (see Appendix, section 4).

Supplementary File S1. List of strains and plasmids used in the study

Table 1. Parameters of the FDT analysis

Parameter	Value
λ	0.10 ± 0.01
N	14
$\langle A \rangle$	0.5
X_A^{∞}	$N\langle A \rangle(1 - \langle A \rangle)$
N_T	10^4
ϵ_n^2	$0.9\ 10^{-3}$

Appendix

This Appendix presents four partially independent theoretical derivations of equations and concepts presented in the main text.

1. Modeling activity fluctuations in the framework of fluctuation-dissipation relation

1.1. Fluctuation dissipation relation and effective temperature

In a system at equilibrium, a fluctuation-dissipation relation links the thermal fluctuations of any physical quantity to its response to an external small perturbation applied to the system via the temperature. It extends the corresponding fluctuation-response relation, which links the amplitudes of the fluctuation and the response, including their evolution in time. For the quantity a, it reads [64]:

$$-\frac{d}{dt}C_a(t,0) = kT\frac{\partial \Delta a(t)}{\partial \Delta h(0)}, \qquad (A.1)$$

Where:

- $C_a(t,0) = \langle a(t)a(0)\rangle - \langle a(t)\rangle\langle a(0)\rangle$ is the time autocorrelation function of a,
- h is the conjugate of a in the Hamiltonian of the system, that is the Hamiltonian (*i.e.* the free energy) can be written $H = H_{unperturbed} - ah$
- $\frac{\partial \Delta a(t)}{\partial \Delta h(0)}$ is the response of a at time $t > 0$ to the small impulse perturbation Δh applied transiently at time 0. It is called impulse response function, usually denoted $\chi_a(t)$.

This relation can also be expressed in Fourier space (decomposing all temporal signals in terms of periodic functions) as: $s_a(\omega) = -\frac{2\,kT}{\omega} Im\,\hat{\chi}_a(\omega)$, where $s_a(\omega)$ is the power spectrum of a and $\hat{\chi}_a(\omega)$ is the Fourier transform of $\chi_a(t)$, typically referred to as "dynamic susceptibility".

In a system which is not at equilibrium, but nonetheless at steady state, one can define the so-called fluctuation-dissipation ratio [68]:

$$\frac{k\mathrm{T}_{\mathrm{eff}}(\omega)}{\mathrm{kT}} = -\frac{\omega s_a(\omega)}{2kTIm\,\hat{\chi}_a(\omega)}. \qquad (A.2)$$

This FDT ratio is a way to quantify some ''distance to equilibrium'', introducing the effective temperature $\mathrm{T}_{\mathrm{eff}}(\omega)$. The system is in equilibrium only if the ratio equals one at all frequencies.

1.2. Choice of model for the chemotaxis pathway

We model the receptors by two-state objects, being either kinase activating (ON) or kinase inhibiting (OFF). The free energy difference between ON and OFF is $\Delta f_0 = \gamma(m) + \eta(c)$ for a single receptor, with $\eta(c) = \ln\left(\left(1+\frac{c}{K_{OFF}}\right)/\left(1+\frac{c}{K_{ON}}\right)\right)$ being the contribution of attractant binding and $\gamma(m) = k_0 - k_1 m$ being the contribution of the receptor methylation.

Two models can describe the coupling between neighboring receptors and kinases in the chemoreceptor cluster, the Monod-Wyman-Changeux (MWC) and the Ising models [46, 48, 73, 91]. The MWC model considers that receptors are grouped by teams of N_{MWC} infinitely coupled receptors and their associated kinases. The Hamiltonian of the whole chemoreceptor cluster is $H_{MWC} = \sum_{j=1}^{N_{team}}\left(a_j \sum_{k=0}^{N_{MWC}} \Delta f_0(k)\right)$, a_j being the Boolean state of team j. The Ising model on the contrary considers finite coupling between receptors, and the Hamiltonian of the cluster is

$$H_{IM} = H_{int} + \sum_{k=1}^{N_T} a_k\, \Delta f_0(k), \qquad (A.3)$$

where a_k is now the state of the single receptor dimer k and H_{int} describes the coupling between and among receptors and kinases. The interaction term H_{int} can be written in all generality $H_{int} = -J_{aa}\sum_{i,j}(A_i - 0.5)S_{i,j}\left(A_j - 0.5\right) - J_{ar}\sum_{i,k}(A_i - 0.5)V_{i,k}(a_k - 0.5) - J_{rr}\sum_{l,k}(a_l -$

$0.5)W_{l,k}(a_k - 0.5)$, where J are the coupling strengths, S, V and W describe the network by determining whether two components are coupled and A_i is the Boolean activity of the *kinase i*.

At steady state, the average activity of the cluster is given in both cases by

$$A = \langle a \rangle = \frac{1}{Z} \iint \frac{1}{N_T} \sum_{k=1}^{N_T} a_k \exp\left(-\beta H(\{a_k\})\right) \prod da_k, \qquad (A.4)$$

where Z is a normalization factor, and N_T is the total number of Tar dimers. In the MWC, it is solved exactly as $A_{MWC} = (1 + \exp(N_{MWC}\, \Delta f_0))^{-1}$. In the Is, analytical solutions exist only for a limited set of network topologies, but numerical solutions in most cases are well fitted by

$$A_{Is} = \frac{1}{1 + \exp(N\, \Delta f_0)}, \qquad (A.5)$$

where N is a fitted parameter, corresponding to an effective ''team size'', which is proportional to the average number of neighboring receptors with the same activity (see ***1.4***).

The MWC does not allow individual receptors to fluctuate within their team nor any team rearrangement. This is unsatisfactory since individual receptors are expected to undergo independent thermal and/or active perturbations and the slow dynamics in the Δ*cheR*Δ*cheB* strain might come from some remodeling of teams of receptors with the same activity [69]. The Ising model, which possesses those two properties, was therefore preferred.

Finally, the average methylation state of the receptor evolves under the action of CheR and CheB according to

$$\frac{dm}{dt} = k_R\,(1 - A) - k_B\, A, \qquad (A.6)$$

with k_R and k_B being the rates of methylation and de-methylation, respectively [60].

1.3. Phenomenological step response function

To define the effective temperature (Equation (A.2)), the activity state of a *single receptor dimer*, a, will be used as the variable. Considering the definition of the dynamic susceptibility (paragraph 1.1) and Equation (A.3), within the Ising model, the dynamic susceptibility $\chi_a(t)$ in response to a perturbation $+\epsilon$ of the free energy difference Δf_0 is

$$\langle \delta a(t) \rangle = \int_{-\infty}^{t} -\epsilon(\tau)\, \chi_a(t-\tau)\, d\tau, \qquad (A.7)$$

where $\langle \cdot \rangle$ is an ensemble average. In the case of a constant perturbation ϵ_0 starting at $t = 0$,

$$\langle \delta a(t) \rangle = -\epsilon_0 \int_{0}^{t} \chi_a(\tau)\, d\tau. \qquad (A.8)$$

In the absence of adaptation enzymes, Equation (A.5) implies that at steady state $\langle \delta a(+\infty) \rangle = -N \langle a \rangle (1 - \langle a \rangle)\, \epsilon_0$, which yields

$$\int_{0}^{+\infty} \chi_a^-(\tau)\, d\tau = N\langle a \rangle (1 - \langle a \rangle) \equiv \mathrm{X}_A^{\infty}\,. \qquad (A.9)$$

Here and in the following, we use a superscript '-' to refer to quantities in the Δ*cheR*Δ*cheB* case, and superscript '+' for the $\mathrm{CheR}^{+}\mathrm{CheB}^{+}$ case.

In the all models so far, the activity switches very rapidly to its steady state value $\langle \delta a(+\infty) \rangle$, meaning that $\chi_a^-(\tau)$ is well approximated by a delta function. However, as observed in Fig. 4A of the main text, step stimulation with MeAsp, which corresponds to the application of a constant ϵ_0 to the receptors, induces also a long term dynamics of the activity, not captured by the models. A phenomenological description of this long term dynamics was therefore used, leading to a more complex form of $\chi_a^-(\tau)$.

We experimentally defined the step response function $g^{-}(t)$, measured as the response of a $\Delta cheR\Delta cheB$ strain to small step-like attractant stimulation, as

$$g^{-}(t) \equiv \frac{\langle \delta a(t) \rangle}{-\mathrm{X}_A^{\infty}\epsilon_0} = \frac{\langle \delta a(t) \rangle}{\langle \delta a(+\infty) \rangle} = \frac{\Delta R(t)}{-\lambda \mathrm{X}_A^{\infty}\epsilon_0} = \frac{\Delta R(t)}{\Delta R(+\infty)}, \qquad (A.10)$$

which goes from 0 at $t = 0$ to 1 at $t = +\infty$.

Combining Equations (A.8), (A.9) and (A.10), the dynamic susceptibility of a receptor in the $\Delta cheR\Delta cheB$ strain is $\int_0^t \chi_a^{-}(\tau)\, d\tau = \mathrm{X}_A^{\infty}\, g^{-}(t)$, which is expressed in Fourier space as

$$\hat{\chi}_a^{-}(\omega) = \mathrm{X}_A^{\infty}\, i\omega \hat{g}^{-}(\omega) \qquad (A.11)$$

Here the Fourier transform of *x* is defined as

$$\hat{x}(\omega) = \int_{-\infty}^{+\infty} x(t) e^{-i\omega t}\, dt \qquad (A.12)$$

In the CheR$^+$ CheB$^+$ case, by analogy we experimentally define the step response function to small step-like attractant stimulation as:

$$g^{+}(t) \equiv \frac{\langle \delta a^{+}(t) \rangle}{-\mathrm{X}_A^{\infty}\epsilon_0} = \frac{\Delta R^{+}(t)}{-\lambda \mathrm{X}_A^{\infty}\epsilon_0}, \qquad (A.13)$$

Here $\Delta R^{+}(t)$ is the measured YFP/CFP ratio during a small stimulation of free energy ϵ_0 in CheR$^+$ CheB$^+$ cells expressing Tar only and λ is the experimentally determined proportionality factor between FRET ratio and activity. Since the response is adaptive, the stimulation $-\lambda\, \mathrm{X}_A^{\infty}\epsilon_0$ cannot be deduced from the final change in FRET ratio ($\Delta R(+\infty)$). It was rather computed using $\langle A \rangle = 0.5$ and $\epsilon_0 = \ln(1 + \Delta c/K_{off})$, with K_{off} = 7 µM, which is lower than the value typically used for WT cells (K_{off} = 18 µM) [92], to account for the increased sensitivity of the Tar-only strain at our expression level [57].

Similarly to the $\Delta cheRcheB$ case, the following relation holds:

$$\hat{\chi}_a^{+}(\omega) = \mathrm{X}_A^{\infty}\, i\omega \hat{g}^{+}(\omega) \qquad (A.14)$$

1.3.1. Role of CheY/CheZ dynamics

In the previous sections, we have assumed that the concentration of CheY-P follows instantaneously the average activity of the cell. In practice, however, [CheY-P] is delayed compared to the activity. The CheY phosphorylation (by CheA)-dephosphorylation (by CheZ) cycle can be modeled by [93]:

$$\frac{dy}{dt} = \omega_{AY} A(y_{tot} - y) - \omega_{ZY} Z y \qquad (A.15)$$

In Fourier space, assuming that CheZ is abundant, the CheY-P perturbation $\delta y(\omega)$ follows the activity perturbation as [93]:

$$\delta y(\omega) = \delta y_{max} \frac{\omega_Y}{\omega_Y + i\omega} \delta a(\omega) \qquad (A.16)$$

The characteristic frequency is $\omega_Y = 2\text{Hz}$ [93], which lies in the range of frequencies for which our measurements are dominated by instrumental noise. Therefore CheY/CheZ dynamics was neglected.

1.3.2. Effect of diffusive smoothing of the step function

We assumed a step increase of the attractant concentration when measuring the response functions. In practice, because of mixing while delivering the media to the cells, the attractant concentration step is smoothed and it takes about 1 s to reach maximal concentration. We note $\epsilon(t) = \epsilon_0 \epsilon_s(t)$ the actual experimental free energy change experienced by the cells, with $\epsilon_s(t)$ a function which is zero for $t < 0$, and rise to 1 in a time scale of the order of 1 s. Typically, $\epsilon_s(t) = 1 - \exp(-t/\tau_s)$ with $\tau_s = 0.5$ s. In Fourier space, the actually measured activity change is

$$\langle \delta a_{meas}(\omega) \rangle = -\mathrm{X}_A^\infty \epsilon_0 \ \frac{\chi_a(\omega)}{\mathrm{X}_A^\infty} \epsilon_s(\omega) \qquad (A.17)$$

Equations (A.7, A.10, A.13) and (A.17) yield a relation between the actually measured response functions $g^{\pm}_{meas}(\omega)$ and their ideal counterpart $g^{\pm}_{ideal}(\omega)$ – if the perturbation were purely step-like:

$$\frac{\langle \delta a_{meas}(t) \rangle}{-\mathrm{X}^{\infty}_{A}\epsilon_0} \equiv g^{\pm}_{meas}(\omega) = i\omega\epsilon_s(\omega)\ g^{\pm}_{ideal}(\omega) \qquad (A.18)$$

For the typical exponential perturbation, when $\omega \neq 0$,

$$i\omega\epsilon_s(\omega) = 1 - \frac{i\omega\tau_s}{1 + i\omega\tau_s}\,. \qquad (A.19)$$

Equation (A.19) reduces to 1 in the range of frequencies for which our measurement is above noise, and $g^{\pm}_{meas}(\omega) = g^{\pm}_{ideal}(\omega)$ was assumed for most of the analysis. Only for measuring the time scale of adaptation ω_{RB} and the relation between g^{+} and g^{-} (section ***2.1*** of this supplement) was the full Equation (A.18) needed.

1.4. Definition of the effective temperature

Equations (A.2) and (A.11) or (A.14) lead to:

$$\frac{k\mathrm{T}_{\mathrm{eff}}(\omega)}{\mathrm{kT}} = -\frac{s_a(\omega)}{2\,\mathrm{X}^{\infty}_{A} Re\big(\hat{g}(\omega)\big)}, \qquad (A.20)$$

Thus, to compute the effective temperature, we need to evaluate the power spectral density (PSD) of the activity of a single receptor dimer, $s_a(\omega)$. We experimentally have access to the PSD of the YFP/CFP ratio, the fluctuations of which are proportional to the ones of the average activity of the cell A_{cell} with the factor λ, modulo the camera noise, so that

$$s_R(\omega) = \lambda^2\, s_{A_{cell}}(\omega) + \epsilon_n^2. \qquad (A.21)$$

The average activity of the cell is given by $A_{cell} = \frac{1}{N_T}\sum_{k=1}^{N_T} a_k$, so that

$$s_{A_{cell}}(\omega) = \frac{1}{TN_T^2}\sum_{k=1}^{N_T}\sum_{k\prime=1}^{N_T}\langle \delta a_k(\omega)\delta a_{k\prime}^*(\omega)\rangle, \qquad (A.22)$$

Since receptors are coupled, $\langle \delta a_k(\omega)\, \delta a_{k\prime}(\omega)\rangle$ is not necessarily zero. In the Ising model, we have $\langle \delta a_k(\omega)\delta a_{k\prime}^*(\omega)\rangle = \langle |\delta a_k(\omega)|^2\rangle\, C(r_{kk\prime})$, where $C(r_{kk\prime})$ is the correlation function between receptors distant from $r_{kk\prime}$ on the lattice, which decreases exponentially on a given length scale [94], so that $\sum_{k=1}^{N_T}\sum_{k'=1}^{N_T}\langle \delta a_k(\omega)\delta a_{k\prime}^*(\omega)\rangle = N_T N_r\, \langle |\delta a_k(\omega)|^2\rangle$, where N_r is the average number of correlated receptors in the cluster (the loose equivalent of the team size of the MWC model), which is expected to be proportional to the cooperativity number N (Equation A.5).

To accurately count the number of correlated receptors, we noted that recent works measured *in vitro* [63] and *in vivo* [44, 56] the response function of the minimal functional chemosensory assembly, believed to consist of two trimers of receptor dimers (TD) coupled to one CheA dimer, and found a cooperativity number close to 2. The dose-response curve of Δ*cheR*Δ*cheB* CheW-X2 expressing $\mathrm{Tar}^{\mathrm{QEQE}}$, featuring such minimal complexes [44, 56], was fitted using Equation (A.5) (Figure 3 – Figure Supplement 1), also yielding N≃2. These results strongly suggest that N effectively accounts for the number of TDs coupled in a "signaling team", thus $N_r = 3N$ and:

$$s_{A_{cell}}(\omega) = \frac{3N}{N_T} s_a(\omega) \qquad (A.23)$$

Finally, Equations (A.9), (A.20), (A.21) and (A.23) yield:

$$\frac{k\mathrm{T}_{\mathrm{eff}}(\omega)}{\mathrm{kT}} = -\frac{N_T}{6\,\lambda^2 N^2 A(1-A)}\,\frac{s_R(\omega)-\epsilon_n^2}{Re\big(\hat{g}(\omega)\big)}, \qquad (A.24)$$

corresponding to Equation (1) and (2) of the main text, which defines the dissipation $G_R(\omega) = -2\,\lambda^2\,\frac{3N^2A(1-A)}{N_T}\mathrm{Re}\big(\hat{\mathrm{g}}(\omega)\big)$.

Note that although we expressed the fluctuation dissipation relation in terms of activity, which allows us to directly compare the analysis with experimental data, this relation can be formulated for any variable (e.g., receptor conformation) that itself determines the activity.

2. Link between the response functions in Δ*cheR*Δ*cheB* and CheR$^+$ CheB$^+$ cases

In presence of the adaptation system, the receptor cluster is assumed to respond to free energy perturbations in the same way as in the adaptation-deficient cells, but this response induces a methylation change adding up to the free energy perturbation. In Fourier space, for a small perturbation of the free energy difference $\epsilon(\omega)$, the resulting perturbations for the average activity and methylation are then given – from Equations (A.6) and (A.7) – by the set of equations:

$$\langle \delta a^+(\omega) \rangle \;=\; \mathrm{X}_A^\infty \; i\omega \hat{g}^-(\omega) \; (-\epsilon(\omega) + \; k_1 \, \langle \delta m(\omega) \rangle) \qquad (A.25)$$

$$i\omega \, \langle \delta m \rangle \;=\; -\,(k_R + \; k_B) \, \langle \delta a^+(\omega) \rangle \qquad (A.26)$$

Defining $\omega_{RB} = \mathrm{X}_A^\infty k_1 (k_R + \; k_B)$, the activity dependent rate of adaptation, this set of equations is easily solved as

$$\langle \delta a^+(\omega) \rangle \;= \frac{\mathrm{X}_A^\infty \; i\omega \; \hat{g}^-(\omega)}{1 + \omega_{RB} \; \hat{g}^-(\omega)} \big(-\epsilon(\omega)\big) \qquad (A.27)$$

We thus inferred the dynamic susceptibility in CheR$^+$ CheB$^+$ as

$$\hat{\chi}_a^+(\omega) = \frac{\mathrm{X}_A^\infty \; i\omega \; \hat{g}^-(\omega)}{1 + \omega_{RB} \; \hat{g}^-(\omega)} \qquad (A.28)$$

Note that the Δ*cheR*Δ*cheB* case is obtained again if $\omega_{RB} = 0$.

From Equation (A.14), the step response functions in the CheR$^+$ CheB$^+$ and Δ*cheR*Δ*cheB* cases are linked by:

$$\hat{g}^+(\omega) = \frac{\hat{g}^-(\omega)}{1 + \omega_{RB} \; \hat{g}^-(\omega)} \qquad (A.29)$$

2.1. Effect of diffusive smoothing of the step function

In the case where the stimulation is not a perfect step function, modeled by $\epsilon(\omega) = \epsilon_0\epsilon_s(\omega)$, using Equations (A.17) and (A.18), the relation of equivalence can be easily shown to become:

$$\hat{g}^{+}_{meas}(\omega) = \frac{i\omega\epsilon_s(\omega)\ \hat{g}^{-}_{meas}(\omega)}{i\omega\epsilon_s(\omega) + \omega_{RB}\ \hat{g}^{-}_{meas}\ (\omega)}. \qquad (A.30)$$

Using $\epsilon_s(t) = 1 - \exp\left(-\frac{t}{\tau_s}\right)$, with $\tau_s = 0.5$ s, the equivalent of Equation (A.30) in real space was fitted using the experimentally determined $\hat{g}^{-}_{meas}(\omega)$ and $\hat{g}^{+}_{meas}(\omega)$, with ω_{RB} as a free parameter, yielding $\omega_{RB} = 0.06$ Hz (Figure 4 - Figure Supplement 5).

2.2. Frequency of effective temperature divergence

In the CheR$^+$ CheB$^+$ case, the effective temperature diverges when $\mathrm{Re}\hat{g}^{+}(\omega) = 0$. Equation (A.29) thus yield an implicit equation for the frequency at which this divergence occurs, $-\mathrm{Re}g^{-}(\omega_{dvg}) = \omega_{RB}\left|g^{-}(\omega_{dvg})\right|^2$, which has a solution since $\mathrm{Re}g^{-}(\omega)$ is negative. This equation clearly represents a balance between the action of the cluster cooperative response (represented by g^{-}) and adaptation (represented by ω_{RB}). The solution is however not trivial, in particular $\omega_{dvg} \neq \omega_{RB}$, and will depend on both the time scales of cluster dynamics and adaptation. Notably, in [74] the typical time scale of the cluster dynamics was chosen to be much shorter than the one suggested by our measurements, resulting in higher frequency of effective temperature divergence.

3. Separating the contribution of methylation enzymes dynamics to the PSD in CheR$^+$ CheB$^+$ cells

A complementary approach to the modeling of the fluctuating activity of chemoreceptor clusters, which has been used in a number of previous theoretical works [75-77], is to introduce noise terms in equations (A.25) and (A.26), which describe the average behavior of the system, in order to describe the behavior of single receptor *k*:

$$\delta a_k(\omega) = \mathrm{X}_A^{\infty}\ i\omega \hat{g}^{-}(\omega)\ \left(-\epsilon_k(\omega) + k_1 \delta m_k(\omega)\right) \qquad (A.31)$$

$$i\omega\, \delta m_k = -\ (k_R + k_B)\delta a_k(\omega) + \delta r_k(\omega) + \delta b_k(\omega) \qquad (A.32)$$

Here $\epsilon_k(\omega)$ represents thermal noise acting on the receptor, and $\delta r_k(\omega)$ and $\delta b_k(\omega)$ represent noise coming from the intermittent action of CheR and CheB, respectively (see below for possible interpretation of these fluctuations).

This set of equations is easily solved as

$$\delta a_k(\omega) = \mathrm{X}_A^{\infty}\ \hat{g}^{+}(\omega)(-i\omega\epsilon_k(\omega) + k_1(\delta r_k + \delta b_k)), \qquad (A.33)$$

where $\hat{g}^{+}(\omega)$ is defined by Equation (A.29), and can be measured using Equation (A.13). Assuming that the power spectra of δr_k and δb_k are identical, denoted $s_{rb}(\omega)$, the power spectrum of the activity of one receptor is:

$$s_a^{+}(\omega) = |\mathrm{X}_A^{\infty}\ \hat{g}^{+}(\omega)|^2\left(\omega^2 s_{\epsilon}(\omega) + 2k_1^2 s_{rb}(\omega)\right). \qquad (A.34)$$

This equation highlights the contributions of thermal fluctuations and methylation noise to the PSD. If the methylation system is absent, this latter equation reduces to the Δ*cheR*Δ*cheB* case:

$$s_a^-(\omega) = |\mathrm{X}_A^\infty\ \hat{g}^-(\omega)|^2\ \ \omega^2 s_\epsilon(\omega). \qquad (A.35)$$

Under the non-trivial assumption that the thermal noise term (which can be explicitly evaluated using the FDT, Equation (A.20)) remains the same whether adaptation enzymes are present or not, the contribution of the enzymes to the PSD in CheR^+ CheB^+ is:

$$s_a^m(\omega) = s_a^+(\omega) - \left|\frac{g^+(\omega)}{g^-(\omega)}\right|^2 s_a^-(\omega) = |\mathrm{k}_1\mathrm{X}_A^\infty\ \hat{g}^+(\omega)|^2 s_{rb}(\omega), \qquad (A.36)$$

which yields in terms of the FRET ratio, from equations (A.21) and (A.23):

$$s_R^m(\omega) = s_R^+(\omega) - \left|\frac{g^+(\omega)}{g^-(\omega)}\right|^2 s_R^-(\omega) = \frac{3N\lambda^2}{N_T}|\mathrm{k}_1\mathrm{X}_A^\infty\ \hat{g}^+(\omega)|^2 s_{rb}(\omega). \qquad (A.37)$$

Here the thermal noise contribution in presence of adaptation is $s_R^T(\omega) = \left|\frac{g^+(\omega)}{g^-(\omega)}\right|^2 s_R^-(\omega)$.

3.1. Possible interpretation of the methylation-based noise term

The non-perturbative equation for the evolution of the methylation of receptor *k* reads:

$$\frac{dm_k}{dt} = \ -\ w_b b_k a_k + w_r b_r (1 - a_k) \qquad (A.38)$$

Here b_k and r_k evaluate whether, respectively, CheB or CheR is present on the site to act on the receptor, with respective rates w_b and w_r, in an activity-dependent manner. This equation accounts for the fact that CheR and CheB, which are in low amounts compared to the total amount of receptors, bind and unbind in the vicinity of only a given number of receptors. Hence not all receptors are (de)methylated at a given time [33]. The ensemble average of equation (A.38), describing the average methylation dynamics, is:

$$\frac{d\langle m\rangle}{dt} = \; - \; w_b \frac{N_B}{N_T} \langle A\rangle + w_r \frac{N_R}{N_T}(1 - \langle A\rangle) \qquad (A.39)$$

This identifies the ensemble averaged rate of (de)methylation, $k_R = w_r \frac{N_R}{N_T}$ ($k_B = w_b \frac{N_B}{N_T}$). Subtracting equation (A.39) from equation (A.38) leads to the perturbative equation (A.32). This enables to define δb_k and δr_kas:

$$\delta r_k = w_r(1 - \langle A\rangle)\left(r_k - \frac{N_R}{N_T}\right) \qquad (A.40)$$

$$\delta b_k = w_b\langle A\rangle\left(b_k - \frac{N_B}{N_T}\right) \qquad (A.41)$$

These equations enable to identify δr_k (δb_k) as the fluctuations in occupancy of a given receptor by CheR (CheB) and thus $s_{rb}(\omega)$ as the power spectrum of enzyme binding dynamics.

Although noisy, $s_{rb}(\omega)$ appeared to decrease at low frequency (Figure 4 – Figure Supplement 8). Such a decrease indicates anti-correlations [95] in the binding dynamics of the methylation enzymes at their substrates, which is consistent with the common assumption that CheR (CheB) loads and acts only on the inactive (active) receptor. For the example of CheR, this activity dependence implies that once receptor is active, it will not allow CheR to reload and restart acting until it switches back into the inactive state, thus introducing a delay in the rebinding of the enzyme. As a consequence, enzyme binding anti-correlates on the time scale of this delay.

4. Simulation of a simplified model for the array of receptors

In order to reproduce semi-qualitatively the features of the $CheR^{+}$ $CheB^{+}$ behavior displayed in Figure 4, a simple model of the receptor array was simulated. The standard values of all simulation parameters are given in Appendix – Table 1. The simulated array is composed of $N_{\mathrm{team}} = 300$ independent MWC signaling teams. The MWC model was chosen for simplicity, and it is expected to lead to qualitative but not necessarily quantitative match between simulations and experiments. Each signaling team is composed of $N_{rcp} = 3N$ receptor dimers – each of which counts 8 methylation sites. The Boolean activity a_k of the signaling team evolves according to:

$$\frac{da_k}{dt} = -w_a\left(a_k - \frac{1}{1+e^{F}}\right),\ F = N\,\Delta f_0 - k_1\left(m_k - N_{rcp}\,m_0\right) \qquad (A.42)$$

Here, Δf_0 is the attractant dependant stimulation, $w_a$is the flipping rate of the kinase and m_k is the total methylation level of the team.

If m_k is fixed, Equation (A.42) is a simple model for the Δ*cheR*Δ*cheB* case. Since the activity of a single team can only take 0 or 1 as a value, it fluctuates between these two values, being only on average equal to $1/(1+e^{F})$. Since the teams are uncoordinated, the average activity of the whole cluster will fluctuate as well. This dynamics represents the thermal fluctuations in a MWC model. This dynamics was simulated for T = 1000 s after an equilibration period from a random initial condition of same duration, for $n = 100$ repeats, with $F = 0$, *i.e.* $\langle a\rangle = 0.5$. Increasing latencies in the response to stimulations of the receptor cluster were modeled by decreasing w_a, for a fixed amplification factor $N = 14$. As expected, the thermal fluctuations were slower for lower w_a. The maximal amplitude of the fluctuations was also larger when w_a was larger (Figure

4 – Figure Supplement 4). Increasing N while keeping the total number of receptors constant (*i.e.* decreasing N_{team} accordingly), at fixed w_a, led to an increased amplitude of the fluctuations, their temporal dependences being however not affected (Figure 4 – Figure Supplement 4). The power spectra however differed from experimental data. The amplitude was underestimated because the MWC does not allow applying thermal fluctuations to individual receptor. The time dependence was also different because we modeled the slow receptor cluster dynamics by lengthening the switching rate w_a, which is the only time scale of the model, where in reality they probably are different processes.

In the CheR$^+$ CheB$^+$ case, the methylation level evolves according to:

$$\frac{dm_k}{dt} = w_m \left(r_k \,\&\big(m_k < 8N_{rcp}\big) - b_k \,\&(m_k > 0) \right) \qquad (A.43)$$

Here r_k (b_k) represents whether a CheR (CheB) protein is tethered to the team. Importantly, the model assumes that only one enzyme may be tethered to the team at a time. (De)methylation occurs at the rate w_m if CheR (CheB) is present and m_k has not reached its maximal (minimal) value. The enzyme tethering dynamics is given by the set of equation:

$$\frac{dr_k}{dt} = w_l(1 - r_k)(1 - b_k)(1 - a_k) - w_u r_k a_k \qquad (A.44)$$

$$\frac{db_k}{dt} = w_l(1 - r_k)(1 - b_k)a_k - w_u b_k(1 - a_k) \qquad (A.45)$$

under the constraint $\sum_k b_k \leq b_{tot}$ and $\sum_k r_k \leq r_{tot}$. This means that CheR (CheB) may only load, if free enzymes are available, on free inactive (active) receptors with rate w_l and unload once the receptor turned active (inactive) with rate w_u.

The typical dynamics in the simulation will then be the following. Take, for example, a weakly methylated team. Its activity will get to zero (Equation (A.42)). If free CheR is available, it will load on the team (Equation (A.44)) and methylate it (Equation (A.43)), until the methylation level is high enough to activate the team (Equation (A.42)). CheR will then unload (Equation (A.44)), and a hypothetic free CheB can then load on the team (Equation (A.45)) to demethylate it and bring it to its initial state.

The level of phosphorylated CheY of the simulated cell, also used as an output of the model, evolves according to:

$$\frac{dy}{dt} = w_y \left(\frac{1}{N_{team}} \sum_{k=1}^{N_{team}} a_k - y \right) \qquad (A.46)$$

Output quantities were averaged over n = 100 independent simulations of single cells.

In practice, w_u, w_l and $w_a$were chosen of the same order of magnitude, and they were the slowest dynamics, whereas w_m was the fastest, in order to obtain reasonable dynamics.

Starting from a random initial condition, the system was let to equilibrate at $\Delta f_0 = 0$ for 100 times the slowest time scale of the system ($1/w_l$). The system was then challenged with free energy perturbation $\Delta f_0 = \ln(1 + 0.3/7)$ (mimicking the experimental conditions) to measure the step response function, computed as $g_{simu}(t) = \frac{\Delta y(t)}{N_{\text{eff}} \Delta f_0}$. Figure 4 – Figure Supplement 9A shows the normalized step response function compared to its experimental counterpart with excellent agreement (although absolute amplitudes differed moderately).

A T = 800 s equilibrated run was further used to compute power spectra, using Equation (5) of the main text. The power spectra of r_k and b_k, corresponding to the inferred $s_{rb}(\omega)$ defined in

Equation (A.36), show good qualitative agreement with the experimental data, with a transition from high values at frequencies larger than 0.01 Hz to low values below this threshold (Figure 4 – Figure Supplement 9B). This transition indicates anti-correlations in the occupancy of the receptor teams by the enzymes, which emerge from their *activity-dependant* loading and unloading. The two spectra are equal within noise by construction of the model (r and b play symmetric roles). Furthermore, the simulated power spectrum of the activity $s_A(\omega)$ was similar to the experimental power spectrum corrected for long term cluster dynamics (compare Figure 4D with Figure 4 – Figure Supplement 9C). The amplitude of the power spectrum was however ~100 fold lower than in experiments, but in line with previous simulations [74].

Finally, from the power spectrum of the CheY-P level $s_Y(\omega)$, which was very close to $s_A(\omega)$, an effective temperature can be computed as

$$\frac{\mathrm{T}}{\mathrm{T_{eff}}} = \frac{2\langle \mathrm{A} \rangle (1 - \langle \mathrm{A} \rangle)}{N_{team}} \frac{\hat{g}_{simu}(\omega)}{s_Y(\omega)} \qquad (A.47)$$

It compares qualitatively well with the experimental effective temperature, with concordant frequencies of divergence (Figure 4 – Figure Supplement 9D). Differences appear for the lowest frequencies, probably because of the long-term dynamics of the receptor clusters, which was not accounted for by these simulations.

All things being otherwise equal, modifying N to 2 and N_{team} to 2100, which models the disruption of the chemoreceptor clusters into individual trimers of dimers, reduced strongly the fluctuations in activity (Figure 4 – Figure Supplement 9C). Decreasing the specific rate of receptor (de)methylation when the enzyme is bound to the receptors, w_m, to $w_m = 0.016$ s^{-1} had however little effect (Figure 4 – Figure Supplement 9C). Note that in both cases the adaptation

time is reduced by a similar factor (7 and 6, respectively), since this time is proportional to the product $N\omega_m$, as evident from equations (A.41) and (A.42).

Conditional tethering of the adaptation enzymes to the receptors therefore seems to account relatively well for the observed dynamics. One important discrepancy between simulations and experiments is in the amplitudes of the fluctuations, which are much larger than expected in experiments, when the simple MWC model is considered.

Appendix-Table 1

Parameter	Value	Reference
N	14	This study (based on experimental values)
N_{team}	300	This study (based on experimental values)
k_1	0.016	Adapted from [96]
w_m	1 s^{-1}	This study
w_l	0.15 s^{-1}	This study
w_u	0.5 s^{-1}	This study
w_y	1 s^{-1}	[93]
w_a	0.25 s^{-1}	This study
b_{tot}	240	[29]
r_{tot}	140	[29]

A

+ Attractant

ON

OFF

IM

SAH

R

SAM

+m

-m

W W

W W

A^a

A^i

B

B

ATP

ADP

P

Adaptation

Y

Y

Z Y

P

P

motor Y

P

motor

CW

CCW

TUMBLE

RUN

FRET

NO FRET

Y Z

P

Y Z

B

flow cell

pump

40 x

Light source

emCCD camera

optosplit

C

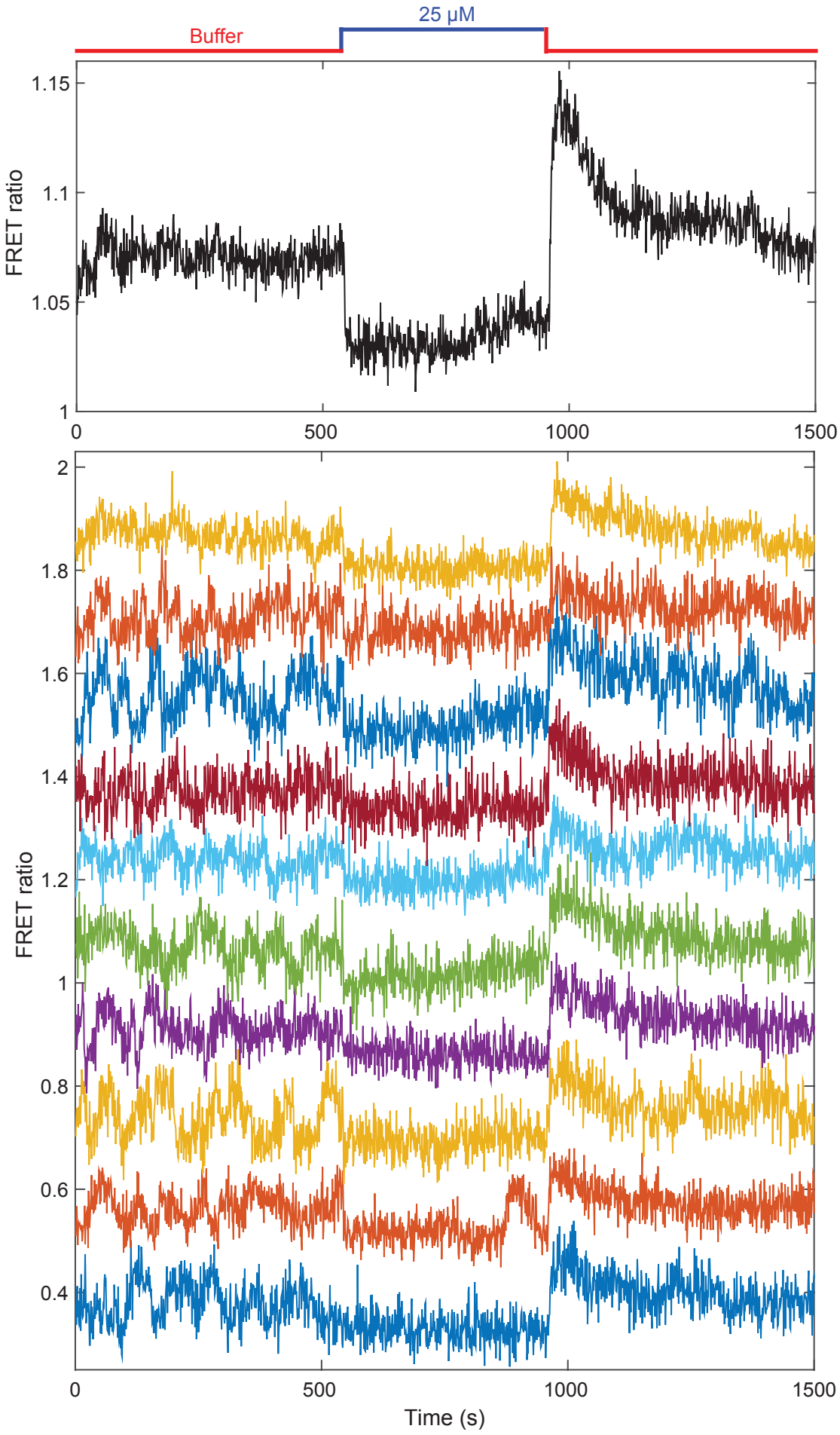
Buffer
25 μM
FRET ratio
1.15
1.1
1.05
1
0
500
1000
1500
FRET ratio
2
1.8
1.6
1.4
1.2
1
0.8
0.6
0.4
0
500
1000
1500
Time (s)

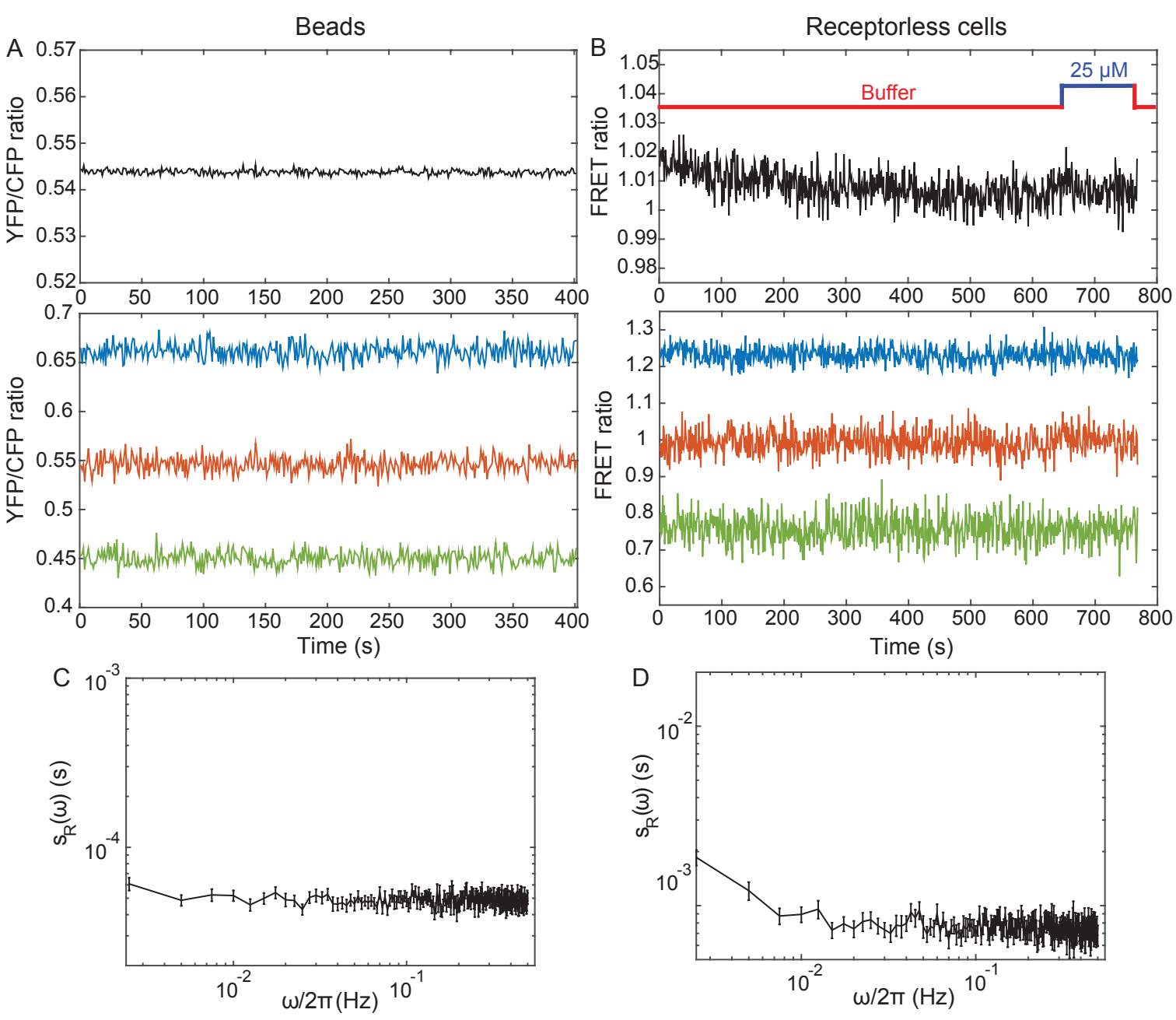
Beads
Receptorless cells
A
B
C
D
YFP/CFP ratio
FRET ratio
Buffer
25 μM
Time (s)
$s_R(\omega)$ (s)
ω/2π (Hz)

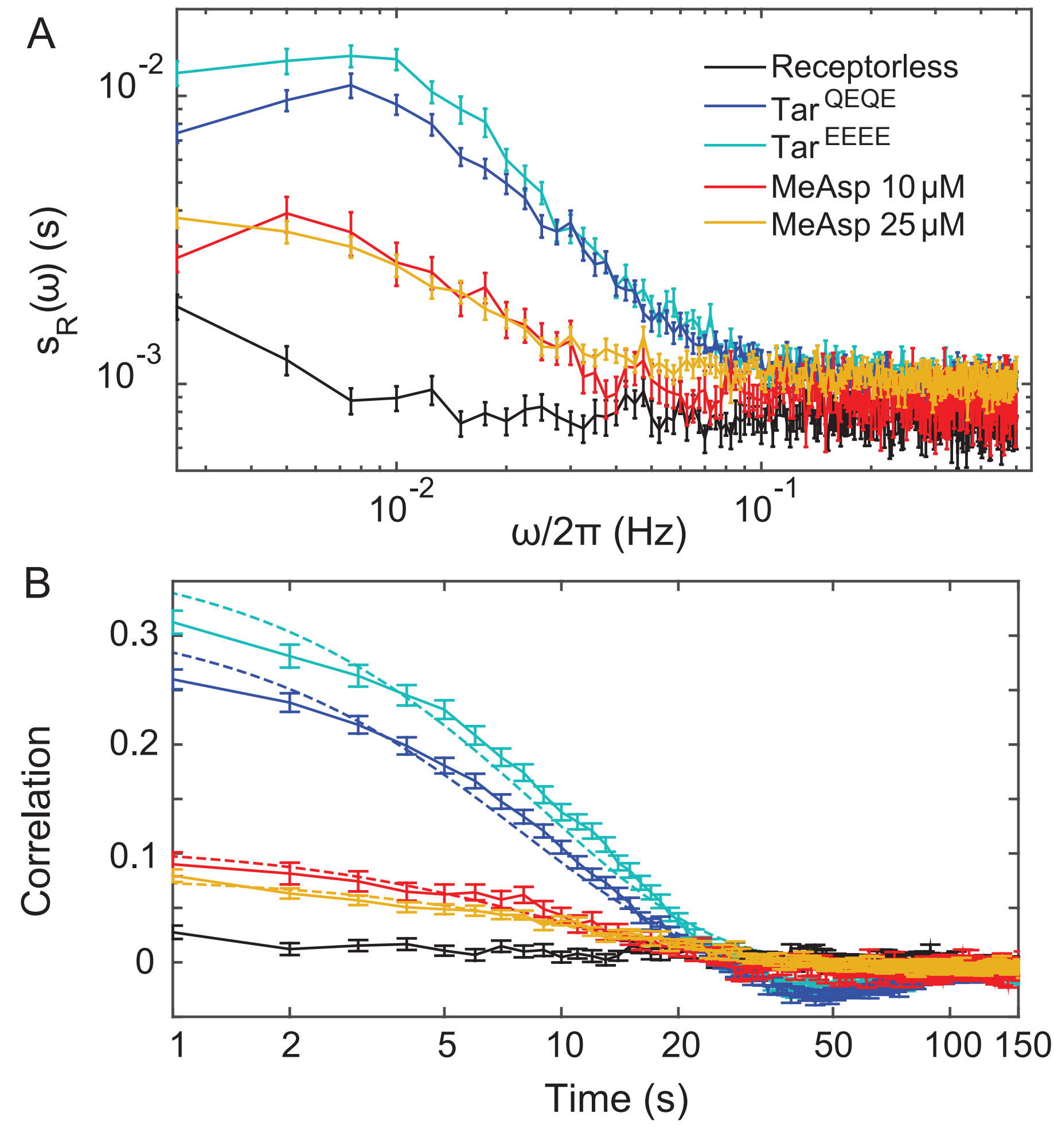
A
10^{-2}
10^{-3}
$s_R(\omega)$ (s)
Receptorless
Tar ^{QEQE}
Tar ^{EEEE}
MeAsp 10 μM
MeAsp 25 μM
10^{-2}
10^{-1}
ω/2π (Hz)
B
0.3
0.2
0.1
0
Correlation
1
2
5
10
20
50
100
150
Time (s)

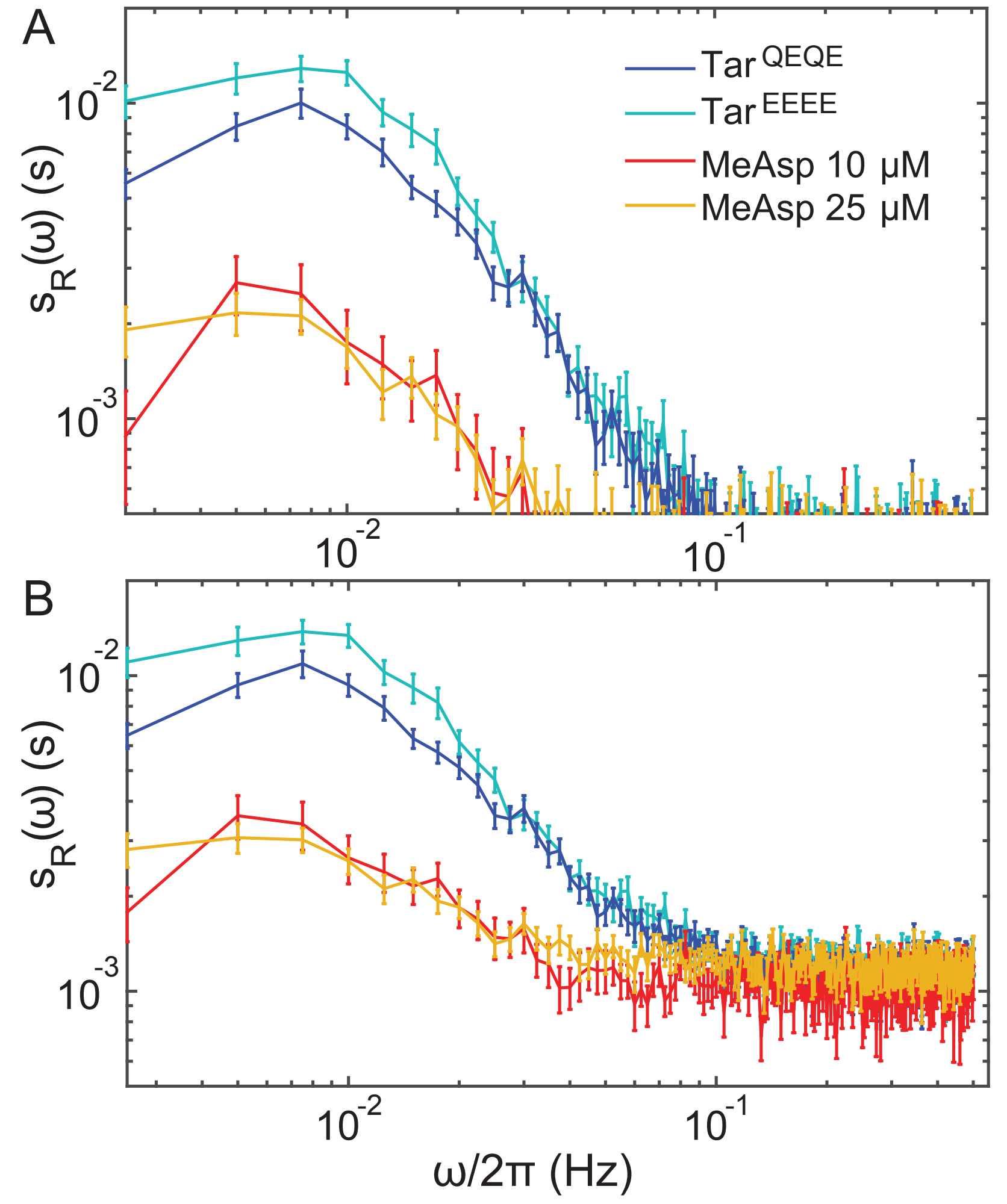
A
B
Tar QEQE
Tar EEEE
MeAsp 10 μM
MeAsp 25 μM
$s_R(\omega)$ (s)
10^{-2}
10^{-3}
10^{-2}
10^{-1}
ω/2π (Hz)

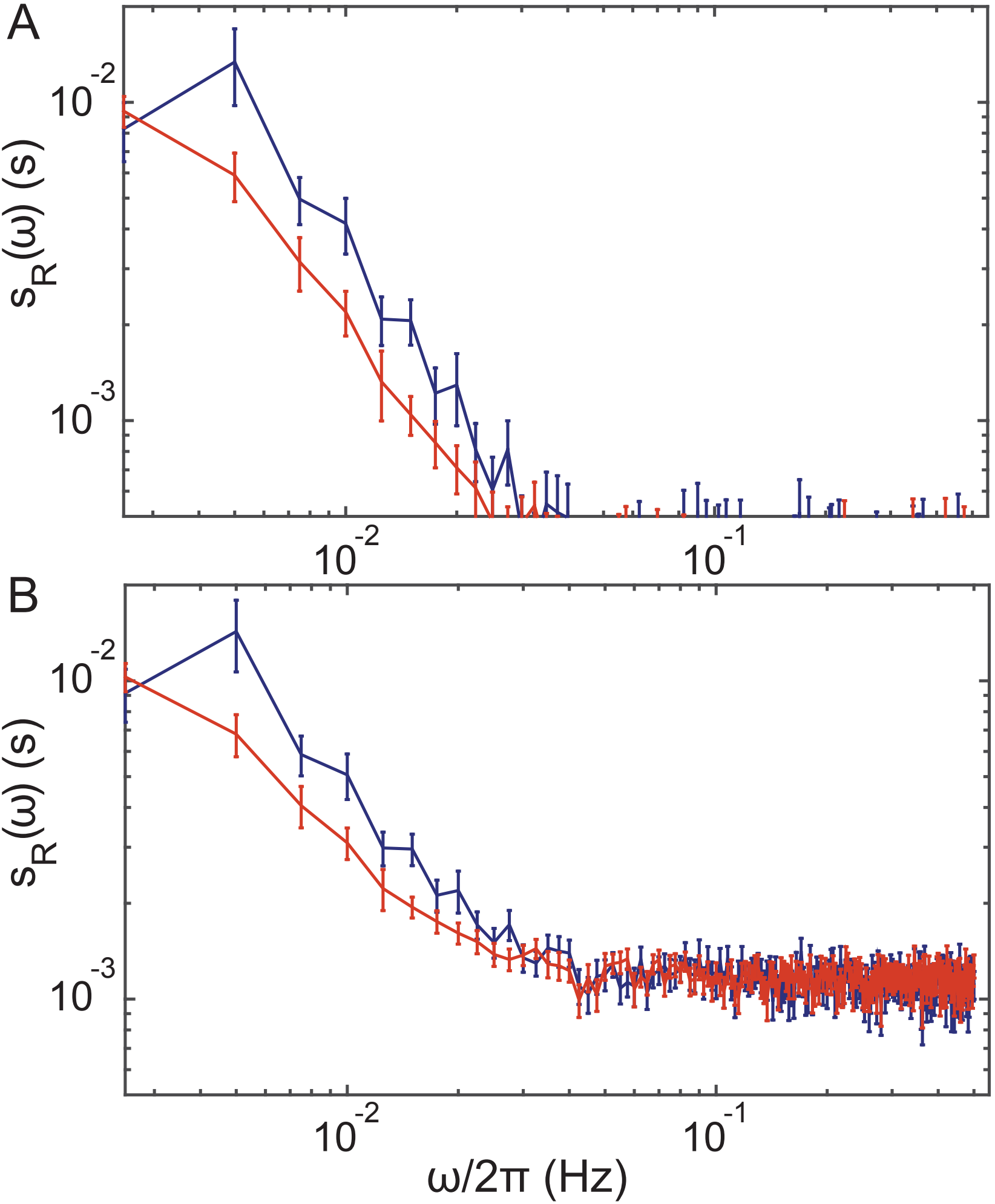
A
B
10^{-2}
10^{-3}
$s_R(\omega)$ (s)
10^{-2}
10^{-1}
$\omega/2\pi$ (Hz)

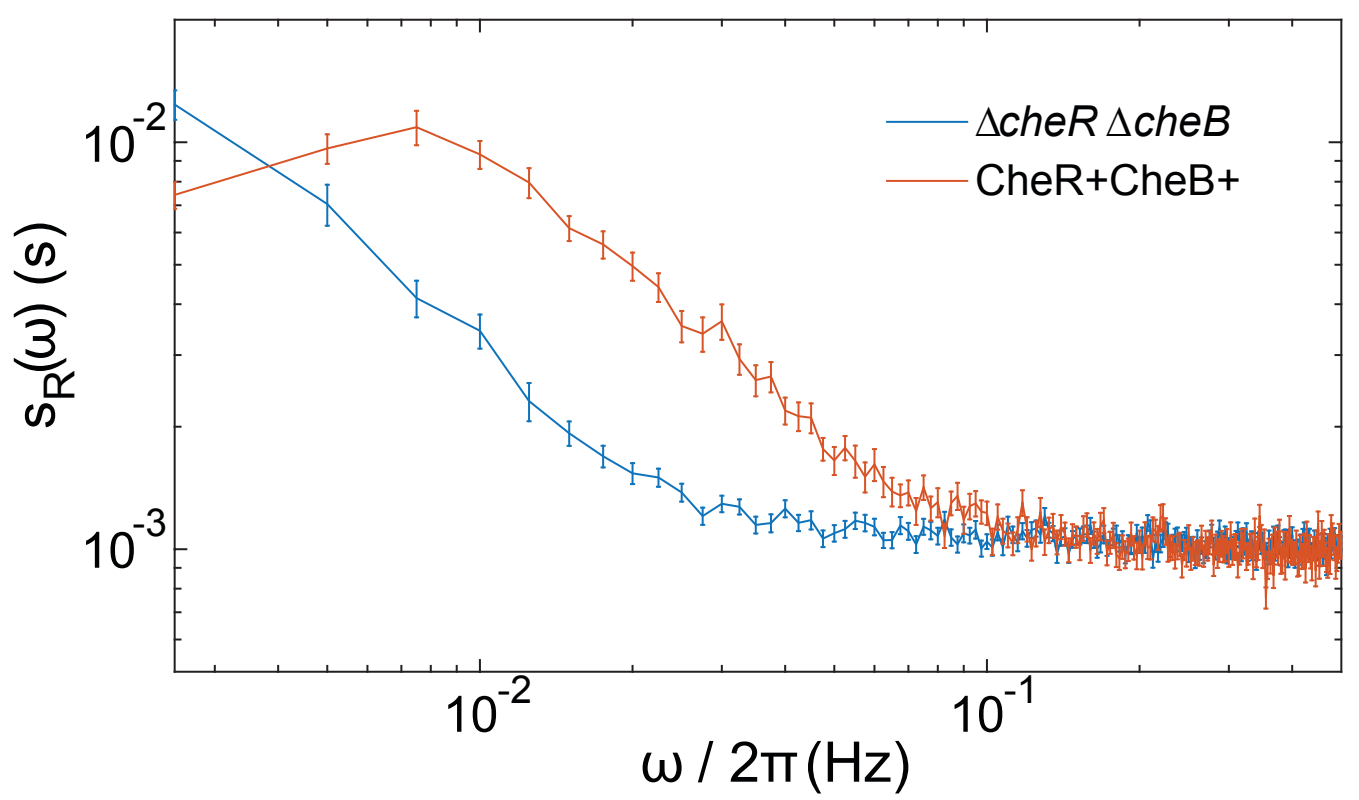
Δ*cheR* Δ*cheB*
CheR+CheB+
10^{-2}
10^{-3}
$s_R(\omega)$ (s)
10^{-2}
10^{-1}
ω / 2π (Hz)

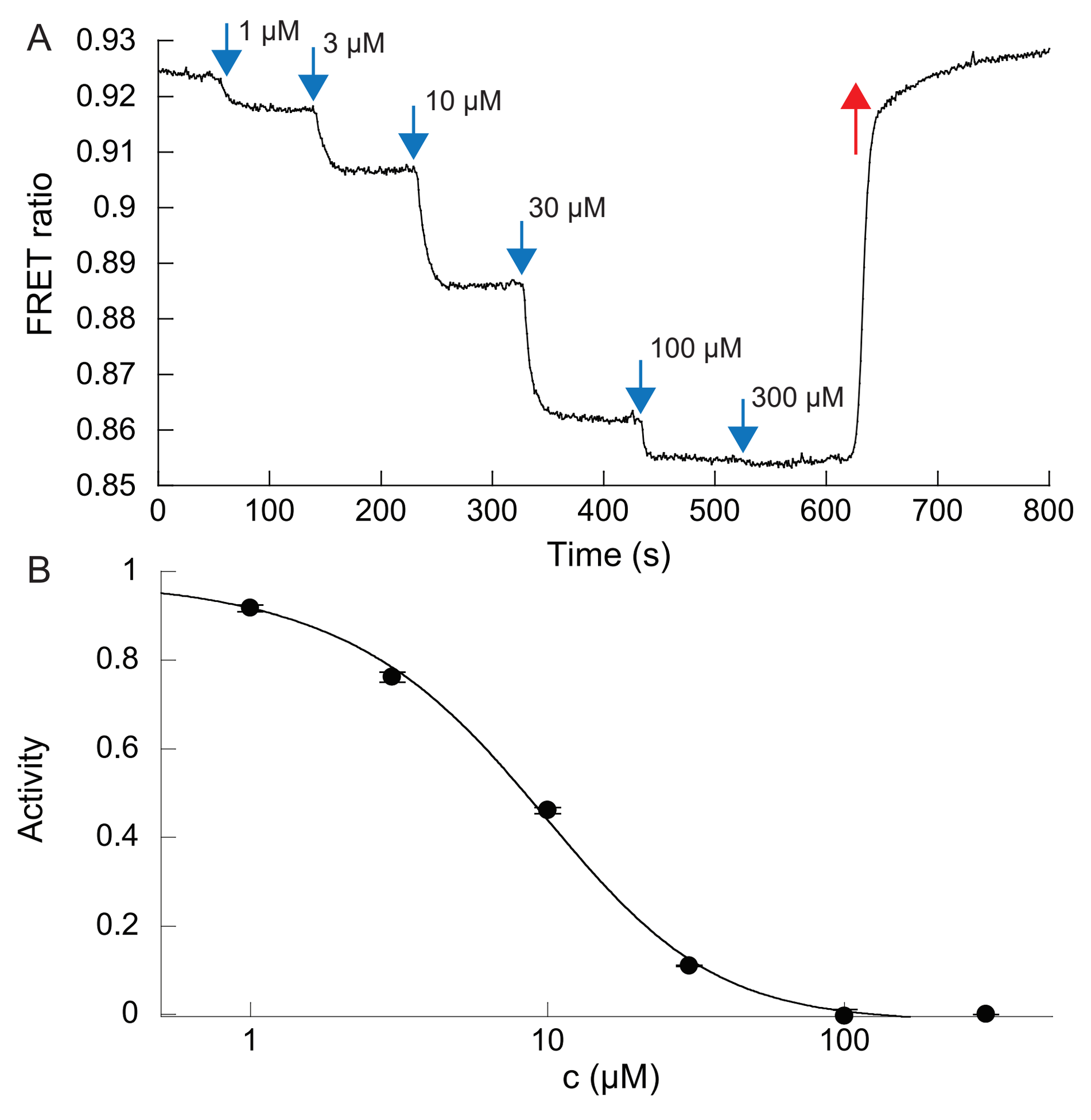
A
1 µM
3 µM
10 µM
30 µM
100 µM
300 µM
FRET ratio
0.93
0.92
0.91
0.9
0.89
0.88
0.87
0.86
0.85
0
100
200
300
400
500
600
700
800
Time (s)
B
Activity
1
0.8
0.6
0.4
0.2
0
1
10
100
c (µM)

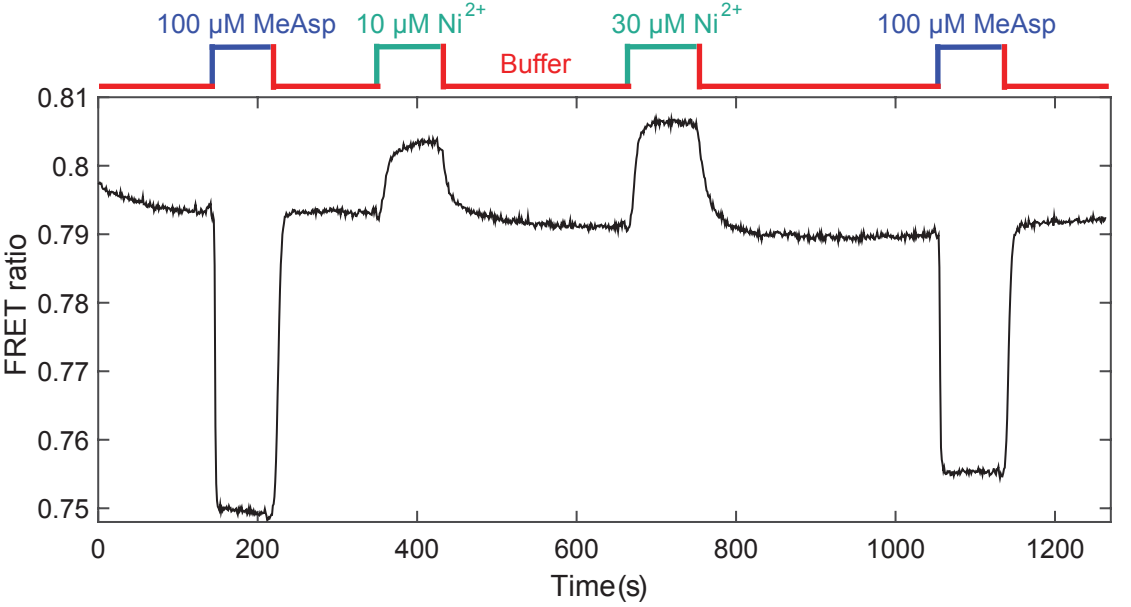
100 μM MeAsp
10 μM Ni2+
30 μM Ni2+
100 μM MeAsp
Buffer
0.81
0.8
0.79
0.78
0.77
0.76
0.75
FRET ratio
0
200
400
600
800
1000
1200
Time(s)

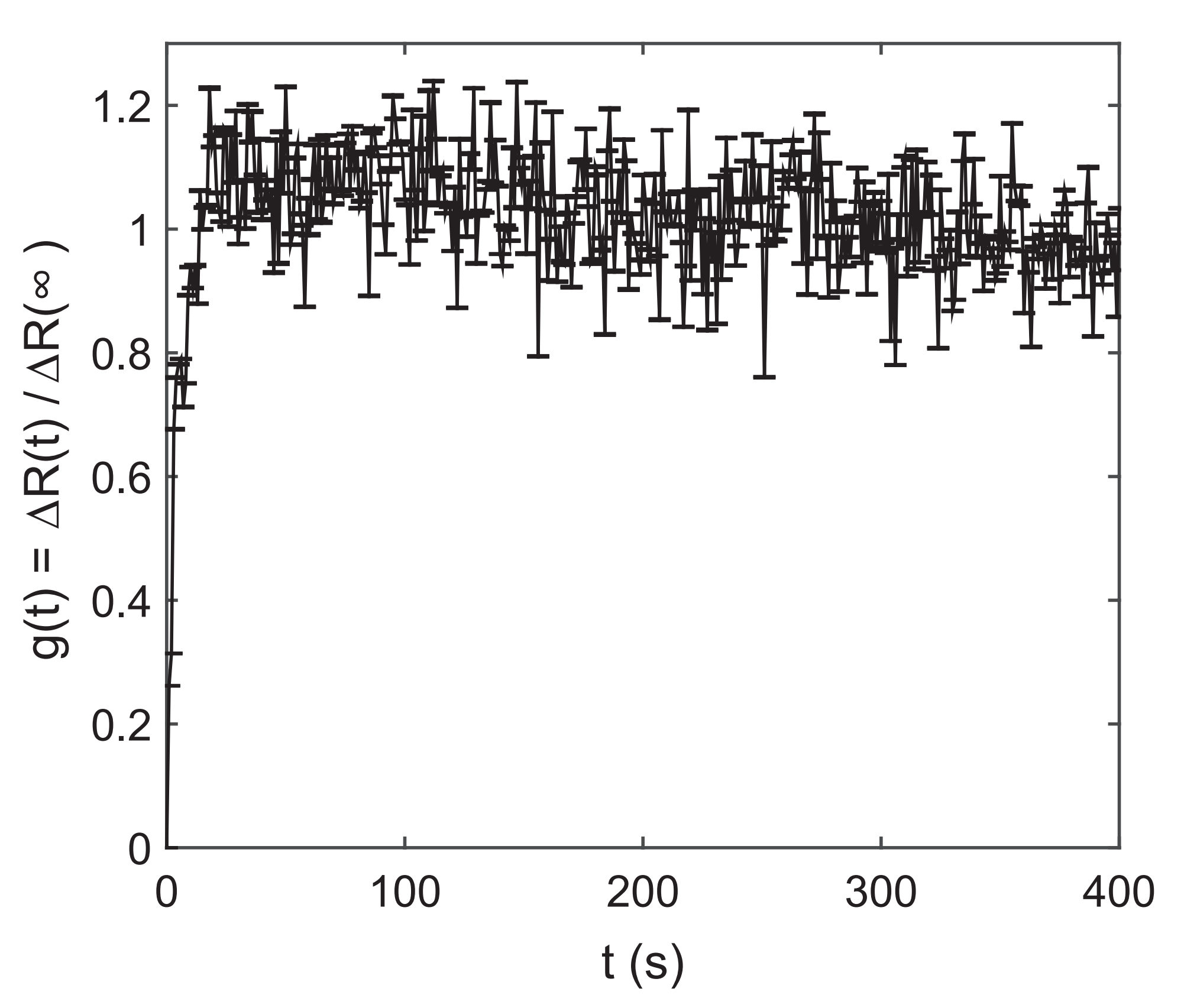
1.2
1
0.8
0.6
0.4
0.2
0
g(t) = ΔR(t) / ΔR(∞)
0
100
200
300
400
t (s)

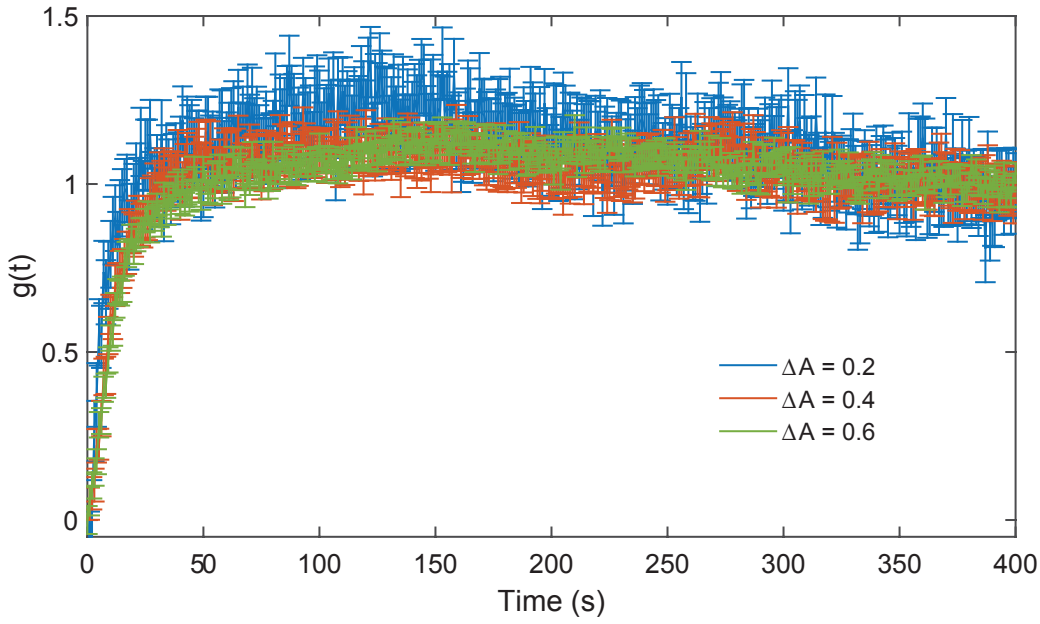
1.5
1
0.5
0
g(t)
0
50
100
150
200
250
300
350
400
Time (s)
ΔA = 0.2
ΔA = 0.4
ΔA = 0.6

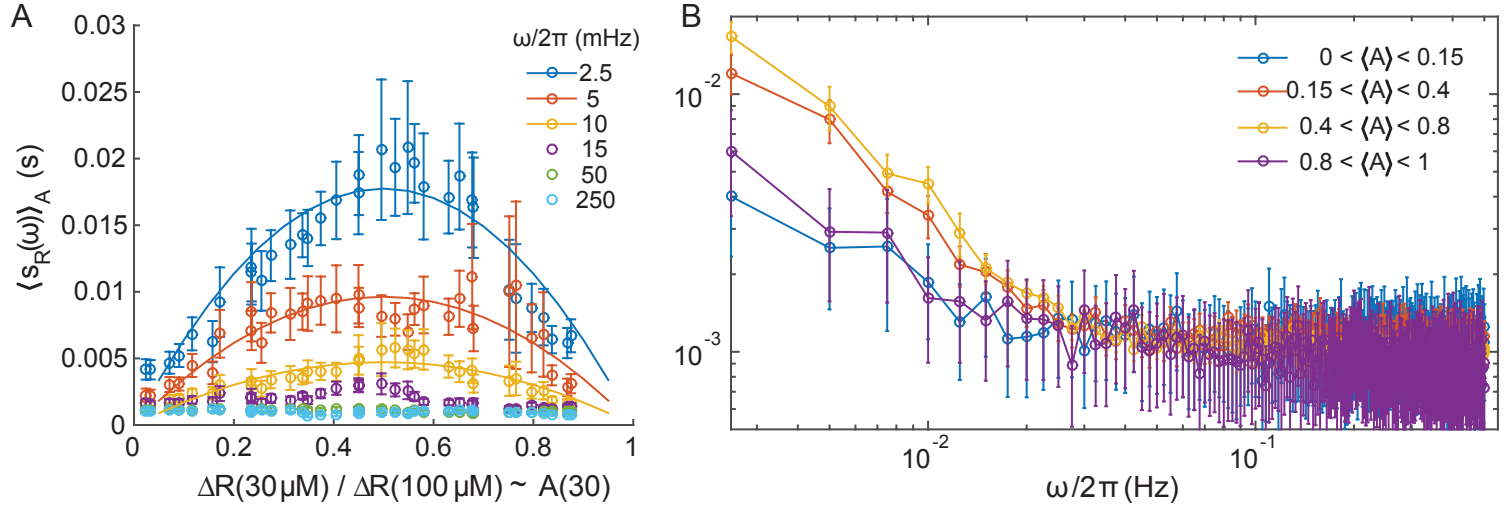
A
0.03
0.025
0.02
0.015
0.01
0.005
0
$\langle s_R(\omega) \rangle_A$ (s)
ω/2π (mHz)
2.5
5
10
15
50
250
0
0.2
0.4
0.6
0.8
1
ΔR(30 μM) / ΔR(100 μM) ~ A(30)
B
10^{-2}
10^{-3}
0 < ⟨A⟩ < 0.15
0.15 < ⟨A⟩ < 0.4
0.4 < ⟨A⟩ < 0.8
0.8 < ⟨A⟩ < 1
10^{-2}
10^{-1}
ω/2π (Hz)

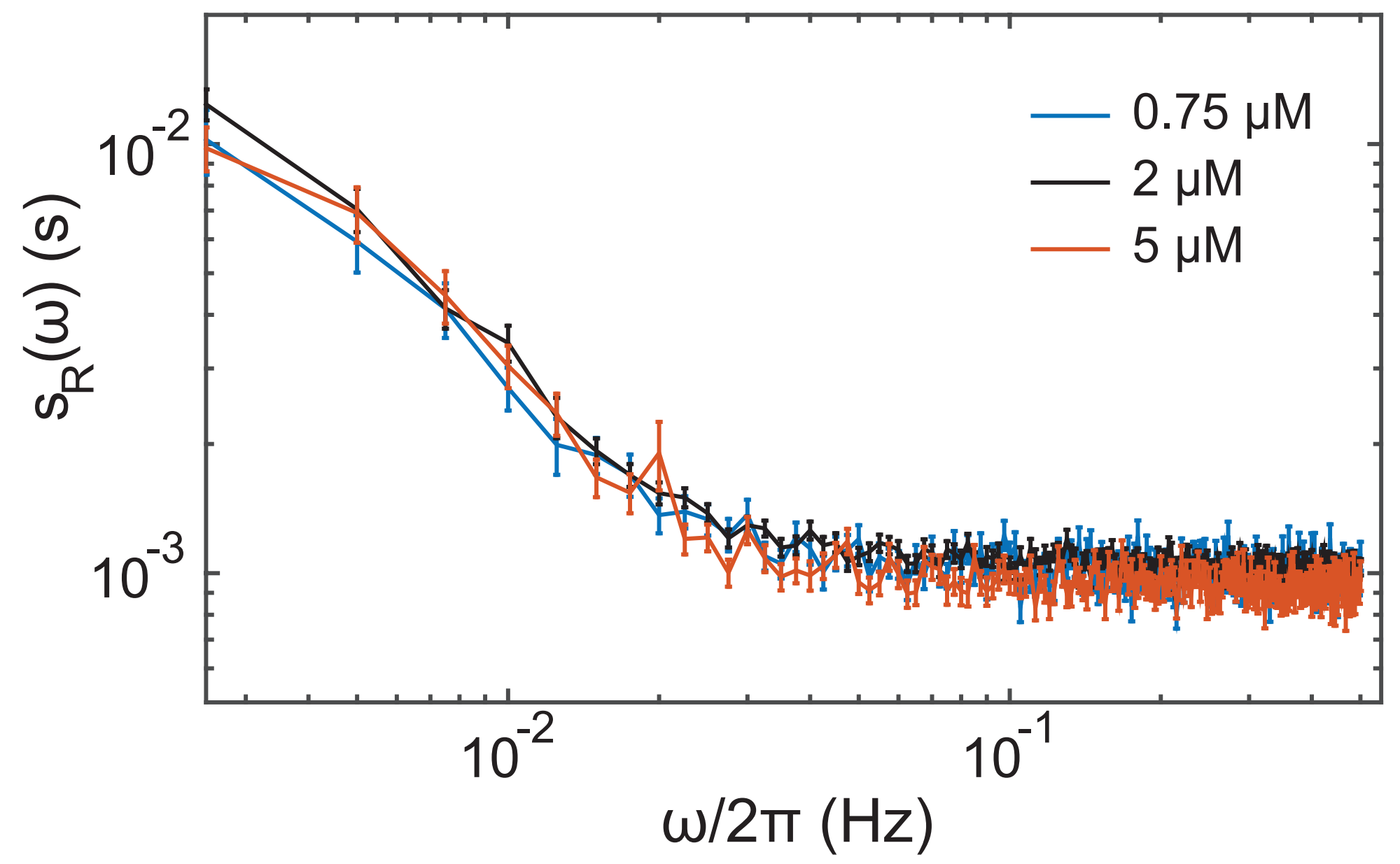
0.75 μM
2 μM
5 μM
10^{-2}
10^{-3}
$s_R(\omega)$ (s)
10^{-2}
10^{-1}
ω/2π (Hz)

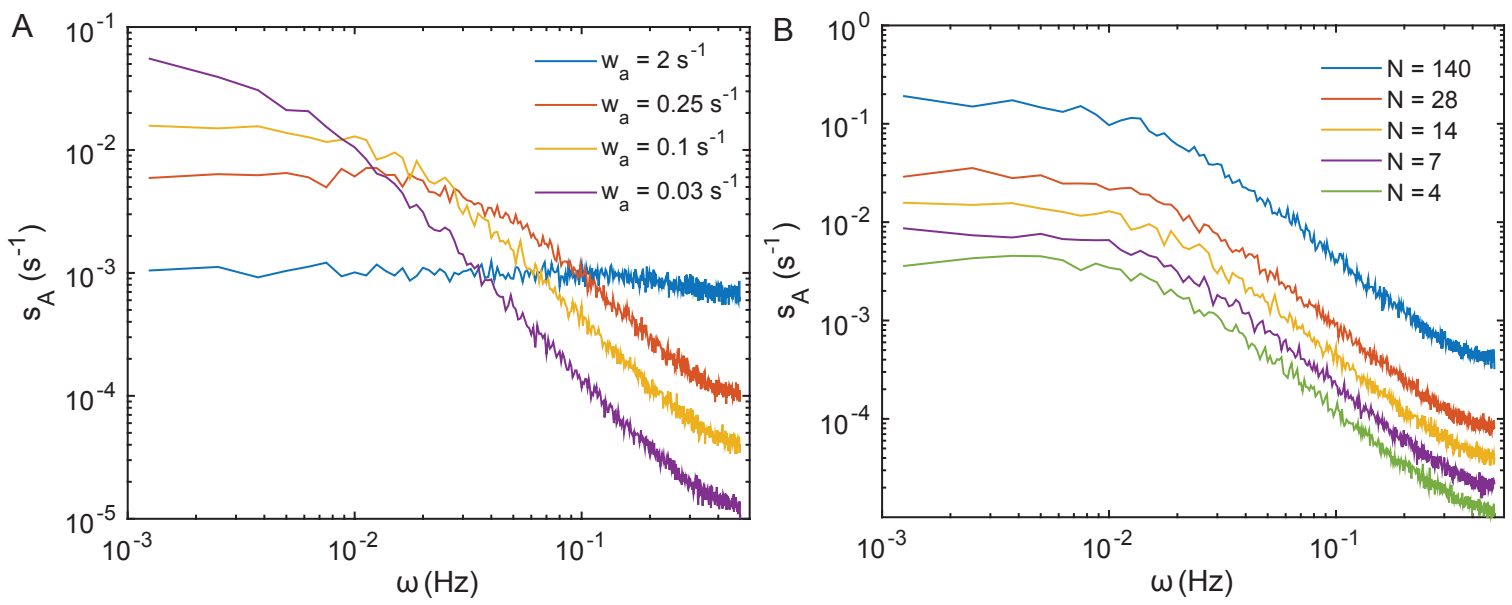
A
B
s_A (s^{-1})
ω (Hz)
w_a = 2 s^{-1}
w_a = 0.25 s^{-1}
w_a = 0.1 s^{-1}
w_a = 0.03 s^{-1}
N = 140
N = 28
N = 14
N = 7
N = 4

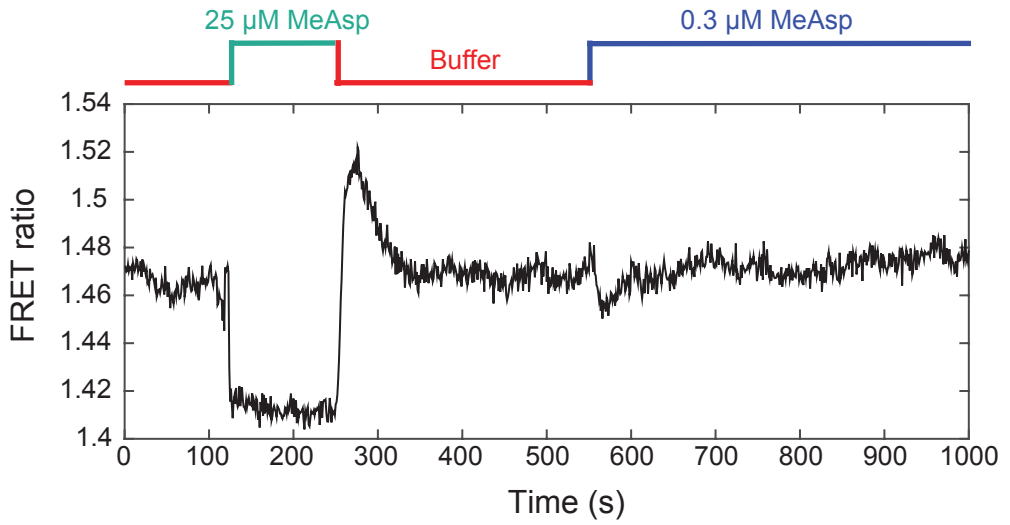
25 μM MeAsp
Buffer
0.3 μM MeAsp
FRET ratio
1.54
1.52
1.5
1.48
1.46
1.44
1.42
1.4
0
100
200
300
400
500
600
700
800
900
1000
Time (s)

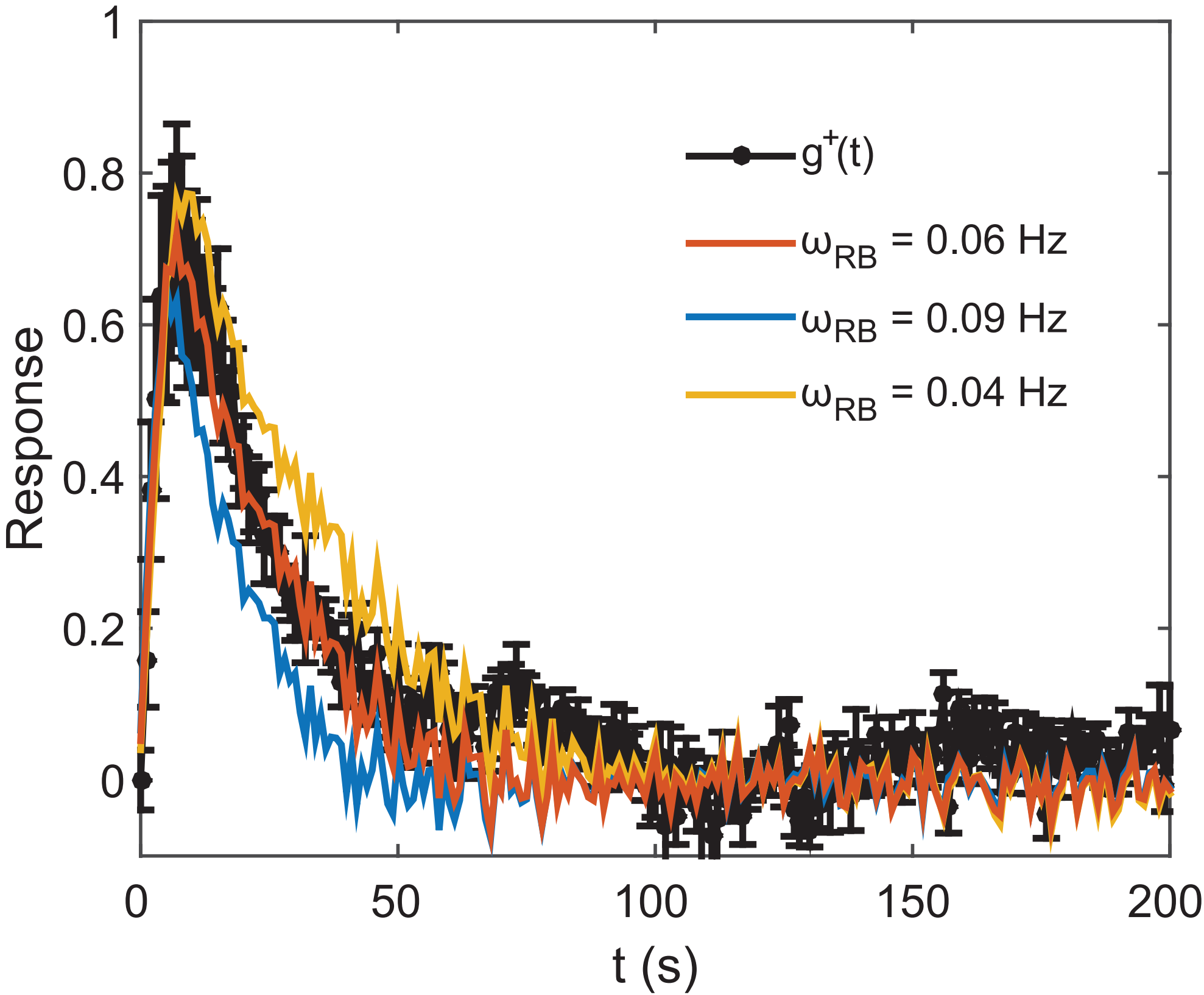
1
0.8
0.6
0.4
0.2
0
Response
0
50
100
150
200
t (s)
g+(t)
ωRB = 0.06 Hz
ωRB = 0.09 Hz
ωRB = 0.04 Hz

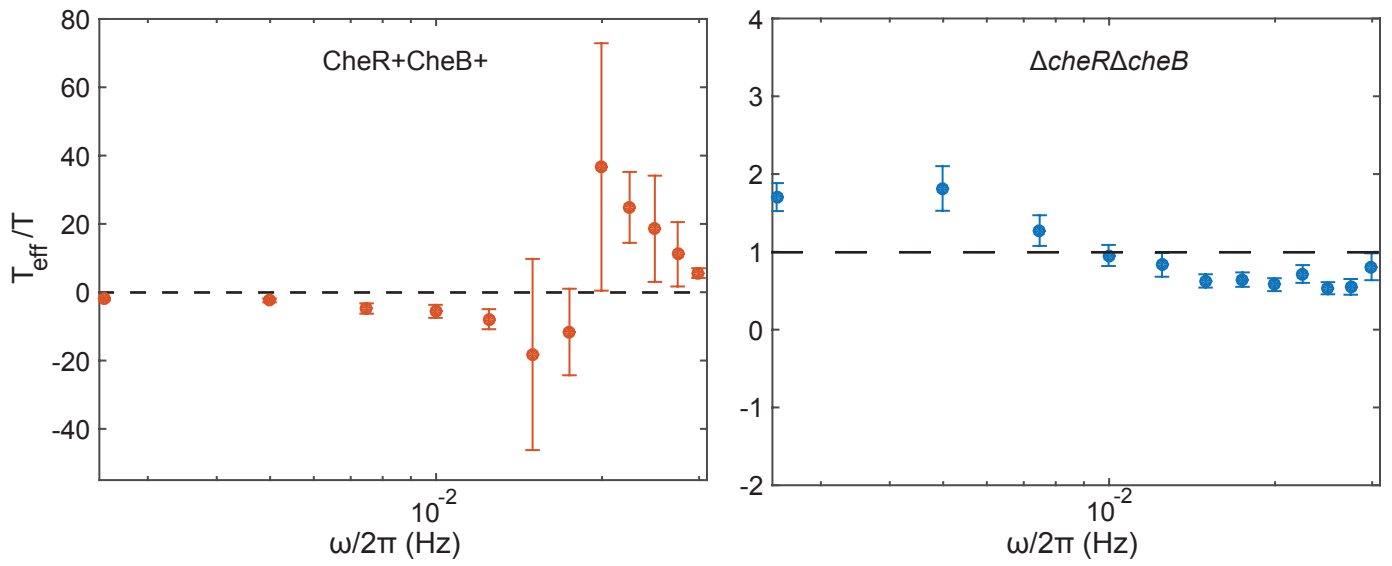
CheR+CheB+
ΔcheRΔcheB
T_eff/T
80
60
40
20
0
-20
-40
4
3
2
1
0
-1
-2
10^-2
ω/2π (Hz)
10^-2
ω/2π (Hz)

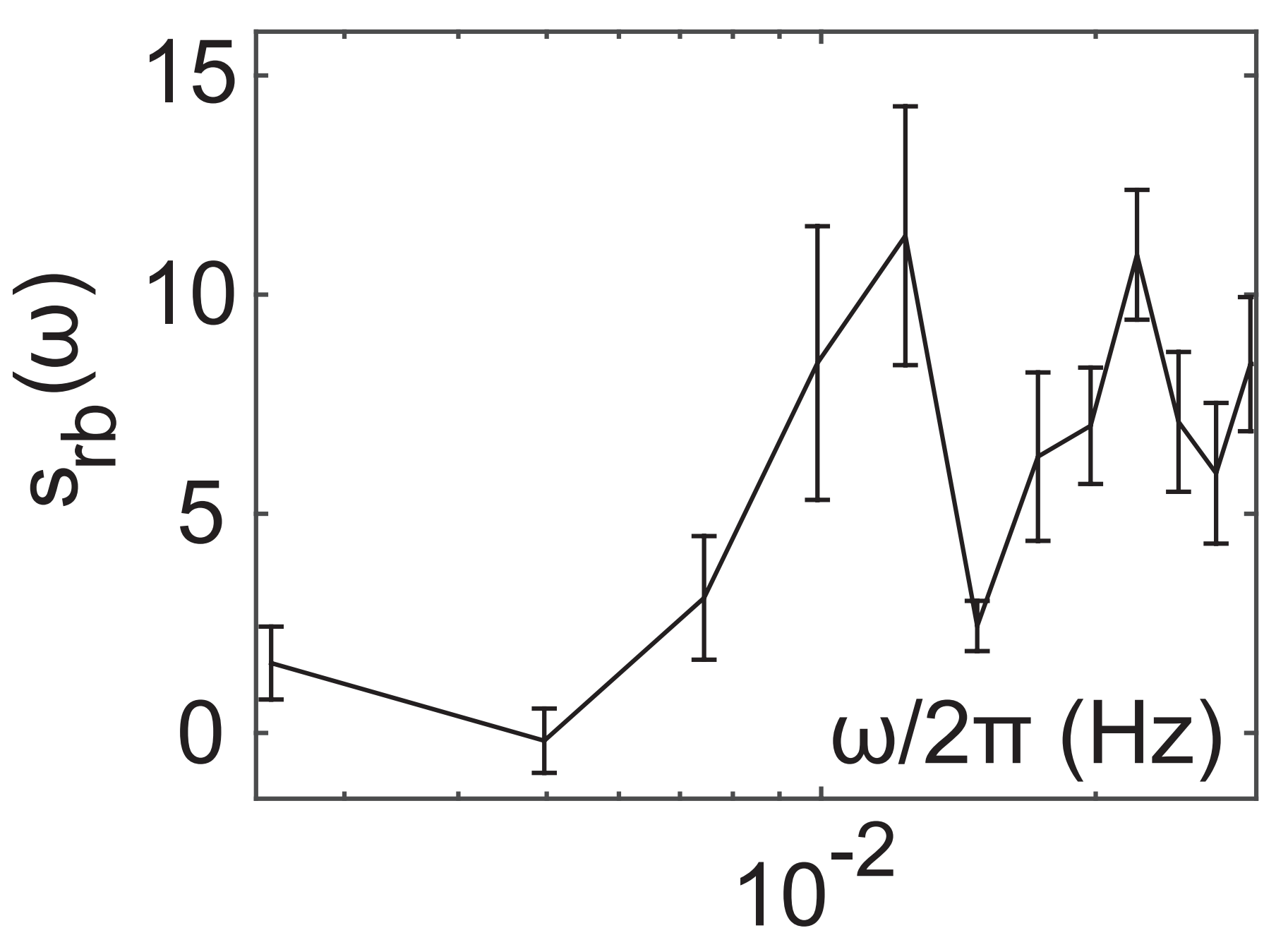
15
10
5
0
$s_{rb}(\omega)$
ω/2π (Hz)
10^{-2}

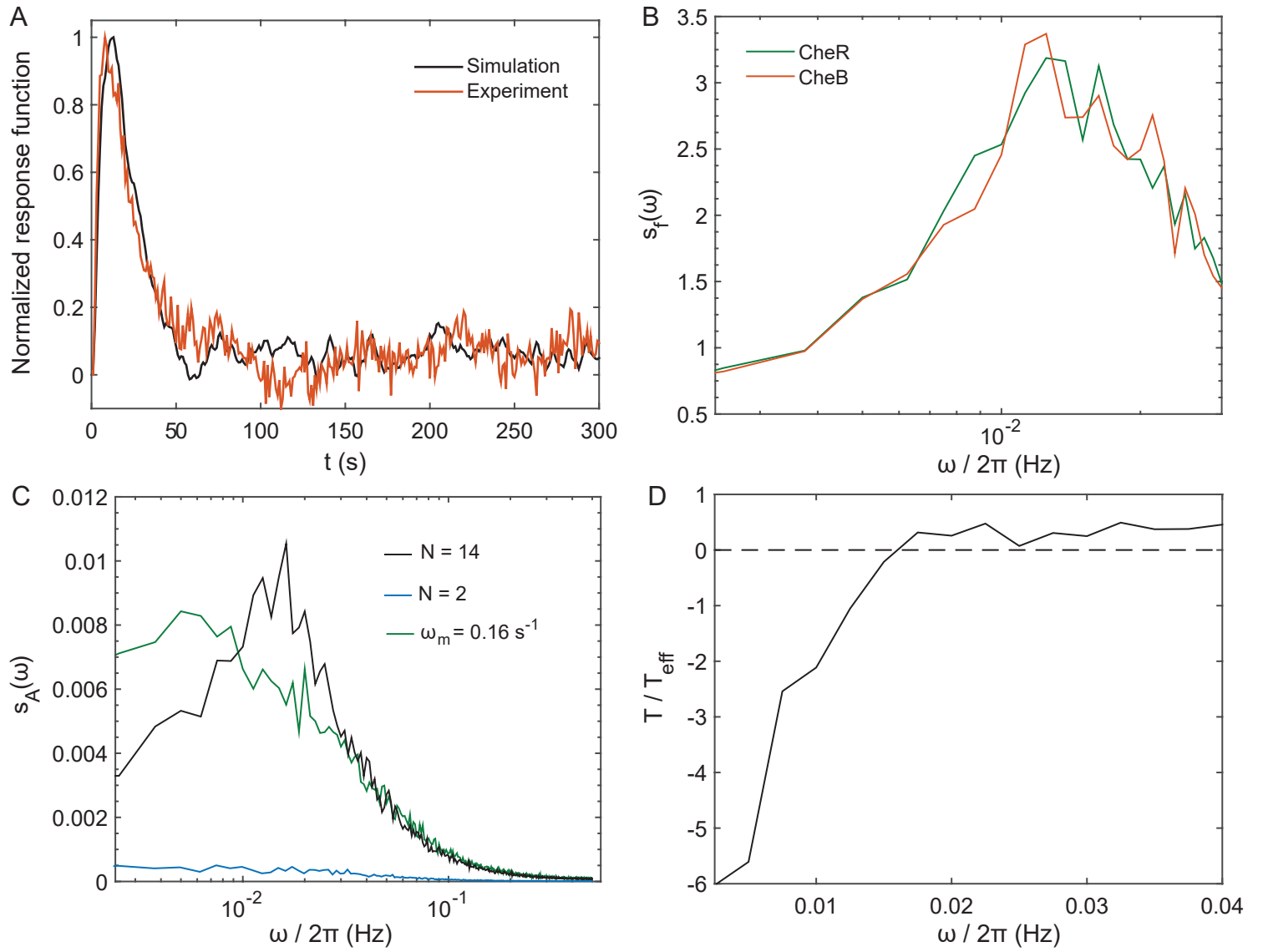
A
Normalized response function
Simulation
Experiment
t (s)
B
CheR
CheB
$s_f(\omega)$
10^{-2}
ω / 2π (Hz)
C
N = 14
N = 2
ω_m = 0.16 s^{-1}
$s_A(\omega)$
10^{-2}
10^{-1}
ω / 2π (Hz)
D
T / T_{eff}
ω / 2π (Hz)